Three Flavour Effects

in

Future Neutrino Oscillation Experiments

by
Dipl.-Phys. Univ. Patrick Huber

Thesis
September 2003

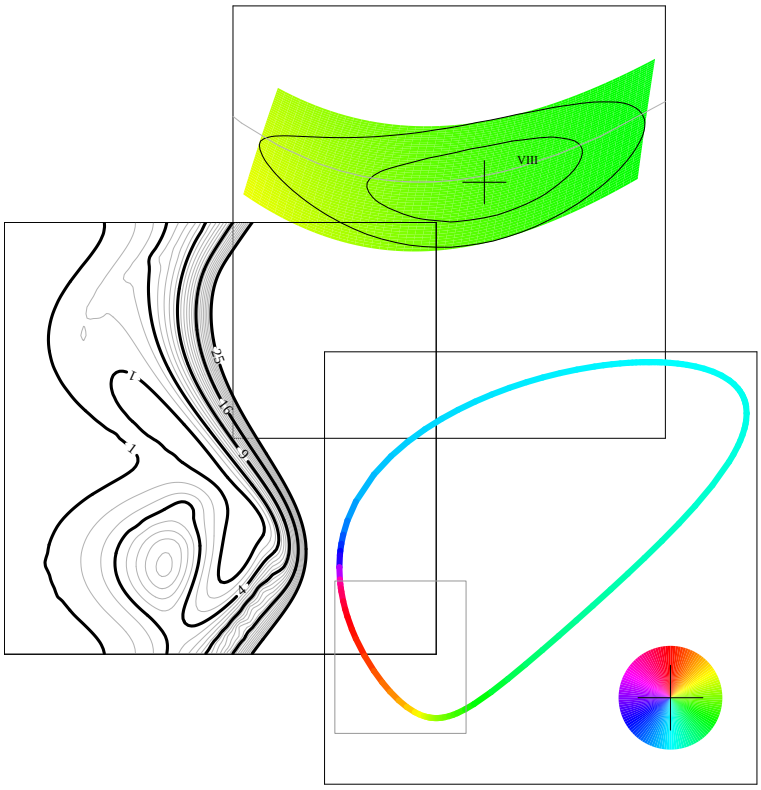

Technische Universität München
Physik-Department
Institut für Theoretische Physik
Prof. Dr. Manfred Lindner

Technische Universität München
Physik Department
Institut für Theoretische Physik T30d
Univ.-Prof. Dr. M. Lindner

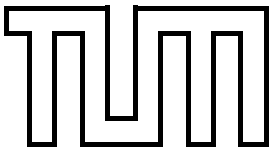

Three Flavour Effects

in

Future Neutrino Oscillation Experiments

Dipl.-Phys. Univ. Patrick Huber

Vollständiger Abdruck der von der Fakultät für Physik der Technischen Universität München zur Erlangung des akademischen Grades eines

Doktors der Naturwissenschaften (Dr. rer. nat.)

genehmigten Dissertation.

Vorsitzender: Univ.-Prof. Dr. Lothar Oberauer

Prüfer der Dissertation:

1. Univ.-Prof. Dr. Manfred Lindner
2. Univ.-Prof. Dr. Andrzej J. Buras

Die Dissertation wurde am 16. September 2003 bei der Technischen Universität München eingereicht und durch die Fakultät für Physik am 23. Oktober 2003 angenommen.

To Angelika

Contents

Chapter 1

Introduction

Neutrino physics has become one of the most active areas of research in particle physics. There are many reasons for this development, one of the most important is that neutrino physics is a data driven field – for several years now, new data are pouring at an astounding rate. It began in 1987 with the first detection of supernova neutrinos. Although only 19 events were observed [1], they allowed to confirm the standard picture of core-collapse supernovæ. Furthermore those 19 events also constitute the detection of the oldest neutrinos ever; they were produced some 150 000 years ago. The fact that there were detectable neutrinos after this time allows to put stringent bounds on the neutrino life time. Furthermore the environment at the production site was a very special one – a dense and hot proto-neutron star. This offers the possibility to derive strong bounds on any additional interaction neutrinos could have. A comprehensive review on the properties of neutrinos which can be deduced from supernovæ is given in [2].

In 1998 Super-K's atmospheric neutrino data [3] gave the first clear evidence for neutrino oscillation. This result was a real turning point for neutrino physics. Neutrino oscillation implies that neutrinos do have a mass and the finding that the mixing angle is large was completely unexpected. In analogy to the quark sector the common belief was that if neutrinos mixed at all then the mixing angles should be small. The importance of the Super-K result is that it is the first strong evidence for physics beyond the Standard Model. With the Super-K result the number of publications per year containing the word neutrino in their title four-folded[1].

The year 2002 was an annus mirabilis for neutrino physics. The solar neutrino puzzle was proven to be due to the properties of the neutrino and not of the Sun. The neutral current data of SNO [4] yielded an independent determination of the total flux of active neutrinos from the Sun and in combination with other solar neutrino data proved that solar neutrinos undergo a flavour transition. Kamland [5] provided an independent check of the oscillation hypothesis by using reactor neutrinos and constrained the mixing parameters to the so called LMA solution. These two results together are extremely difficult to explain other than by neutrino oscillation. Also the evidence for oscillation in

[1] According to the `hep-ph` preprint server of `arXive.org`

atmospheric neutrinos could be confirmed independently by K2K [6], which is the first long baseline experiment. Furthermore two pioneers of neutrino physics were awarded the Nobel prize. Masatoshi Koshiba was awarded one fourth of the prize for the detection of neutrinos from a supernova and Ray Davis Jr. was awarded another fourth for his detection of solar neutrinos. A relatively recent review on the topic of neutrino oscillations in general is given in *e.g.* [7].

Massive neutrinos offer a variety of fascinating new phenomenology beyond oscillation, especially in cosmology. In one scenario, called leptogenesis, heavy neutrinos are responsible for the baryon asymmetry of the Universe. Light neutrinos have a sizable impact on structure formation, *i.e.* the mechanism by which the homogeneous early Universe developed the rich structure which is observed today. A rather extensive review on the wide area of neutrinos in cosmology is given in [8]. Cosmology has undergone a tremendous increase in the available experimental data as well and is now entering a phase of high precision measurements. With the data of WMAP [9] and the 2dFGRS [10] the cosmological limits on the masses of neutrinos are already slightly better than the laboratory bounds, see *e.g.* [11].

The Standard Model is in a paradox situation – it is extremely successful in describing elementary particles and their interactions and still it is strongly believed to be incomplete. It seems to be the correct description of the physics which can be observed at low energies but it is obvious from its structure that it cannot be correct up to the very highest energies. This has inspired many attempts to provide a convincing model for the physics beyond the Standard Model. These attempts strongly suffered from the fact that no deviation from the Standard Model had been found before the discovery of neutrino flavour transitions. The discovery of neutrino oscillations requires only a minor change in order to accommodate three massive neutrinos, three mixing angles and one Dirac-type CP-phase. Neutrinos are the only neutral fundamental fermions and therefore a Majorana mass term can appear in the Lagrangian. In that case also two Majorana phases enter into the extension of the Standard Model. The mixing of neutrinos is very different from that of quarks, since there are two large mixing angles. Neutrino masses are also peculiar because they are at least five orders of magnitude smaller than the mass of the electron. These facts pose a major challenge to any theory of neutrino masses and mixings: Why are neutrino masses so small? Why is the neutrino mixing pattern so different from that of the quarks? What is the pattern of neutrino masses? The observation of neutrino oscillation has stipulated a large effort to answer these questions. The smallness of neutrino masses is usually accounted for by the so called see-saw mechanism, *i.e.* heavy right handed singlet neutrinos with masses around the GUT-scale suppress the neutrino mass to very small values. In such a scenario neutrino masses are a probe of very high energy scales which may otherwise be not accessible. It turns out that it is far from trivial to construct a theory which can account for the observed mixing pattern, *i.e.* predict two large mixing angles. Some theories are at least able to avoid open conflict with the existing oscillation data[2]. But it seems that there is a far

[2]To what extent this signifies an explanation or even a deep understanding of the problem

way to go to fully understand neutrino masses and mixings. This may require a theory of flavour, which basically should shed light onto the question why there are three families. For some recent reviews on the vast amount of literature on these topics see [12].

The next step is to consolidate the general picture and to prove oscillation unambiguously by observing the typical energy dependence. SNO is expected to yield improved neutral current data within the next few months. Also Kamland is continuing to take data and may very well prove oscillation for the solar mass splitting. K2K is taking more data and will thus test the atmospheric oscillation with a better precision. There are several experiments under construction in order to prove the atmospheric oscillation and to narrow down the allowed ranges for the mass splitting, the most important being Minos and CNGS. Finally Miniboone will thoroughly test the results of LSND. The most recent review of neutrino physics is to be found in [13], which also contains an extensive bibliography.

In order to develop and finally test a theory of neutrino masses and mixings it will be essential to further improve on the knowledge of not only the oscillation parameters but also the absolute mass scale of neutrinos. Furthermore the observation of neutrino-less double β-decay could shed some light onto the Majorana nature of neutrinos. The theoretical motivation, the current status and future experiments for neutrino-less double β-decay are reviewed in [14], whereas the prospects of determining the absolute mass scale are reviewed in [15]. The issue of how to improve the knowledge on the oscillation parameters beyond what will be achieved by the next generation experiments is the topic of this work.

Scope & structure of this work

As indicated in the title of this work the focus is on three flavour effects in future neutrino oscillation experiments. Three flavour effects occur whenever the two mass scales of the solar and the atmospheric oscillation interfere, *i.e.* an experiment is sensitive to effects of both mass splittings. All of the existing experiments and also all of the already approved experiments are sensitive to only one mass scale. The term "future" in the title thus refers to experiments which have not been approved yet, albeit the different kinds of experiments considered in this work have very different time scales. The first ones could be taking data within a few years, whereas the most sophisticated ones may require more than ten years before becoming operational. Three flavour effects have not the same relevance to all measurements connected to neutrino oscillation. They do not play an essential role in the precision determination of the mass splittings or the two large mixing angles. For the measurement of the small mixing angle, however, they are crucial and in many circumstances completely determine the potential of an experiment. In a certain class of experiments it is possible to determine the mass hierarchy of the neutrinos by exploiting so called matter effects. In that case three flavour effects are large and have to be included in order to evaluate the performance of an experiment. The most important

is left to the judgment of the reader.

instance where three flavour effects are essential is leptonic CP-violation. A prerequisite for observing leptonic CP-violation is that the interference of the two mass scales is observable. Thus the discussion and comparison of the different experiments is performed for the limiting sensitivity to the small mixing angle, for the sensitivity to the mass hierarchy and for the potential to discover leptonic CP-violation. The interference of two mass scales introduces a considerable degree of complexity in the analysis of experimental data and the central topic of this work is to explore and understand this complexity in its full extent in order to arrive at quantitatively precise results for the physics potential of each experiment.

In the first part of chapter 2 a very basic introduction to the quantum mechanics of neutrino oscillation, including matter effects, is given. In the second part of chapter 2 the existing evidence for neutrino oscillations is reviewed with a special focus on the historical development of the field and the status quo of neutrino oscillations is described. Chapter 3 deals with the mathematical structure of oscillation probabilities and the existence of multiple solutions. Some new analytical results on degeneracies are presented as well. This chapter furthermore provides a showcase of the general analysis strategy used in deriving the results, which are presented in chapter 5. The various experiments studied in this work and their simulation are introduced in chapter 4. There, also the standard values for the oscillation parameters as used for the calculation of the results in chapter 5 are defined. The final results of this work are presented in chapter 5. The performance of the various setups is compared with respect to the possibility to determine the small mixing angle, the mass hierarchy and the value of the CP-phase. Finally there is a conclusion and an outlook in chapter 6. In appendix A the more technical details of the experiment simulation are discussed and the numerical values used for the individual setups are given. Appendix B consists of a detailed description of the statistical methods used in this work and certain varieties of $\Delta\chi^2$.

The reader who is familiar with neutrino oscillations may wish to skip chapter 2. Those who are either more interested in a global picture or are familiar with the various ideas for future experiments can also skip chapter 4. On the other hand chapter 3 and the appendices may prove a useful resource for those readers who are working in the field of future neutrino oscillation experiments.

Chapter 2

Primer on neutrino oscillations

The following chapter will give in its first part an introduction to the basic formalism of neutrino oscillations. First the simple case of two flavour oscillations in vacuum will be introduced. Starting from this, matter effects and the MSW-resonance are discussed, again in the two neutrino framework. This is then generalized to the three neutrino case where also the standard parameterization of the leptonic mixing matrix is presented. The second part of this chapter deals with the experimental evidence for neutrino oscillations and the current global understanding of oscillations. Finally the most recent best fit values and errors on the neutrino mixing parameters are given and compared to the existing knowledge in the quark sector.

2.1 Basic vacuum oscillations

Neutrino oscillation is a simple quantum mechanical effect, which can be illustrated by a two-state system and was first[1] discussed in [17]. Assuming $|\nu_i\rangle$ to be the stationary eigenstates of the free Hamiltonian the time evolution of the state $|\nu_i(t)\rangle$ is given by

$$|\nu_i(t)\rangle = e^{-iE_i t}|\nu_i\rangle\,. \tag{2.1}$$

In the context of neutrino oscillations the eigenstates of the Hamiltonian are called mass eigenstates, since the Hamiltonian $\hat{H}$ is proportional to the diagonal matrix $\mathrm{diag}(m_1^2, m_2^2)$, where m_1 and m_2 denote the masses of the states $|\nu_1\rangle$ and $|\nu_2\rangle$. Neutrinos are produced and detected with a definite flavour, *i.e.* as eigenstates of the weak interaction, which are denoted by $|\nu_\alpha\rangle$. These weak eigenstates do not necessarily coincide with the mass eigenstates. Therefore a linear superposition of mass eigenstates may be created in the neutrino production and the transformation between the two bases is determined by a unitary matrix [18], which is a 2×2 matrix in the two neutrino case

Mass eigenstates & weak eigenstates

$$|\nu_\alpha\rangle = \sum_i U^*_{\alpha i}|\nu_i\rangle\,. \tag{2.2}$$

[1] Actually, neutrino oscillation was for the very first time discussed in [16], but there the oscillation between ν and $\bar{\nu}$ was considered only, since ν_μ and ν_τ were not known at that time.

The general vacuum oscillation probability is then given by[2]

$$P_{\nu_\alpha \to \nu_\beta} = \left| \langle \nu_\beta | e^{-iE_i t} | \nu_\alpha \rangle \right|^2 = \sum_{ij} U_{\alpha j} U^*_{\beta j} U^*_{\alpha i} U_{\beta i} e^{-i \frac{\Delta m^2_{ij} L}{2E}} , \tag{2.3}$$

where $\Delta m^2_{ij} = m^2_i - m^2_j$ is called mass splitting. Thus neutrino oscillations are only sensitive to mass differences but *not* to the absolute neutrino mass scale. In the case of two neutrinos the unitary matrix U can be parameterized in the following way

$$U = \begin{pmatrix} \cos\theta & \sin\theta \\ -\sin\theta & \cos\theta \end{pmatrix} , \tag{2.4}$$

where θ is called mixing angle. Inserting this in equation 2.3 yields the following simple formulæ for the oscillation probabilities

$$\begin{aligned} P_{\nu_\alpha \to \nu_\beta} &= \sin^2 2\theta \sin^2 \left(\frac{\Delta m^2 L}{4E} \right) , \\ P_{\nu_\alpha \to \nu_\alpha} &= 1 - \sin^2 2\theta \sin^2 \left(\frac{\Delta m^2 L}{4E} \right) , \end{aligned} \tag{2.5}$$

Appearance & disappearance

where L is the distance traveled by the neutrinos and is usually called baseline and E is the neutrino energy. $P_{\nu_\alpha \to \nu_\beta}$ is called appearance probability, since the flavour β appears as final state and analogously $P_{\nu_\alpha \to \nu_\alpha}$ is called disappearance probability, since the flavour α disappears. Obviously the two probabilities fulfill the unitarity condition $P_{\nu_\alpha \to \nu_\beta} + P_{\nu_\alpha \to \nu_\alpha} = 1$. Moreover $P_{\nu_\alpha \to \nu_\beta}$ is invariant under time reversal and CP-conjugation, since in the two neutrino case there is no CP-violation in neutrino oscillations for the same reason as there would be no CP-violation in the quark sector if only two families existed [19].

Signatures of Δm^2 and θ

The parameters Δm^2 and θ are fundamental constants like the electron mass or the Cabibbo-angle. However the baseline and neutrino energy can in principle be chosen by the experimental setup. The signature for the value of the mixing angle in an appearance experiment, *i.e.* an experiment which observes $P_{\nu_\alpha \to \nu_\beta}$, is given by the height of the oscillation peak, which is also indicated by the vertical arrow in the left hand panel of figure 2.1. The value of Δm^2 is given by the position of the oscillation peak as a function of the energy, which is shown as horizontal arrow. For a disappearance experiment the oscillation peak becomes an oscillation dip as shown in the right hand panel of figure 2.1. The depth of the dip is now the signature for the mixing angle as indicated by the vertical arrow. The position of the dip yields the value of the mass splitting and is indicated by the horizontal arrow.

Systematical limitations

For both kinds of experiments, appearance and disappearance, there can be a correlation between the measured values of Δm^2 and θ, *i.e.* an error on the determination of one parameter introduces an additional uncertainty on the other parameter. Furthermore an experiment needs to have enough energy resolution to clearly determine the position of the peak, otherwise the experiment sees an energy independent signal proportional to $1/2 \sin^2 2\theta$. Another important factor for the determination of the mass splitting is the energy calibration of the

[2] in the ultra-relativistic limit, $m_i \ll E_\nu$

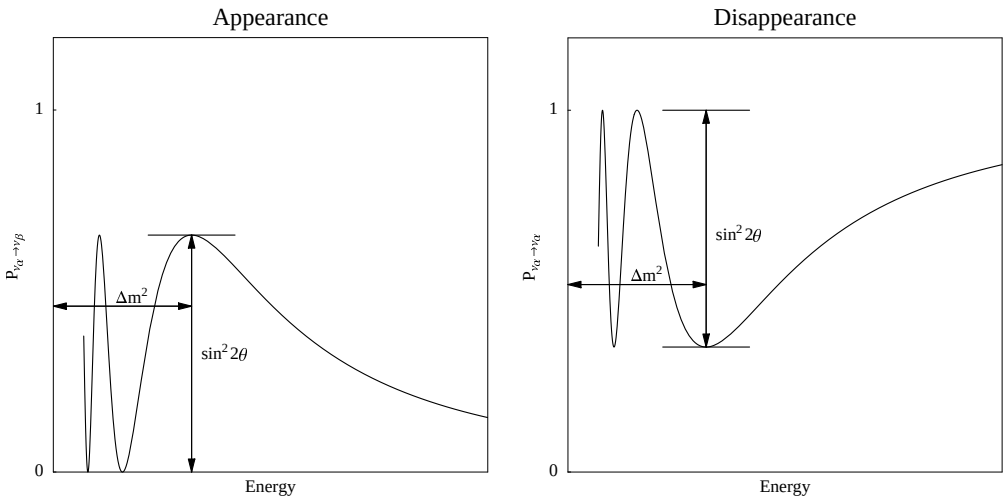

Figure 2.1: *The oscillation probability as a function of the energy in arbitrary units. The left hand panel shows the signature of the mixing angle θ (vertical arrow) and the one of the mass splitting Δm^2 (horizontal arrow) in the case of an appearance experiment, whereas the right hand panel shows the signatures in the case of a disappearance experiment.*

detector – any error on the absolute energy scale directly translates into an error in the position of the oscillation peak or dip. The major difference between the two possible experiments is that an appearance experiment is much more sensitive to small values of θ, because the measurement is performed relative to zero, whereas a disappearance experiment measures relative to unity. This implies a different behavior of the two types of experiments with respect to certain systematical errors. On the one hand, the level of background is crucial for an appearance experiment, since a large background reduces the sensitivity to small values of θ. On the other hand, the total normalization is vital for a disappearance measurement, because a large normalization error makes it impossible to detect deviations from unity. These differences become very obvious in chapter 5, where the performance of both kinds of experiments is compared.

2.2 Matter effects

In many cases the propagation of neutrinos does not take place in vacuo but in matter. Although the interaction of neutrinos with matter is tiny, matter can have a substantial impact on the oscillation probabilities. Matter effects in neutrino oscillations will again be illustrated within a two neutrino framework, where the principle features are already visible but the algebra stays simple. The weak interaction couples the neutrinos to matter and besides hard scattering events there is also coherent forward scattering in very much the same fashion as for visible light traveling through glass. The point is that the coherent forward scattering amplitudes are not the same for all neutrino flavours, since

ordinary matter is made of particles of the first family and does specifically not contain muons or tau-leptons. All flavours have the same amplitude for neutral current reactions but the electron neutrinos have an additional contribution due to charged current reactions. The electron (anti-)neutrino is the only one which can scatter coherently with the electrons in the matter via the charged current and this yields an additional contribution to the potential A for electron (anti-)neutrinos of

$$A = (-)2\sqrt{2}\, G_F\, n_e\, E\,, \tag{2.6}$$

where G_F is the Fermi coupling constant, n_e is the electron density[3] and E is the neutrino energy. The minus sign is for anti-neutrinos. In matter the Schrödinger equation for neutrino propagation is now modified by a term containing the potential A and is in the flavour basis given by

$$i\frac{d}{dt}\begin{pmatrix}\nu_\alpha\\ \nu_\beta\end{pmatrix} = \frac{1}{2E}\left[U\begin{pmatrix}m_1^2 & 0\\ 0 & m_2^2\end{pmatrix}U^\dagger + \begin{pmatrix}A(t) & 0\\ 0 & 0\end{pmatrix}\right]\begin{pmatrix}\nu_\alpha\\ \nu_\beta\end{pmatrix}. \tag{2.7}$$

For a constant matter density the problem reduces to a stationary one and the solution can be obtained by a simple diagonalization of the Hamiltonian. The result is a mapping of the vacuum parameters to new parameters in matter, which carry the subscript m:

$$\begin{aligned}\Delta m^2_{\mathrm{m}} &= \Delta m^2 C_\pm = \Delta m^2\sqrt{\left(\frac{|A|}{\Delta m^2}\mp\cos 2\theta\right)^2 - \sin^2 2\theta}\,.\\ \sin^2 2\theta_{\mathrm{m}} &= \sin^2 2\theta\, C_\pm^{-2}\,,\end{aligned} \tag{2.8}$$

where the minus sign is for neutrinos, whereas the positive sign is for anti-neutrinos. At $|A| = \Delta m^2$ the so called MSW-resonance occurs [20], *i.e.* any finite value of θ is resonantly enhanced to maximal mixing $\theta = \pi/4$. This resonance happens for neutrinos in the case of a positive Δm^2 and for anti-neutrinos in the case of a negative Δm^2. In this way the oscillation probability depends now on the sign of Δm^2. The sign of Δm^2 is determined by the mass hierarchy, *i.e.* whether ν_1 is lighter than ν_2 (normal hierarchy) or heavier (inverted hierarchy). In vacuo a change of the sign of Δm^2 leaves the oscillation probability in the two neutrino case invariant as it can be seen from equation 2.3. The resonance condition $|A| = \Delta m^2$ can be recast in the following useful form

Matter effects can distinguish the mass hierarchy

$$E_{\mathrm{res}} = 8.6\,\mathrm{GeV}\left(\frac{|\Delta m^2|}{2\cdot 10^{-3}\,\mathrm{eV}^2}\right)\cdot\left(\frac{2.8\,\mathrm{g\,cm^{-3}}}{\rho}\right). \tag{2.9}$$

Thus the resonance in the upper Earth mantle ($\rho = 2.8\,\mathrm{g\,cm^{-3}}$) occurs at roughly 9 GeV for a value of Δm^2 around $2\cdot 10^{-3}\,\mathrm{eV}^2$. In matter the oscillation probabilities are even in the two neutrino case no longer invariant under CP-conjugation, since the matter potential breaks this symmetry, because it is due to matter and not anti-matter.

[3] The electron density is connected to the matter density via the electron fraction Y_e, which is taken to be 0.5.

2.3 Three flavours

With three neutrino flavours the mixing matrix can be parameterized by three complex rotations in the following way:

$$U = \begin{pmatrix} 1 & 0 & 0 \\ 0 & c_{23} & s_{23} \\ 0 & -s_{23} & c_{23} \end{pmatrix} \begin{pmatrix} c_{13} & 0 & s_{13}e^{-i\delta} \\ 0 & 1 & 0 \\ -s_{13}e^{i\delta} & 0 & c_{13} \end{pmatrix} \begin{pmatrix} c_{12} & s_{12} & 0 \\ -s_{12} & c_{12} & 0 \\ 0 & 0 & 1 \end{pmatrix} \begin{pmatrix} 1 & 0 & 0 \\ 0 & e^{i\phi_1} & 0 \\ 0 & 0 & e^{i\phi_2} \end{pmatrix}, \tag{2.10}$$

where s_{ij} stands for $\sin\theta_{ij}$ and analogously c_{ij} stands for $\cos\theta_{ij}$. The phases ϕ_1 and ϕ_2 are Majorana-phases and do not enter into the oscillation probabilities [21], however they can have phenomenological consequences, *e.g.* in neutrino-less double beta decay [22]. The most general parameterization of neutrino mixings can be found in [23]. In the case of three neutrinos there are two mass splittings denoted by Δm^2_{21}, which corresponds to the mass splitting that is together with θ_{12} responsible for the effects in solar neutrinos and Δm^2_{31} that together with θ_{23} governs the oscillation of atmospheric neutrinos. In the three family case there can be CP-violation in the same way as in the quark sector. The size of all CP-violating effects is proportional to $J_{\rm CP}$ [24] whose value in the above parameterization is

Six parameters

$$J_{\rm CP} = \frac{1}{8}\cos\theta_{13}\sin 2\theta_{13}\sin 2\theta_{23}\sin 2\theta_{12}\sin\delta\,. \tag{2.11}$$

Therefore any CP-violating effect is suppressed by the smallest of the mixing angles, which is θ_{13}. In matter the CP-phase is not the only source of CP-violation since there are additional contributions due to the CP-asymmetry of matter. Furthermore there can be matter-induced T-violation for asymmetric matter density profiles, which however does not play a role for any of the setups discussed in this work [25]. The detailed form of the oscillation probabilities including matter effects and their phenomenological consequences will be discussed in chapter 3.

θ_{13} suppresses CP-effects

2.4 Present status of neutrino oscillations

All existing data for neutrino oscillations can separately be analyzed in an effective two neutrino framework, *i.e.* the data do not indicate any genuine three flavour effects, in particular all data can be accommodated without any complex entries in the mixing matrix. The reason for this is that there is a pronounced hierarchy of mass splittings $|\Delta m^2_{21}| \ll |\Delta m^2_{31}|$ and that the angle θ_{13} which couples the two oscillations is small. Therefore the presentation of the current knowledge on neutrino mixing parameters can be divided into three subsets: oscillations associated with Δm^2_{21}, oscillations associated with Δm^2_{31} and the non-observation of θ_{13}. Finally some comments on the status of four neutrino scenarios with respect to the existing data will be made.

Solar parameters – Δm^2_{21} and θ_{12}

History of early solar models

The question of how the Sun produces its energy has been a long standing issue of debate. The earliest scientific theories of the energy production in the Sun date back to about 1840 and the most prominent of these theories was that the Sun gains energy by converting gravitational energy into heat via contraction. Among the proponents of this theory were Kelvin [26] and Helmholtz [27]. The flaw of this theory is that it yields an upper bound on the age of the sun of approximately 20 million years. In 1920 it was realized by Eddington inspired by the latest results of Aston [28] on the mass difference of four Hydrogen atoms to one Helium atom that the Sun may produce its energy by nuclear fusion. Bethe and Weizsäcker proposed then in 1939 a detailed reaction chain for the fusion processes in the Sun [29]. At this point it was clear that electron neutrinos would be produced by the nuclear reactions in the Sun. An overview of the historical development of early solar models is given in [30]. The standard solar model of today has improved a lot in many aspects to early calculations and has become quite complex. However it has found an excellent confirmation by helioseismology. Helioseismology studies the vibrations of the Sun's surface by means of the Doppler-shift of certain spectral lines when the surface moves up and down. This information can be used to infer the speed of sound in the interior of the Sun in pretty much the same fashion as it is done in the seismology of the Earth. For a recent review on the topic see [31].

The solar neutrino puzzle

The solar neutrino puzzle started to emerge in the late sixties and it took nearly forty years to resolve it. The first data on solar neutrinos obtained in the Homestake experiment [32] already displayed a difference of roughly a factor of 2.5 between the measured flux and the prediction [33], albeit at a very low confidence level. The first detection of solar neutrinos was awarded with the Nobel prize in 2002. As more and more data were gathered, the discrepancy between the observed neutrino flux and the theoretically predicted flux increased as it can be seen in figure 2.2. With the advent of the first solar neutrino data from Kamiokande [34] in 1989 the evidence for the solar neutrino deficit was strengthened. This development continued with the first data from Sage [35] in 1991 and from Gallex [36] in 1994. The next major breakthrough in the observation of solar neutrinos was the high quality spectral data delivered by the successor experiment of Kamiokande, Super-K [37], in 1999. The culmination and solution to the solar neutrino puzzle then was achieved by the neutral current data of the SNO experiment [4] in 2002. The neutral current data allow to precisely determine the overall flux of all active neutrino flavours from the Sun and they are found to be in excellent agreement with the predictions. Thus the only possible conclusion is that the electron neutrinos from the Sun undergo a transition to another active flavour. This conclusion can be drawn at the very high confidence level of $5.3\,\sigma$, *i.e.* the probability that this result is a statistical fluctuation is approximately 1 in 10^7. This by itself does not prove that the flavour transition is due to oscillation and there can be other mechanisms like spin-flavour precession [38] or non-standard neutrino properties [39]. A nice review on the compatibility of the solar data and various mechanisms for flavour transitions including oscillations is for example given in [40]. A very detailed

SNO's neutral current data

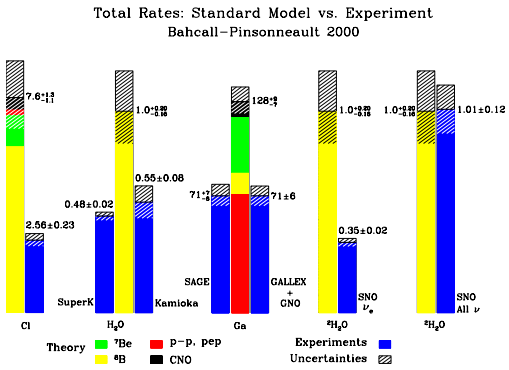

Figure 2.2: *Comparison of the measured and predicted total rates of solar neutrinos. This figure is taken from* [42].

description of the impact of the various pieces of evidence and systematical errors is given in [41].

The Kamland experiment, however, provides an independent check of the results of the solar neutrino experiments. Kamland measures the survival probability of electron anti-neutrinos produced in various nuclear power plants in Japan. This allows a precise test of the solar oscillation hypothesis without any astrophysical uncertainties. The first Kamland data were published in 2002 in [5]. The Kamland result led to a flood of papers [43][4] analyzing the Kamland data in combination with existing solar data. In all the papers [43] basically the same result was found, namely that the so called MSW-LMA oscillation solution gives the best fit and that any other known mechanism can play at most a sub-leading role in the explanation of the solar neutrino deficit. The remaining parameter ranges derived by a fit to all existing data [44] are at $3\,\sigma$ given by [43]

Kamland confirms the oscillation hypothesis

$$\Delta m^2_{21} = +7^{+23}_{-3} \cdot 10^{-5}\,\mathrm{eV}^2\,, \quad \sin^2 2\theta_{12} = 0.8^{+0.2}_{-0.2}\,. \tag{2.12}$$

Atmospheric parameters – Δm^2_{31} and θ_{23}

In the Earth's atmosphere neutrinos are produced by reactions of cosmic radiation and the nuclei in the atmosphere. The main component of the cosmic radiation at the relevant energies are protons, which in turn produce via strong interactions mesons. Those mesons are mainly pions and undergo the following decay chain

$$\pi^- \rightarrow \begin{array}{l} \mu^- \\ +\bar{\nu}_\mu \end{array} \rightarrow e^- + \bar{\nu}_e + \nu_\mu\,. \tag{2.13}$$

This yields a ratio of muon flavour to electron flavour neutrinos of 2. It was realized in 1960 that the observation of atmospheric neutrinos could be possible using a large water Cherenkov detector deep underground [45]. The ratio of course is not exactly 2 since there are many subtleties involved in the prediction of the atmospheric neutrino flux like the composition of the primary cosmic rays, the incoming flux of particles *a.s.f.*. However there exist complete models

[4] NB – some of these papers appeared before the Kamland data were publicly available

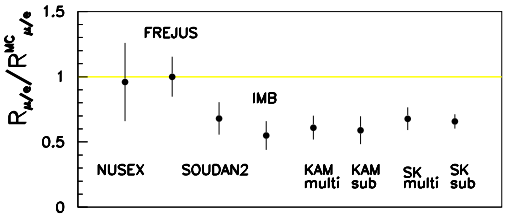

Figure 2.3: *Comparison of the measured and predicted ratio of muon flavour neutrino to electron flavour neutrinos. This figure is taken from* [7].

for computing the neutrino flux of each flavour with an accuracy of $\sim 20\%$. The ratio of electron flavour to muon flavour neutrinos is known with a better precision of $\sim 5\%$, since in the ratio many uncertainties cancel. For an extensive review on the calculation of atmospheric neutrino fluxes see [46].

The atmospheric neutrino anomaly

The first detection of an atmospheric neutrino was independently reported by two groups [47] in 1965. The first sign that something may be amiss with atmospheric neutrinos was found by the IMB experiment [48] in 1986. The number of so called stopping muons was too low compared to the predictions. Further support for these results came in 1988 by the data of the Kamiokande experiment [49]. The situation became more confusing when the Frejus experiment [50] found a ratio consistent with the theoretical expectation in 1990. As more and more data were accumulated by IMB and Kamiokande, and as the data of Soudan [51] and Macro [52] became available the evidence for some strange phenomenon in atmospheric neutrinos increased strongly. This is also to be seen in figure 2.3, where the double-ratio of the measured muon flavour neutrino to electron flavour neutrino ratio to the predicted value of this ratio is shown. Finally in 1998 the Super-K collaboration presented their now famous result [3] – atmospheric neutrinos do oscillate. The key to this statement is that Super-K has a sufficient number of events to observe the baseline dependence of the ratio of electron flavour to muon flavour neutrinos. The neutrinos coming from above, who have traveled $\sim 20\,\mathrm{km}$, show the expected ratio of 2, whereas the neutrinos coming from below, who have traveled $\sim 13\,000\,\mathrm{km}$, show a strong decrease in the ratio to about 1. This can be accounted for by an oscillation of muon neutrinos to tau neutrinos [53].

Neutrinos do oscillate

The initial evidence of Super-K was further strengthened by the increasing size of the event sample in Super-K and by the results of the first long baseline experiment K2K [6]. The global analysis of all atmospheric data [3, 54] found a very good agreement between the different data sets [55, 56]. The best fit values and the allowed range used to be given at $3\,\sigma$ by [57, 58]:

$$|\Delta m^2_{31}| = 3^{+3}_{-2} \cdot 10^{-3}\,\mathrm{eV}^2\,, \quad \sin^2 2\theta_{23} = 1^{+0}_{-0.2}\,. \tag{2.14}$$

An excellent summary of the atmospheric neutrino anomaly is given in chapter V of [7]. Furthermore it turns out that the interpretation of the atmospheric neutrino anomaly in terms of active-active oscillations is very robust. A pure conversion to sterile neutrinos is excluded at more than $5\,\sigma$. In fact this robustness allows to constrain exotic scenarios like non-standard interactions of

neutrinos [59] or de-coherence [58]. Still also in the case of atmospheric neutrinos, oscillation has not been unambiguously proven by observing the typical energy dependence.

Latest update

During the final stage of this work the Super-K collaboration has presented an updated analysis of their existing data [60] and the best fit values have shifted according to a preliminary combined analysis of the existing data [61]. The most recent best fit values and allowed ranges at $3\,\sigma$ are [61]

$$|\Delta m^2_{31}| = 2^{+1.2}_{-0.9} \cdot 10^{-3}\,\mathrm{eV}^2\,, \quad \sin^2 2\theta_{23} = 1^{+0}_{-0.2}\,. \tag{2.15}$$

The global picture

The two instances of a very strong evidence for neutrino oscillations have been presented and discussed in the previous two sections. There remains now the combination of these two pieces with the other existing data to a global picture. There has been a long row of experiments which did not observe any neutrino transitions. A series of reactor neutrino experiments has provided stringent bounds on the disappearance of electron anti-neutrinos [62–65] (see also section A.2.1). Furthermore a series of short baseline accelerator experiments has provided rather tight bounds on the transition of ν_μ and ν_e to ν_τ [66].

However there also has been one experiment observing evidence for neutrino oscillation – LSND. The results of this experiment indicate that there is a third mass splitting $\Delta m^2_{\mathrm{LSND}}$ in the range $0.2 - 10\,\mathrm{eV}^2$ [67]. The Karmen experiment [68] on the other hand excludes a large part of the parameter region claimed by LSND. In a combined analysis of both data sets there still remains a combined allowed region [69]. The third mass splitting cannot be accommodated within a three neutrino flavour framework. Basically two possible solutions exist – either there are more than three neutrinos, which means that the additional neutrinos are sterile in order not to create a conflict with the decay width of the Z^0 (see *e.g.* [70]), or there is a huge CPT-violation, which would make the mass splittings of neutrinos and of anti-neutrinos independent of each other. Both solutions suffer from phenomenological problems, *i.e.* they do not fit the existing data very well.

The LSND anomaly

A sterile neutrino?

First the four neutrino case is discussed. As it was shown in the previous two sections each of the data sets from atmospheric and solar neutrinos excludes a pure sterile oscillation, but some admixture may be admitted. In a combined analysis however it turns out that for the so called $2+2$ scheme the parameter goodness of fit[5] is $1.3 \cdot 10^{-6}$ [72], *i.e.* the $2+2$ scheme is completely ruled out. This is due to the fact that each of the two data sets disfavors a sterile neutrino and the tension between the two data sets is too large for the $2+2$ scheme. In the so called $3+1$ scheme the situation is somewhat different, here the parameter goodness of fit is $5.6 \cdot 10^{-3}$ [72]. Thus the $3+1$ scheme cannot be considered completely ruled out but it is strongly disfavored basically on account of the existing short baseline data. In [72] it was furthermore shown that cosmological constraints on the absolute mass scale of the neutrino further reduce the allowed region in the parameter space for the $3+1$ scheme. Recently

[5] For an exact definition see [71].

a $3+2$ scheme has been proposed to account for the result of LSND. In [73] a combined analysis of LSND and the short baseline data was performed and it was found that the $3+2$ scheme fits the data reasonably well[6].

CPT-violation?

The idea of a large CPT-violation to account for the LSND result was pursued in detail in *e.g.* [74]. In [75] it is claimed that even in the light of the Kamland data CPT-violation is a viable solution to the LSND result. This claim was refuted in [76]. There it was shown that in a full analysis of all existing data there is no evidence for CPT-violation and the solution to the LSND problem via CPT-violation is rejected at the $3\,\sigma$ level. Summarizing, the status and interpretation of the LSND result stay unclear, therefore the LSND evidence is discarded throughout this work. The result itself will be in any case thoroughly tested by the forthcoming Miniboone experiment [77].

Global analysis

Many authors have performed global analyses of the existing data in a three neutrino framework [55, 78]. The basic trend is that the oscillation of three active flavours describes very well all data except for LSND and that the corrections to the two neutrino analysis of each of the data sets are non-negligible but still small. Taking into account the latest Super-K results [60] the best fit values and ranges at $3\,\sigma$ for the oscillation parameters are [61]

$$\begin{aligned} |\Delta m^2_{31}| &= 2^{+1.2}_{-0.9}\cdot 10^{-3}\,\mathrm{eV}^2\,, & \sin^2 2\theta_{23} &= 1^{+0}_{-0.2}\,,\\ \Delta m^2_{21} &= +7^{+23}_{-3}\cdot 10^{-5}\,\mathrm{eV}^2\,, & \sin^2 2\theta_{12} &= 0.8^{+0.2}_{-0.2}\,,\\ & & \sin^2 2\theta_{13} &< 0.25\,. \end{aligned}$$

There does not exist any information on the mass hierarchy, *i.e.* the sign of Δm^2_{31}, and there is no information on the value of the CP-phase δ either. The current knowledge in the neutrino sector can now be compared to that in the quark sector. For a recent review on the CKM-matrix see [79]. The CKM-parameters and their $3\,\sigma$ ranges are (adopted from [70])

Mixing parameters of the quarks

$$\begin{aligned} \sin^2 2\theta_{23} &= 6.78^{+2.1}_{-1.8}\cdot 10^{-3}\,, & \sin^2 2\theta_{12} &= 1.89^{+0.11}_{-0.10}\cdot 10^{-1}\,,\\ \sin^2 2\theta_{13} &= 5.18^{+34}_{-2.3}\cdot 10^{-5}\,, & \delta &= 1.03^{+0.66}_{-0.66}\,. \end{aligned}$$

A large part of the uncertainty on the CKM-parameters is due to theoretical uncertainties in the translation of measured quantities into the CKM-parameters. Neutrinos are free of these uncertainties, and this may finally allow a more accurate determination of the leptonic mixing matrix than it is possible in the quark sector, *e.g.* the CP-phase may be determined with a four times smaller error than in the quark sector [80]. Also the large mixing angles $\sin^2 2\theta_{23}$ and $\sin^2 2\theta_{12}$ can be determined for neutrinos with an accuracy at the level of percent [81,82], whereas $\sin^2 2\theta_{13}$ can depending on its magnitude be determined with an accuracy at the level of a few 10% [80]. The possible accuracy on the two mass splittings is also expected to reach the percent level [81, 82].

[6] NB – Increasing the number of neutrinos at some point will fit any data.

Chapter 3

Theoretical framework

The aim of this chapter is to provide some theoretical insight into the origin of the surprising complexity of three flavour neutrino oscillations. The discussion is focused on total event rates and therefore serves only as a guideline. The analysis of an experiment including spectral information is considerably more involved and the inclusion of spectral information in an analytical discussion is extremely difficult. However, many of the results and relations derived here are a useful and important ingredient for the full numerical analysis. Furthermore many features of the results presented in chapter 5 can at least qualitatively be understood by using the analytical results of this chapter. Starting with the transition probability for $\nu_e \to \nu_\mu$ a scheme is developed to arrive in a simple way at the total number of events in a given experiment. Based on this method the θ_{13} sensitivity of experiments with one observable is derived. Then experiments with two observables are considered and the solutions to the corresponding equations are presented. From these solutions the so called eight-fold degeneracy is recovered and closed form expressions for it are given. With these expressions it will be shown that in fact there are more than eight degenerate solutions in the most general case. This is illustrated by a simplified analysis of neutrino factory data and the importance of spectral information is highlighted. Finally the question of how to summarize the results of a full analysis in the case of multiple solutions is considered. Some definitions of sensitivities and limits will be given, which are used throughout this work.

3.1 The oscillation probability $P_{\nu_e \to \nu_\mu}$

The fact that the solar mass splitting is within the LMA region implies that three flavour effects are non-negligible in future neutrino oscillation experiments. Exact results for three flavour oscillation probabilities including matter effects have been derived [83]. They are, however, somewhat lengthy and complex and therefore not very well suited for further analytical studies. A way around this is to make use of the fact that we know that $\sin 2\theta_{13}$ is small and that the mass hierarchy parameter $\alpha = \Delta m^2_{21}/\Delta m^2_{31}$ is also small. The possible ranges for these parameters are $0 \leq \sin 2\theta_{13} \leq 0.32$ and $0.004 \leq \alpha \leq 0.2$ (see also equation 4.5). Thus it is possible to obtain an accurate approximation by

expanding the exact result simultaneously in both parameters, *i.e.* for a given order of the expansion $\mathcal{O}$ one has to include all terms of the form $\alpha^m(\sin 2\theta_{13})^n$ where $m+n \leq \mathcal{O}$. This task has been performed in [84, 85], and here the notation of [85] is used. The transition probability $\nu_e \to \nu_\mu$ does not contain any zeroth or first order terms, thus the first non-vanishing terms are of second order[1]

The key to analytical understanding

$$\begin{aligned}
P_{\nu_e\to\nu_\mu} &\approx \sin^2 2\theta_{13}\sin^2\theta_{23}\frac{\sin^2((\hat{A}-1)\Delta)}{(\hat{A}-1)^2} \\
&\pm \alpha \sin 2\theta_{13}\sin\delta_{\mathrm{CP}}\sin 2\theta_{12}\sin 2\theta_{23}\frac{\sin(\Delta)\sin(\hat{A}\Delta)\sin((1-\hat{A})\Delta)}{\hat{A}(1-\hat{A})} \\
&+ \alpha \sin 2\theta_{13}\cos\delta_{\mathrm{CP}}\sin 2\theta_{12}\sin 2\theta_{23}\frac{\cos(\Delta)\sin(\hat{A}\Delta)\sin((1-\hat{A})\Delta)}{\hat{A}(1-\hat{A})} \\
&+ \alpha^2 \cos^2\theta_{23}\sin^2 2\theta_{12}\frac{\sin^2(\hat{A}\Delta)}{\hat{A}^2}\,, \qquad (3.1)\\
\Delta &= \frac{\Delta m^2_{31}L}{4E}\,, \quad \hat{A} = A/\Delta m^2_{31}\,, \\
A &= 2E\sqrt{2}G_F n_e\,, \quad \hat{A}\Delta = 1/\sqrt{2}\,G_F n_e L\,.
\end{aligned}$$

This approximation is based on an expansion of the two neutrino result for the atmospheric Δm^2_{31} and therefore does not cover the solar resonance. This restricts the validity of the above formula to energies larger than [85]:

The validity range of equation 3.1

$$|\hat{A}| \geq |\alpha| \;\Rightarrow\; E \geq 0.45\,\mathrm{GeV}\left(\frac{\Delta m^2_{21}}{10^{-4}\,\mathrm{eV}^2}\right)\left(\frac{2.8\,\mathrm{g\,cm^{-3}}}{\rho}\right). \qquad (3.2)$$

Furthermore the approximation breaks down when the oscillation with the solar frequency can no longer be linearized. This yields an upper bound on the maximum baseline up to which this approximation is valid [85]:

$$\Delta\alpha \leq 1 \;\Rightarrow\; L \leq 8\,000\,\mathrm{km}\left(\frac{10^{-4}\,\mathrm{eV}^2}{\Delta m^2_{21}}\right)\left(\frac{E}{\mathrm{GeV}}\right). \qquad (3.3)$$

The condition on the minimum energy in equation 3.2 is slightly violated in the JHF experiment for the highest possible values of Δm^2_{21} and the lowest energies available in this experiment ($0.4\,\mathrm{GeV} \leq E \leq 1.2\,\mathrm{GeV}$). The approximation is, however, still rather accurate since the baseline of 295 km is too short to develop strong matter effects. The condition on the baseline given by equation 3.3 can be violated only by experiments with the longest baselines, which also tend to have high energies in order to stay tuned with the atmospheric frequency. Therefore this condition is safely fulfilled by all setups studied in this work.

Next we observe that equation 3.1 depends on Δm^2_{21} and $\sin 2\theta_{12}$ only via the product $\Delta m^2_{21}\cdot\sin 2\theta_{12}$. We therefore choose to keep $\sin 2\theta_{12}$ fixed and to increase the variation of Δm^2_{21} accordingly.

[1] In the original version of the formula in [85] also some factors of $\cos\theta_{13}$ appear in the second and third term. However, formally they belong already to the fourth order and can therefore be set to unity, since $\cos x \simeq 1-(\sin 2x)^2/8+\ldots$.

3.2 Application to experiments

In order to predict or at least to understand a posteriori the performance of a given experiment one cannot simply use the oscillation probability as given by equation 3.1 for several reasons. The first and most important is that an experiment does *not* measure the oscillation probability. Instead it measures a convolution of the probability with many factors like neutrino flux spectrum, cross section, detector response, statistical fluctuations, etc. (for a detailed discussion see appendix A). Second, the probability in equation 3.1 depends on all six oscillation parameters and the matter density simultaneously. Thus it is basically impossible to track the influence of all those parameters at the same time in an analytical calculation. However one can introduce an approximate scheme which is simple enough to be illuminating and still retains the essential features of the problem. For quantitative and accurate results it is of course still necessary to employ a full numerical calculation, the results of which will be presented in chapter 5.

An experiment measures event rates, not probabilities

In order to arrive at useful analytical expressions, the first step is to identify those parameters which have the most influence and/or are subject to the largest uncertainties. Δm^2_{31} is currently known roughly within a factor of two. However any experiment looking for the transition $\nu_e \leftrightarrow \nu_\mu$ will also measure at the same time the $\nu_\mu \leftrightarrow \nu_\mu$ transition which allows a very precise determination of $|\Delta m^2_{31}|$ and $\sin^2 2\theta_{23}$ at the percent level [86–89]. Therefore we will regard these two parameters as fixed for our analytical discussion. There is a little caveat: the $\nu_\mu \leftrightarrow \nu_\mu$ transition does not allow to determine the sign of Δm^2_{31} and whether θ_{23} is below or above $\pi/4$. Thus we will also have to keep in mind that there can be another set of solutions to our equations with $\Delta m^2_{31} \to -\Delta m^2_{31}$ [90] and $\theta_{23} \to \pi/2 - \theta_{23}$ [91]. These discrete transformations constitute a part of the so called "eight-fold" degeneracy, a name which was introduced in [92]. This point will be discussed in section 3.5 in more detail.

The matter density is known from geophysics within 5%. This error is only relevant for neutrino factory setups at large values of θ_{13} [80, 81]. Thus the matter density is assumed to be fixed.

The knowledge on Δm^2_{21} and $\sin 2\theta_{12}$ has improved considerably during the last two years [44] and is expected to further improve with the ongoing Kamland [5] experiment. Kamland will finally reduce the error on the product $\Delta m^2_{21} \cdot \sin 2\theta_{12}$ to about 15%. Thus there will remain a sizeable uncertainty in these parameters unless a special purpose experiment is built to reduce the errors further.

There is no knowledge of any kind on the value of the CP-phase. Also the information on $\sin 2\theta_{13}$ is limited and there is only an upper bound, which is given by the results of the Chooz experiment [65].

Three parameters are important – θ_{13}, Δm^2_{21} and δ

We have now identified three parameters which have a large degree of uncertainty: Δm^2_{21},[2] δ_{CP} and $\sin 2\theta_{13}$. Introducing the following notation $\sigma := \Delta m^2_{21}$,

[2] The variation of $\sin 2\theta_{12}$ can be ignored since only the product $\Delta m^2_{21} \cdot \sin 2\theta_{12}$ enters equation 3.1.

$x := \sin 2\theta_{13}$ and $\delta := \delta_{\mathrm{CP}}$, we now can rewrite equation 3.1 as

$$\begin{aligned} P_{\nu_e\to\nu_\mu} &= x^2 \underbrace{\sin^2\theta_{23}}_{=:c_1} \underbrace{\frac{\sin^2((\hat{A}-1)\hat{\Delta})}{(\hat{A}-1)^2}}_{=:f_1(E)} \\ &\pm \sigma x \underbrace{\frac{\sin 2\theta_{12}\sin 2\theta_{23}}{\Delta m^2_{31}}}_{=:c_2} \left(\sin\delta \underbrace{\frac{\sin(\Delta)\sin(\hat{A}\Delta)\sin((1-\hat{A})\Delta)}{\hat{A}(1-\hat{A})}}_{=:f_{2a}(E)} \right. \\ &\quad \left. + \cos\delta \underbrace{\frac{\cos(\Delta)\sin(\hat{A}\Delta)\sin((1-\hat{A})\Delta)}{\hat{A}(1-\hat{A})}}_{=:f_{2b}(E)} \right) \\ &+ \sigma^2 \underbrace{\frac{\cos^2\theta_{23}\sin^2 2\theta_{12}}{(\Delta m^2_{31})^2}}_{=:c_3} \underbrace{\frac{\sin^2(\hat{A}\Delta)}{\hat{A}^2}}_{=:f_3(E)} . \end{aligned} \tag{3.4}$$

Using the new abbreviations we obtain this compact form

$$P(E) = x^2\, c_1 f_1(E) + x\sigma\, c_2 \left[\sin\delta\, f_{2a}(E) + \cos\delta\, f_{2b}(E)\right] + \sigma^2\, c_3 f_3(E)\,. \tag{3.5}$$

It is common to choose the energy to be *e.g.* the mean beam energy [92]. This, however, neglects the energy spread of the beam completely and can in fact give rise to misleading results. It is straightforward to perform the full convolution of each energy dependent part $f_i(E)$ with the cross section, the detector energy response and the efficiency as given in appendix A (the convolution kernel is denoted by $K(E)$ and defined in equation A.6). The advantage in doing so is that one obtains directly the observed number of signal events n

$$\begin{aligned} n = P(E)\otimes K(E) &= x^2\, c_1 \underbrace{f_1(E)\otimes K(E)}_{g_1} \\ &+ x\sigma\, c_2 \left[\sin\delta\, \underbrace{f_{2a}(E)\otimes K(E)}_{g_{2a}} + \cos\delta\, \underbrace{f_{2b}(E)\otimes K(E)}_{g_{2b}}\right] \\ &+ \sigma^2\, c_3 \underbrace{f_3(E)\otimes K(E)}_{g_3} . \end{aligned} \tag{3.6}$$

For any given set of input parameters σ_0, x_0 and δ_0 one thus obtains for the number of observed signal events

$$n_0 = x_0^2\, c_1 g_1 + x_0\sigma_0\, c_2(\sin\delta_0 g_{2a} + \cos\delta_0 g_{2b}) + \sigma_0^2 c_3 g_3\,. \tag{3.7}$$

In contrast to analyzing real data it is necessary to simulate the data, since none of the experiments which are subject of this study has taken data yet. In order to simulate data, a choice for the physical parameters which are used for this purpose has to be made. The subscript 0 will denote throughout this work these input or "true" parameters which have been used to simulate the data of an experiment. It is crucial to keep a clear distinction of those true parameters from the fitted parameters which are used in the analysis of the simulated data. The simulated data are generated with the true parameters $\boldsymbol{\lambda}_0$ and then a fit to these data is performed yielding allowed regions in the space of fitted parameters $\boldsymbol{\lambda}$.

True parameters versus fitted parameters

3.3 One observable

In this section the question: "What do we learn by observing a certain number of events n_0?", will be examined. Or respectively, whether one number is enough to learn about three parameters, *i.e.* how many numbers are needed to pin down x and δ.

To begin with we assume that we have only one measured number n_0. This is *e.g.* the case in the Minos, CNGS, JHF and NuMI experiments, where there is only the $\nu_\mu \to \nu_e$ transition available. Thus we are looking for solutions of this equation

$$n_0 = x^2\, c_1 g_1 + x\sigma\, c_2 \underbrace{(\sin\delta g_{2a} + \cos\delta g_{2b})}_{=:g_2(\delta)} + \sigma^2 c_3 g_3\,. \tag{3.8}$$

In general the solutions of equation 3.8 will constitute a hypersurface in the three dimensional space spanned by σ, x and δ. For fixed δ, equation 3.8 describes an ellipse centered at the origin in the x-σ-plane. In figure 3.1 the set of all points in the σ-x-plane is shown which can fulfill equation 3.8 (grey shaded area). The lower arrow indicates the allowed range for x once σ is known to exactly equal σ_0. In this case still a whole line of solutions remains which is due to the unknown CP-phase δ. Allowing σ to vary freely yields the interval for x which is depicted by the upper arrow. In particular, the value $x = 0$ becomes now part of the allowed range. In this case there would never be a conclusive observation of x not being zero. Obviously, having at least some knowledge on σ helps to reduce the allowed range in x considerably. This result is not surprising since we have tried to derive information on one quantity x which depends on two other variables by only one equation. That we can obtain a finite allowed region at all is due to fact that δ enters the problem only via trigonometric functions.

There may, however, be other sets of solutions due to the discrete transformation mentioned above

Three discrete transformations – four sets of solutions

$$\begin{aligned} \mathcal{T}_s &:= \Delta m^2_{31} \to -\Delta m^2_{31}\,, \\ \mathcal{T}_t &:= \theta_{23} \to \pi/2 - \theta_{23}\,, \\ \mathcal{T}_{ts} &:= \mathcal{T}_s \oplus \mathcal{T}_t\,. \end{aligned} \tag{3.9}$$

These transformations are applied to the coefficients c_i and g_i in equation 3.8. $\mathcal{T}_s$ was discovered in [90], whereas $\mathcal{T}_t$ was first found in [91] and the combination $\mathcal{T}_{ts}$

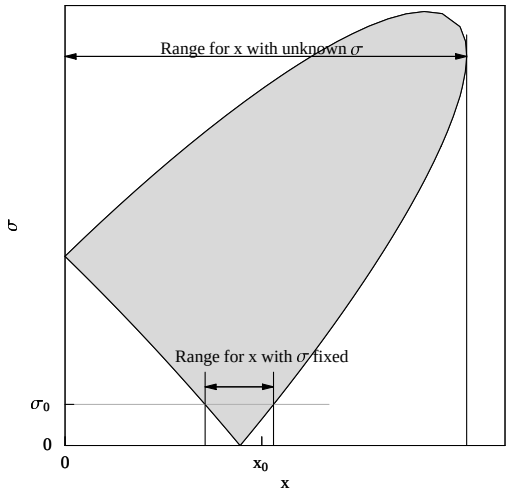

Figure 3.1: *The grey shaded area shows the set of points in the x-σ-plane which fulfills equation 3.8 for fixed n_0. In case σ is unknown the length of the upper arrow gives the allowed interval for x. If σ is known to be exactly σ_0 the range indicated by the lower arrow is the allowed range for x.*

was introduced in [92]. We introduce the following notation for the transformed quantities

$$\begin{aligned} \mathcal{T}_s\, c_i g_i &=: \hat{c}_i \hat{g}_i\,, \\ \mathcal{T}_t\, c_i g_i &=: \tilde{c}_i \tilde{g}_i\,, \\ \mathcal{T}_{ts}\, c_i g_i &=: \bar{c}_i \bar{g}_i\,. \end{aligned} \tag{3.10}$$

None of the $\mathcal{T}_i$ acts on x, σ, δ or n_0. In the case that the atmospheric mixing angle is exactly maximal, $\theta_{23} = \pi/4$, $\mathcal{T}_t$ becomes the identity transformation and $\mathcal{T}_{ts}$ reduces to $\mathcal{T}_s$. In general there are three additional sets of solutions which are connected by the three transformations. These additional sets are shown in figure 3.2. If there is only one observable there will be four sets of solutions for x in the most general case. Within each of these sets, δ can have any value, thus we obtain *no* information on the CP-phase. This is also true in the case that σ is kept fixed too. Besides there is no possibility to tell which of the four sets is the correct one, *i.e.* neither the mass hierarchy nor the quadrant of θ_{23} can be determined. As it will be shown in chapter 5 this result remains valid for all the experimental setups studied in this work which observe only one appearance channel. The energy information in those experiments is not sufficient to resolve the ambiguities. This can of course be altered by combining several experiments, which will be discussed in detail in the next section 3.4.

With only one observable it is not possible to measure δ

The classification of all the existing solutions is not straightforward and the complexity of this issue will appear even stronger in the context of sections 3.5 and 3.7. The term "degenerate" or "fake" solution has been brought forth in the literature to name all the solutions which do not coincide with the true values (*e.g.* in [92, 93]). This terminology is adequate in case there are really topologically disconnected solutions, which is usually the case for the three

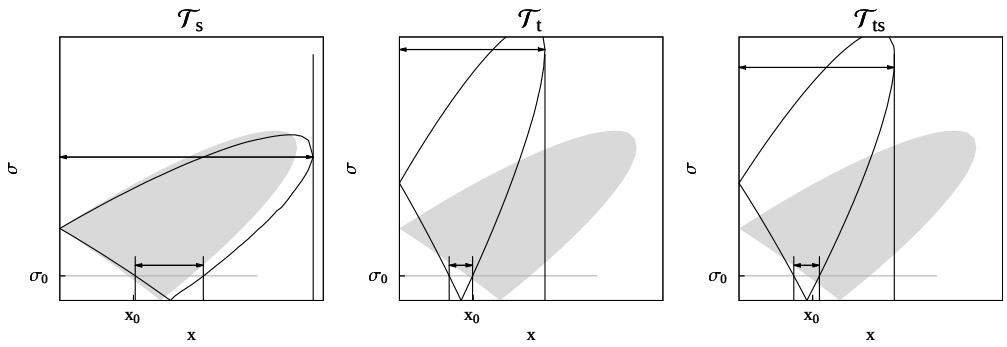

Figure 3.2: *The grey shaded area shows the set of points in x-σ-plane which fulfills equation 3.8 for fixed n_0 as in figure 3.1. The black solid lines delimit the set of points which give solutions to equation 3.8 once the transformations given atop of each panel are applied. In case σ is unknown the length of the upper arrow gives the allowed interval for x. If σ is known to be exactly σ_0 the range indicated by the lower arrow is the allowed range for x.*

additional sets of solutions generated by the discrete transformations $\mathcal{T}_s$, $\mathcal{T}_t$ and $\mathcal{T}_{ts}$. However the range of x values one obtains due to the unknown CP-phase within one set of solutions is as "fake" or "degenerate" as the three additional sets of solutions. They all are real solutions to equation 3.8. The difference is, however, that the CP-phase is a continuous variable, whereas $\mathcal{T}_s$, $\mathcal{T}_t$ and $\mathcal{T}_{ts}$ are discrete. Once the analysis gets more complex by including spectral information and detector effects the connectivity of the solutions is no longer a useful classification scheme since it depends sensitively on experiment specific parameters, like the detector threshold (see *e.g.* [80]). We will postpone this issue till section 3.7. However there still remains a problem with combining all the solutions into only one number like a sensitivity limit. One possible choice among others is to treat all possible solutions equally and to include all of them in the limit by defining the one-sided upper limit $\hat{\eta}$ to some quantity η by the maximum of *all* values for η which are compatible with the null result[3] at a given confidence level. This choice will be justified in detail in section 3.7 and is the basis for the definition of χ^2_{L} in equation B.4.

Since it is difficult to map out the surface described by equation 3.8 in the most general case, it is useful to look at some simpler special cases. It is of special interest whether the observation of n_0 allows us to put an *upper* limit on x. Especially the case when x_0 is zero, $x_0 = 0$, since this gives the sensitivity limit on $\sin^2 2\theta_{13}$. According to the above definition we have to take the largest value of all possible limits generated by applying $\mathcal{T}_s$, $\mathcal{T}_t$, $\mathcal{T}_{ts}$ and simultaneously leaving δ to vary freely. Inserting $x_0 = 0$ in equation 3.7 yields

$$n_0 = \sigma_0^2 c_3 g_3 \,, \tag{3.11}$$

thus n_0 is in this case independent of the CP-phase δ. Assuming σ to be exactly

[3]This is the result which would be obtained on average if $\eta_0 = 0$.

known, which is not realistic but serves as a starting point, σ becomes fixed to σ_0. Using this assumption and setting the left hand side of equation 3.8 to this value results in

$\sin^2 2\theta_{13}$ limit for fixed Δm^2_{21}

$$\begin{aligned} 0 &= x^2\, c_1 g_1 + x\sigma_0\, c_2 g_2(\delta) \;\Rightarrow \\ x_{1/2} &= \begin{cases} 0 \\ -\sigma_0 \frac{c_2 g_2(\delta)}{c_1 g_1} \end{cases} . \end{aligned} \tag{3.12}$$

Since there is no previous knowledge on δ, the next step is the determination of the value of δ which makes x_2 extremal. The location of the extrema is given by

$$\frac{\partial g_2(\delta)}{\partial \delta} = 0 \;\Rightarrow\; (\cos\delta\, g_{2a} - \sin\delta\, g_{2b}) = 0 \;\Rightarrow\; \tan\delta_{\text{extrem}} = \frac{g_{2a}}{g_{2b}} . \tag{3.13}$$

Using some trigonometrical relations we can compute the value of $g_2(\delta_{\text{extrem}})$

$$g_2^{\max} = \sqrt{g_{2a}^2 + g_{2b}^2}\,, \quad g_2^{\min} = -\sqrt{g_{2a}^2 + g_{2b}^2}\,. \tag{3.14}$$

Inserting the values for $g_2(\delta_{\text{extrem}})$ into equation 3.12 and keeping only the positive solution yields

$$x_{\text{up}} = \sigma_0 \frac{c_2 \sqrt{g_{2a}^2 + g_{2b}^2}}{c_1 g_1} . \tag{3.15}$$

The first observation is that increasing σ_0 increases the sensitivity limit x_{up}, *i.e.* the sensitivity of the experiment becomes worse for larger values of σ_0 even if the value of σ_0 is known with infinite precision. The second observation is that the sensitivity limit would be 0 if σ_0 became 0. This is of course not the case for any real experiment for two reasons: We have so far neglected the statistical nature of a real experiment. It is a counting experiment and therefore the observed number of events is subject to Poissonian fluctuations. The other reason is that even if the number of signal events, *i.e.* n_0, approaches zero there remain background events and their statistical fluctuations. Thus even if an experiment only observes the expected number of background events, one can *not* conclude that $x_0 \equiv 0$.

Inclusion of statistical fluctuations and backgrounds

In order to include the effects of limited statistics and background it is useful to first derive the upper bound on x as a function of n_0. The result of this is shown in the following equation

$$\begin{aligned} x_{\max} &= \frac{{c_2}^2 \sqrt{{g_{2a}}^2 + {g_{2b}}^2}\,\sigma + \sqrt{{c_2}^4\, ({g_{2a}}^2 + {g_{2b}}^2)\, \sigma^2 + 4\, c_1\, g_1\, (n_0 - c_3\, g_3\, \sigma^2)}}{2\, c_1\, g_1} \\ &\text{for all } \sigma \leq \frac{2\sqrt{c_1 g_1 n_0}}{\sqrt{-({c_2}^4\, ({g_{2a}}^2 + {g_{2b}}^2)) + 4\, c_1\, c_3\, g_1\, g_3}} . \end{aligned} \tag{3.16}$$

$x_{\max}$ is a monotonous increasing function of n_0, thus the largest value of n_0 called $n_0^{\max}$ which is allowed at a given confidence level yields the limit on x, which will be called $x_{\lim}$. The largest possible number of events at a certain confidence level is given by $n_0^{\max} := n_0 + \gamma\, \delta n_0$, where δn_0 is the one standard

deviation error on n_0 and γ is a trivial scaling factor for obtaining results at confidence levels different from one standard deviation. In order to compute δn_0 the additional error induced by the background subtraction has to be included. The total number of events which is observed in an experiment n_1 is the sum of signal events n_0 and background events n_{BG}, $n_1 = n_0 + n_{\mathrm{BG}}$. The computation of δn_1 directly yields δn_0. The error δn_1 on n_1 can be computed by Gaußian error propagation. We extend the definition of n_1 to include systematical uncertainties on the signal normalization a_{norm} and on the background expectation a_{BG}

$$\begin{aligned} n_1 &= (1 + a_{\mathrm{norm}})n_0 + (1 + a_{\mathrm{BG}})n_{\mathrm{BG}}\,, \\ (\delta n_1)^2 &= \underbrace{n_0 + n_{\mathrm{BG}}}_{\text{stat.}} + \\ &\quad \underbrace{\left(\left.\frac{\partial n_1}{\partial \sigma_0}\right|_{\sigma_0} \delta\sigma_0\right)^2 + \left(\left.\frac{\partial n_1}{\partial a_{\mathrm{norm}}}\right|_0 \delta a_{\mathrm{norm}}\right)^2 + \left(\left.\frac{\partial n_1}{\partial a_{\mathrm{BG}}}\right|_0 \delta a_{\mathrm{BG}}\right)^2}_{\text{syst.}}\,, \\ (\delta n_1)^2 &= n_{\mathrm{BG}} + c_3 g_3 \sigma_0^2 \\ &\quad + 4c_3^2 g_3^2 \sigma_0^2 \,(\delta\sigma_0)^2 + c_3^2 g_3^2 \sigma_0^4 \,(\delta a_{\mathrm{norm}})^2 + n_{\mathrm{BG}}^2 \,(\delta a_{\mathrm{BG}})^2\,. \end{aligned} \tag{3.17}$$

Since n_1 is the direct sum of n_0 and n_{BG} the error δn_0 on n_0 is equal to the error on n_1, $\delta n_1 = \delta n_0$. Putting everything together yields the following formula for determining the sensitivity limit x_{lim}

$$\begin{aligned} x_{\mathrm{lim}} &= \frac{1}{2\,c_1\,g_1}\Big({c_2}^2\,\sqrt{{g_{2a}}^2 + {g_{2b}}^2}\,\sigma_0 \\ &\quad + \sqrt{{c_2}^4\,({g_{2a}}^2 + {g_{2b}}^2)\,{\sigma_0}^2 + 4\,c_1\,g_1\,(n_0 + \gamma\delta n_0 - c_3\,g_3\,{\sigma_0}^2)}\Big)\,, \end{aligned} \tag{3.18}$$

where γ is 1 for 68.27% cl, 1.64 for 90% cl and 2 for 95.45% cl. The final limit as used throughout this work is given by the supremum of x_{lim}, $\hat{x}_{\mathrm{lim}}$, $\tilde{x}_{\mathrm{lim}}$ and $\bar{x}_{\mathrm{lim}}$, where $\hat{x}_{\mathrm{lim}}$, $\tilde{x}_{\mathrm{lim}}$ and $\bar{x}_{\mathrm{lim}}$ are obtained by applying equation 3.18 to the transformed coefficients $\hat{c}_i\hat{g}_i$, $\tilde{c}_i\tilde{g}_i$ and $\bar{c}_i\bar{g}_i$ as defined in equation 3.10. An equivalent definition for the numerical calculation is given in equation B.4.

The final result for the $\sin^2 2\theta_{13}$ limit

As shown in figure 3.3, equation 3.18 allows a rather precise calculation of the sensitivity limit for those experiments which measure only one number, *i.e.* they have only neutrino running and the number of events is not sufficiently large to deliver significant spectral information. The RMS error of equation 3.18 compared to the full numerical result is smaller than 4% for the whole range of Δm^2_{21} shown in the figure.

3.4 Two observables

In the previous section it was demonstrated that only one observable is insufficient to address the measurement of the CP-phase. Furthermore it is not

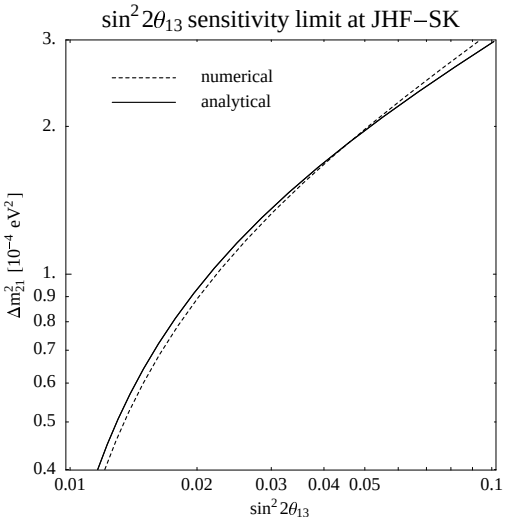

Figure 3.3: *The* $\sin^2 2\theta_{13}$ *limit at* 90% cl *for different values of* Δm^2_{21} *for the* JHF-SK *setup. The dashed line shows the result of a full numerical calculation (see appendix A, this line is also shown in the right hand panel of figure 6 in* [94]*), whereas the solid line shows the result obtained from equation 3.18.*

possible to either determine the mass hierarchy or the quadrant of θ_{23}. Obviously at least a second observable is needed to perform these measurements. In this section the benefits and limitations of having two observables will be discussed. The second observable can be provided in several ways: anti-neutrinos and/or the combination with another experiment. The mathematics, however, stays the same, instead of having only one equation like 3.8 there are now two equations, which have to be fulfilled simultaneously. The two equations are in analogy to the preceeding section

$$\text{(I)} \quad n_0^a = x^2\, c_1^a g_1^a + x\sigma\, c_2^a g_2^a + \sigma^2 c_3^a g_3^a\,, \tag{3.19}$$

$$\text{(II)} \quad n_0^b = x^2\, c_1^b g_1^b + x\sigma\, c_2^b g_2^b + \sigma^2 c_3^b g_3^b\,. \tag{3.20}$$

Solving the equations

By a suitable subtraction of I and II, one of the quadratic terms can be eliminated. This yields two equations, each linear in either x or σ

$$\text{I} - \frac{c_1^a g_1^a}{c_1^b g_1^b}\text{II} \quad \Rightarrow \tag{3.21}$$

$$n_0^a - \frac{c_1^a g_1^a}{c_1^b g_1^b} n_0^b = x\sigma \left(c_2^a g_2^a - \frac{c_1^a g_1^a}{c_1^b g_1^b} c_2^b g_2^b \right) + \sigma^2 \left(c_3^a g_3^a - \frac{c_1^a g_1^a}{c_1^b g_1^b} c_3^b g_3^b \right),$$

$$\text{I} - \frac{c_3^a g_3^a}{c_3^b g_3^b}\text{II} \quad \Rightarrow \tag{3.22}$$

$$n_0^a - \frac{c_3^a g_3^a}{c_3^b g_3^b} n_0^b = x\sigma \left(c_2^a g_2^a - \frac{c_3^a g_3^a}{c_3^b g_3^b} c_2^b g_2^b \right) + x^2 \left(c_1^a g_1^a - \frac{c_3^a g_3^a}{c_3^b g_3^b} c_1^b g_1^b \right).$$

In order to keep the notation concise, the following definitions are made

$$\begin{aligned} N_x &:= n_0^a - \frac{c_1^a g_1^a}{c_1^b g_1^b} n_0^b\,, \qquad & N_\sigma &:= n_0^a - \frac{c_3^a g_3^a}{c_3^b g_3^b} n_0^b\,, \\ M_x &:= c_2^a g_2^a - \frac{c_1^a g_1^a}{c_1^b g_1^b} c_2^b g_2^b\,, \qquad & M_\sigma &:= c_2^a g_2^a - \frac{c_3^a g_3^a}{c_3^b g_3^b} c_2^b g_2^b\,, \\ Q_x &:= c_3^a g_3^a - \frac{c_1^a g_1^a}{c_1^b g_1^b} c_3^b g_3^b\,, \qquad & Q_\sigma &:= c_1^a g_1^a - \frac{c_3^a g_3^a}{c_3^b g_3^b} c_1^b g_1^b\,. \end{aligned}$$

Using these and the above two equations, solutions for x and σ can be found

$$x = \frac{N_x - Q_x\,\sigma^2}{M_x\,\sigma} \tag{3.23}$$

$$\sigma = \frac{N_\sigma - Q_\sigma\,x^2}{M_\sigma\,x} \tag{3.24}$$

Inserting 3.23 in 3.24 and solving for σ yields

$$\begin{aligned} \sigma^2(\delta) = {} & \frac{1}{2\,Q_x\,\left(M_x\,M_\sigma - Q_x\,Q_\sigma\right)} \\ & \Big[M_x\,M_\sigma\,N_x - {M_x}^2\,N_\sigma - 2\,N_x\,Q_x\,Q_\sigma \\ & \pm M_x \sqrt{{M_\sigma}^2\,{N_x}^2 - 2\,M_x\,M_\sigma\,N_x\,N_\sigma + {M_x}^2\,{N_\sigma}^2 + 4\,N_x\,N_\sigma\,Q_x\,Q_\sigma} \Big]\,. \end{aligned} \tag{3.25}$$

Inserting 3.24 in 3.23 and this time solving for x yields

$$\begin{aligned} x^2(\delta) = {} & \frac{1}{2\,Q_\sigma\,\left(M_x\,M_\sigma - Q_x\,Q_\sigma\right)} \\ & \Big[-\left({M_\sigma}^2\,N_x\right) + M_x\,M_\sigma\,N_\sigma - 2\,N_\sigma\,Q_x\,Q_\sigma \\ & \pm M_\sigma \sqrt{{M_\sigma}^2\,{N_x}^2 - 2\,M_x\,M_\sigma\,N_x\,N_\sigma + {M_x}^2\,{N_\sigma}^2 + 4\,N_x\,N_\sigma\,Q_x\,Q_\sigma} \Big]\,. \end{aligned} \tag{3.26}$$

This result is quite complicated, since M_x and M_σ are functions of $\sin\delta$ and $\cos\delta$, thus x^2 and σ^2 depend on the CP-phase δ in a non-trivial way. Furthermore determining which sign in each of the solutions is the correct one is rather tricky. One can, however, prove the following useful theorem:

Theorem *Equations 3.26 and 3.25 constitute a parametric representation of an ellipse in the coordinates x^2 and σ^2, where the parameter is δ.*

Ellipses are the solution and vice versa

The proof consists in finding a representation of the space curve described by equations 3.26 and 3.25 in the form of a general ellipse, with $u := x^2$ and $v := \sigma^2$

$$a_{11}\,u^2 + a_{12}\,u\,v + a_{22}\,v^2 + a_{13}\,u + a_{23}\,v + a_{33} = 0\,. \tag{3.27}$$

To this end the algebra of equations 3.21 – 3.24 is repeated but now in order to isolate $\sin\delta$ and $\cos\delta$ instead of x and σ. With a set of new definitions,

$$\begin{aligned}
N_{\sin\delta} &:= n_0^a - \frac{c_2^a g_{2b}^a}{c_2^b g_{2b}^b} n_0^b\,, \qquad & N_{\cos\delta} &:= n_0^a - \frac{c_2^a g_{2a}^a}{c_2^b g_{2a}^b} n_0^b\,,\\
M_{\sin\delta} &:= c_2^a - \frac{c_2^a g_{2b}^a}{c_2^b g_{2b}^b} c_2^b g_{2a}^b\,, \qquad & M_{\cos\delta} &:= c_2^a g_2^a - \frac{c_2^a g_{2a}^a}{c_2^b g_{2a}^b} c_2^b g_{2b}^b\,,\\
Q_{\sin\delta} &:= c_3^a g_3^a - \frac{c_2^a g_{2b}^a}{c_2^b g_{2b}^b} c_3^b g_3^b\,, \qquad & Q_{\cos\delta} &:= c_3^a g_3^a - \frac{c_2^a g_{2a}^a}{c_2^b g_{2a}^b} c_3^b g_3^b\,,\\
K_{\sin\delta} &:= c_1^a g_1^a - \frac{c_2^a g_{2b}^a}{c_2^b g_{2b}^b} c_1^b g_1^b\,, \qquad & K_{\cos\delta} &:= c_1^a g_1^a - \frac{c_2^a g_{2a}^a}{c_2^b g_{2a}^b} c_1^b g_1^b\,,
\end{aligned} \tag{3.28}$$

the results for $\sin\delta$ and $\cos\delta$ as functions of x and σ are

$$\sin\delta = \frac{N_{\cos\delta} - x^2\, K_{\cos\delta} - \sigma^2\, Q_{\cos\delta}}{x\,\sigma\, M_{\cos\delta}} \tag{3.29}$$

$$\cos\delta = \frac{N_{\sin\delta} - x^2\, K_{\sin\delta} - \sigma^2\, Q_{\sin\delta}}{x\,\sigma\, M_{\sin\delta}} \tag{3.30}$$

Using the well-known relation $\sin^2\theta + \cos^2\theta = 1$ and equations 3.29 and 3.30 the following equation is found

$$\begin{aligned}
\left(N_{\cos\delta} - x^2\, K_{\cos\delta} - \sigma^2\, Q_{\cos\delta}\right)^2 + \left(N_{\sin\delta} - x^2\, K_{\sin\delta} - \sigma^2\, Q_{\sin\delta}\right)^2 = \\
x^2\,\sigma^2\, {M_{\sin\delta}}^2\, {M_{\cos\delta}}^2\,,
\end{aligned} \tag{3.31}$$

which only depends on $x^2 = u$ and $\sigma^2 = v$. Therefore replacing x^2 by u and σ^2 by v, expanding the terms and collecting the coefficients we obtain the same form as given in equation 3.27

$$a_{11}\,u^2 + a_{12}\,u\,v + a_{22}\,v^2 + a_{13}\,u + a_{23}\,v + a_{33} = 0\,, \tag{3.32}$$

where the coefficients a_{ij} are given by

$$\begin{aligned}
a_{11} &= {K_{\sin\delta}}^2\, {M_{\cos\delta}}^2 + {K_{\cos\delta}}^2\, {M_{\sin\delta}}^2\,,\\
a_{22} &= {M_{\sin\delta}}^2\, {Q_{\cos\delta}}^2 + {M_{\cos\delta}}^2\, {Q_{\sin\delta}}^2\,,\\
a_{12} &= -M_{\cos\delta}\, M_{\sin\delta} + 2\, K_{\cos\delta}\, {M_{\sin\delta}}^2\, Q_{\cos\delta} + 2\, K_{\sin\delta}\, {M_{\cos\delta}}^2\, Q_{\sin\delta}\,,\\
a_{13} &= -2\, K_{\cos\delta}\, {M_{\sin\delta}}^2\, N_{\cos\delta} - 2\, K_{\sin\delta}\, {M_{\cos\delta}}^2\, N_{\sin\delta}\,,\\
a_{23} &= -2\, {M_{\sin\delta}}^2\, N_{\cos\delta}\, Q_{\cos\delta} - 2\, {M_{\cos\delta}}^2\, N_{\sin\delta}\, Q_{\sin\delta}\,,\\
a_{33} &= {M_{\sin\delta}}^2\, {N_{\cos\delta}}^2 + {M_{\cos\delta}}^2\, {N_{\sin\delta}}^2\,.
\end{aligned} \tag{3.33}$$

This completes the proof of the theorem given above.

3.5 Eight-fold degeneracy

Equations 3.32 and 3.33 allow now to derive the location of each of the eight solutions in a closed form. The occurrence of eight solutions was shown in [92], where the discussion is based on two assumptions – σ is known exactly and

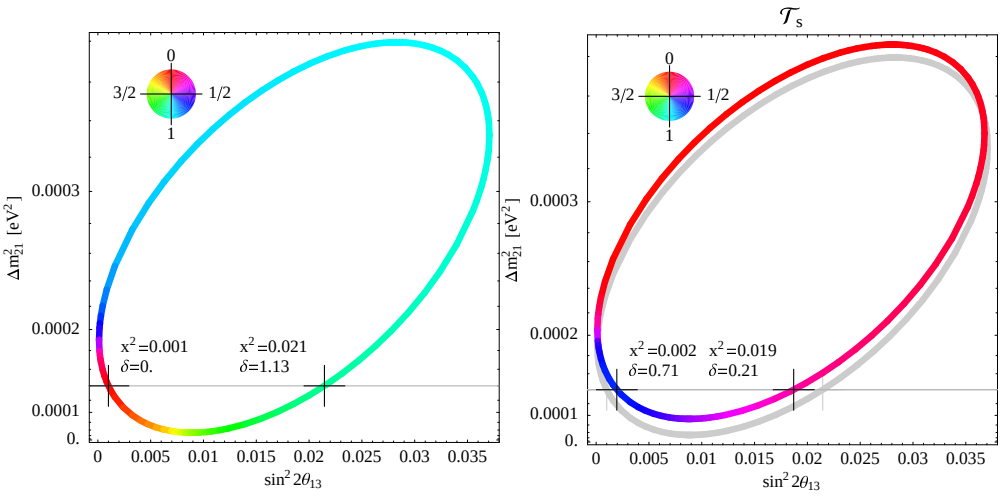

Figure 3.4: *The ellipses defined by equation 3.32 for* NuFact-II*. The colors encode the* CP*-phase δ as indicated by the colored disk in the upper left corner of each panel. The grey horizontal line shows the value of $\sigma_0 = 1.4 \cdot 10^{-4}\,\mathrm{eV}^2$. The left hand panel shows the intrinsic set of solutions. The right hand panel shows the set of solutions obtained by applying $\mathcal{T}_s$, the so called sign of Δm^2_{31} degeneracy. In the left hand panel, the left black cross indicates the location of the true parameters, whereas the right cross shows the location of the intrinsic ambiguity. The black crosses in the right hand panel show the two additional solutions for opposite mass hierarchy. The grey ellipse in the right hand panel is formed by the solutions for the intrinsic case, i.e. the same as in the left hand panel. The values of δ are given in units of π.*

the neutrino beam is mono-energetic. Fixing the value of σ implies that only a subset of the complete set of possible solutions is studied, *i.e.* the ellipses of equation 3.32 are reduced to a set of discrete points. First the so called intrinsic ambiguity is discussed. It was discovered in [93] and a closed form solution for its location was given in [92]. It occurs at the same value of σ as the true value σ_0. Solving equation 3.32 for $u = x^2$ yields:

$$x^2_{1/2} = \frac{-2\,v\,a_{12} - a_{13} \pm \sqrt{(2\,v\,a_{12} + a_{13})^2 - 4\,a_{11}\;(v^2\,a_{22} + v\,a_{23} + a_{33})}}{2\,a_{11}}\,. \tag{3.34}$$

At $v = \sigma_0^2$ one of the solutions for x^2 in equation 3.34 coincides with x_0^2. Whereas the other solution is the so called intrinsic ambiguity. The CP-phase δ of the intrinsic ambiguity can now easily be calculated by using equations 3.29 and 3.30. This shows that in general there are two solutions, even for fixed σ. In the left hand panel of figure 3.4 a graphical representation of this fact is given. The two solutions $x_{1/2}$ are the intersections of the grey line ($\sigma = \sigma_0$) and the ellipse (defined by equation 3.32). This example is computed for NuFact-II with $x_0^2 = 10^{-3}$, $\sigma_0 = 1.4 \cdot 10^{-4}\,\mathrm{eV}^2$, $\delta_0 = 0$, $(\Delta m^2_{31})_0 = +3 \cdot 10^{-3}\,\mathrm{eV}^2$ and $(\theta_{23})_0 = 0.55$. Here the intrinsic ambiguity appears at $x_2^2 = 0.021$ and $\delta_2 = 1.13\,\pi$.

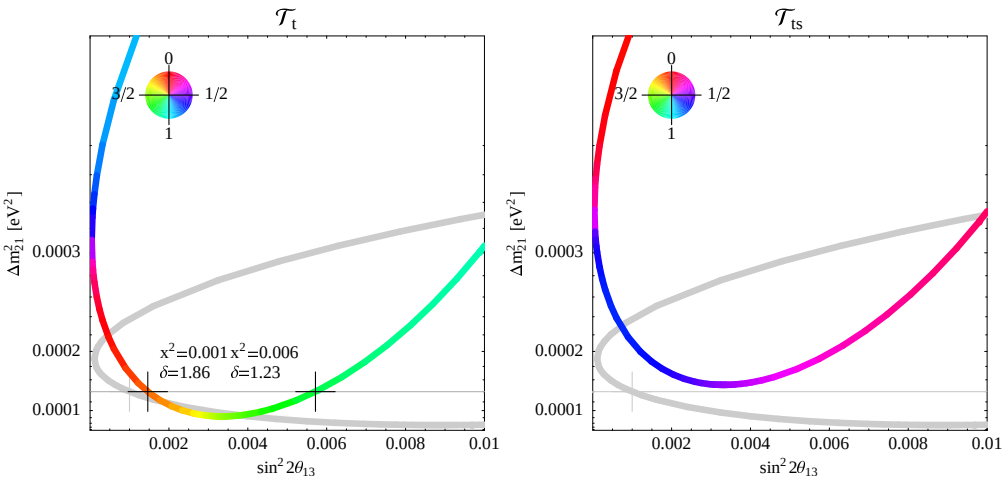

Figure 3.5: *The ellipses defined by equation 3.32 for* NuFact-II*. The colors encode the* CP*-phase δ as indicated by the colored disk in the upper left corner of each panel. The grey horizontal line shows the value of $\sigma_0 = 1.4 \cdot 10^{-4}\,\mathrm{eV}^2$. The left hand panel shows the set of solutions obtained by applying $\mathcal{T}_t$. The right hand panel shows the set of solutions obtained by applying $\mathcal{T}_{ts}$. The black crosses show the two additional solutions for either $\theta_{23} > \pi/4$ or for opposite mass hierarchy and $\theta_{23} > \pi/4$. The grey ellipses are the solutions given by the intrinsic case, i.e. the same as in the left hand panel of figure 3.4. The value of δ is given in units of π.*

Application of the discrete transformations

Next we derive the other solutions generated by the discrete transformations $\mathcal{T}_s$, $\mathcal{T}_t$ and $\mathcal{T}_{ts}$. The transformed versions of equation 3.34 are obtained by applying the $\mathcal{T}_i$ to each of the coefficients in equation 3.28.

$$\hat{x}^2_{1/2} = \frac{-2\,v\,\hat{a}_{12} - \hat{a}_{13} \pm \sqrt{(2\,v\,\hat{a}_{12} + \hat{a}_{13})^2 - 4\,\hat{a}_{11}\,(v^2\,\hat{a}_{22} + v\,\hat{a}_{23} + \hat{a}_{33})}}{2\,\hat{a}_{11}}\,, \tag{3.35}$$

$$\tilde{x}^2_{1/2} = \frac{-2\,v\,\tilde{a}_{12} - \tilde{a}_{13} \pm \sqrt{(2\,v\,\tilde{a}_{12} + \tilde{a}_{13})^2 - 4\,\tilde{a}_{11}\,(v^2\,\tilde{a}_{22} + v\,\tilde{a}_{23} + \tilde{a}_{33})}}{2\,\tilde{a}_{11}}\,, \tag{3.36}$$

$$\bar{x}^2_{1/2} = \frac{-2\,v\,\bar{a}_{12} - \bar{a}_{13} \pm \sqrt{(2\,v\,\bar{a}_{12} + \bar{a}_{13})^2 - 4\,\bar{a}_{11}\,(v^2\,\bar{a}_{22} + v\,\bar{a}_{23} + \bar{a}_{33})}}{2\,\bar{a}_{11}}\,. \tag{3.37}$$

Thus there are alltogether eight possible values for x^2, namely $x^2_{1/2}$, $\hat{x}^2_{1/2}$, $\tilde{x}^2_{1/2}$ and $\bar{x}^2_{1/2}$. These values can now be used with equations 3.29 and 3.30 to compute $\delta_{1/2}$, $\hat{\delta}_{1/2}$, $\tilde{\delta}_{1/2}$ and $\bar{\delta}_{1/2}$. In doing so also the coefficients in equations 3.29 and 3.30 have to be transformed according to the definition of the $\mathcal{T}_i$.

These eight sets of δ and x^2 constitute the "eight-fold" degeneracy as discussed in [92]. An approximate result for equations 3.35 and 3.36 was presented in [92]. The solution for $\bar{x}$ is presented here for the first time. Obviously not all of the equations 3.35 – 3.37 yield real and positive solutions for x^2 in all cases, thus in certain circumstances only a subset of those eight solutions appears in an experiment.

In figures 3.4 and 3.5 an example of the four possible ellipses is shown. They have been calculated for the NuFact-II setup with $\sigma_0 = 1.4 \cdot 10^{-4}\,\mathrm{eV}^2$, $\Delta m^2_{31} = +3 \cdot 10^{-3}\,\mathrm{eV}^2$, $\theta_{23} = 0.55$, $x^2_0 = 10^{-3}$ and $\delta_0 = 0$. The left hand panel of figure 3.4 shows the intrinsic case. The right hand panel is drawn for $\Delta m^2_{31} = -3 \cdot 10^{-3}\,\mathrm{eV}^2$. There are two solutions for $\hat{x}^2$ with the values indicated in the figure. Again for the case of $\theta_{23} = \pi/2 - 0.55$ there are two solutions as shown in the left hand panel of figure 3.5. For the ellipse which has been obtained by applying both $\mathcal{T}_s$ and $\mathcal{T}_t$ there are no solutions for $\sigma = \sigma_0$ as it can be seen in the right hand panel of figure 3.5. But already for a value of $\sigma = 1.52 \cdot 10^{-4}\,\mathrm{eV}^2$ a solution appears, *i.e.* if a $\sim 9\%$ larger value of σ than σ_0 was allowed, at least one solution with both $\Delta m^2_{31} = -3 \cdot 10^{-3}\,\mathrm{eV}^2$ and $\theta_{23} = \pi/2 - 0.55$ would exist. This illustrates the importance of taking into account the finite error on σ. In the example shown here, no determination of the mass hierarchy or the quadrant of θ_{23} would be possible. Also the test of CP-conservation would fail since there are additional solutions close to maximal CP-violation.

3.6 More degeneracies

In section 3.5 the solar mass splitting σ was regarded as fixed, which led to the eight-fold degeneracy. Relaxing this assumption and treating σ as a free parameter yielded the ellipses as defined in equation 3.32 and shown in figures 3.4 and 3.5. In this case, obviously the intrinsic ambiguity does no longer exist as *disconnected* solution, it is just one solution amongst many[4] others. Thus in terms of total event rates a picture emerges where there are four sets of solutions generated by the discrete transformations $\mathcal{T}_s$, $\mathcal{T}_t$, and $\mathcal{T}_{ts}$. Each of these sets is an ellipse in the x^2-σ^2-plane.

The discussion up to now has focused on total rates only, leaving a set of four ellipses. The question now is, how many of these points survive in a full analysis. For this purpose a simplified scheme for the analysis will be used: only θ_{13}, σ and δ will be considered and only the appearance channels are used. This ensures a concise presentation and still retains the essential features of the full analysis technique as described in appendix B. The following example has been calculated for NuFact-II and the set of true parameters $\boldsymbol{\lambda}_0$: $(\sin^2 2\theta_{13})_0 = 10^{-3}$, $\delta_0 = 0$ and $\sigma_0 = 1.4 \cdot 10^{-4}\,\mathrm{eV}^2$. The aim is to extract this set $\boldsymbol{\lambda}_0$. $(\theta_{23})_0$ was chosen to be 0.55 instead of the current best fit value of $\pi/4$ in order to make it possible to study the θ_{23} ambiguity $\mathcal{T}_t$ as well. This example will also be used to illustrate the basic features of the analysis technique used for obtaining the results of chapter 5. The results of the previous section serve as a very useful

A showcase

[4] in fact, uncountably many

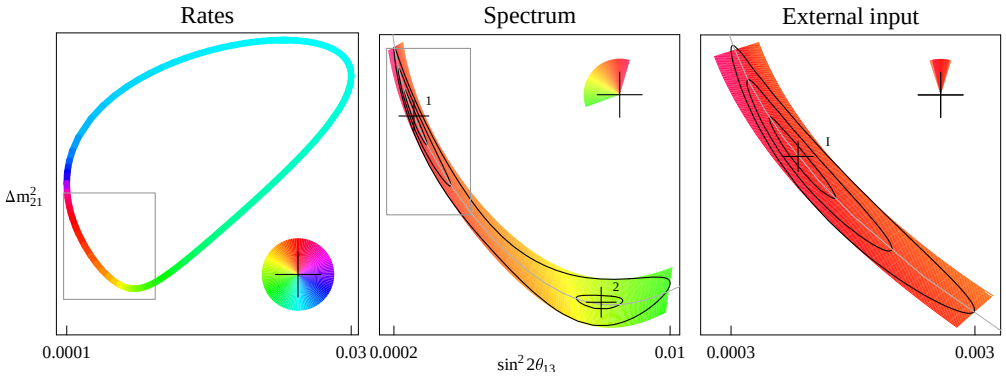

Figure 3.6: *The left hand panel shows the ellipse of all solutions in the x^2-σ-plane of equation 3.32 for the intrinsic case. The color coding indicates the* CP*-phase as shown in the colored circle in the lower right corner of this panel. Here twelve o'clock marks $\delta = 0$, six o'clock $\delta = \pi$, a.s.f.. The labels at the frame indicate the allowed range for $x^2 = \sin^2 2\theta_{13}$. The grey thin curve in the middle and rightmost panel indicates the location of the solutions of equation 3.32. The grey rectangle shows the region displayed in the middle panel. In the middle panel the effect of the inclusion of spectral information is shown. The black lines are the 1, 2 and 3 standard deviations contours (1* DOF*) of a fit which leaves δ free. The colored pie slice shows the range of* CP*-phases which is still allowed at 99.73%* cl*. The color coding underneath the contours depicts the values of δ at which the minimum χ^2 occured. The grey box now is the area shown in the right hand panel. Here the effect of the inclusion of external input on σ is shown. To this end a 15% uncertainty on σ is assumed. This example has been calculated for* NuFact-II*.*

tool – their value lies in their ability to predict the approximate location of the local minima of the χ^2-function. This is a crucial ingredient for the numerical calculation, since there is no general algorithm for finding the global minimum of the χ^2-function. But since the location of all local minima is approximately known, the exact location and χ^2-value of each local minimum can be found, as discussed in detail in appendix B.

Total rates

The starting point for this showcase analysis, as for the real analysis, are the solutions for the total rates as shown in the leftmost panel of figure 3.6 for the intrinsic case. The abscissa is x^2 and the ordinate σ. The color indicates the CP-phase, whereas the colored disk shows the allowed range for δ, which is 2π in this case. The labels at the abscissa yield the allowed range for $x^2 = 1{\cdot}10^{-4}{-}3{\cdot}10^{-2}$.

Spectrum

The next step is to include spectral information. A χ^2-fit to the observed (*i.e.* with $\boldsymbol{\lambda}_0$ simulated) data is performed with δ as a free parameter. The resulting χ^2-function is projected onto the displayed x^2-σ-plane. This means that for each pair of x^2 and σ the minimum of the χ^2 as function of δ is determined. Contours of this projected χ^2-function are shown in the middle panel as black lines, representing the 1, 2 and 3 standard deviations confidence levels for 1 DOF.[5]

[5] One degree of freedom was chosen in order to facilitate the visual projection onto the axes to obtain the allowed ranges.

The coloring indicates the values of δ for which the minimum was found. The range in x^2 and σ is strongly reduced by the inclusion of spectral information. This reduction is illustrated by the grey box in the left hand panel – it is the area covered by the middle panel.

	$\Delta\chi^2$	position			x^2-range		δ-range	
		x^2	σ	δ				
1	0.0	$1.0 \cdot 10^{-3}$	1.4	0.0	$2.0 \cdot 10^{-4}$	$1.1 \cdot 10^{-2}$	-0.61	0.09
2	3.5	$8.4 \cdot 10^{-3}$	0.53	-0.42				
3	3.4	$9.7 \cdot 10^{-4}$	1.6	0.74	$2.7 \cdot 10^{-4}$	$3.0 \cdot 10^{-3}$	0.67	0.77
4	1.1	$1.0 \cdot 10^{-4}$	0.97	0.41	$5.5 \cdot 10^{-3}$	$1.3 \cdot 10^{-2}$	0.32	0.60
5	0.1	$3.3 \cdot 10^{-4}$	2.3	0.0	$7.6 \cdot 10^{-5}$	$4.1 \cdot 10^{-3}$	-0.62	0.09
6	3.6	$3.2 \cdot 10^{-3}$	0.90	1.15				
7	3.5	$3.9 \cdot 10^{-4}$	2.6	0.74	$1.0 \cdot 10^{-4}$	$1.3 \cdot 10^{-3}$	0.31	0.64
8	1.0	$3.8 \cdot 10^{-3}$	1.5	0.42	$1.9 \cdot 10^{-3}$	$5.1 \cdot 10^{-3}$	0.67	0.78

Table 3.1: *The $\Delta\chi^2$ and positions of the local minima for unconstrained σ. Also given are the three standard deviations allowed ranges for x^2 and δ. In the cases, where one range for two lines is shown, the two minima are connected by the three standard deviations allowed region. Minima 1 and 2 are marked by black crosses in the middle panel of figure 3.6. The units are $10^{-4}\,\mathrm{eV}^2$ for σ and δ is given in units of π.*

The range for x^2 is now $x^2 = 2.0 \cdot 10^{-4} - 1.1 \cdot 10^{-2}$. The χ^2 has two local minima, labeled 1 and 2. They have rather different values for the CP-phase: minimum 1 has $\delta = 0$, whereas number 2 has $\delta = -0.42\,\pi$. The $\Delta\chi^2$ of minimum 2 is 3.5. The remaining range for the CP-phase is $\delta = -0.07\,\pi - 0.67\,\pi$. Thus there are still two solutions for the CP-phase, one is CP-conserving, whereas the other solution is nearly maximally CP-violating. A summary of the properties and ranges for each possible minimum at the level of a spectral analysis is given in table 3.1. Interestingly, in this example the two solutions do not appear at the same value of the solar mass splitting σ, thus none of the two represents the intrinsic ambiguity as defined in [93].

Constraint on Δm^2_{21}

As a third step the external information on the value of σ is used and results in the rightmost panel of figure 3.6. A 1 standard deviation error on σ of 15% is assumed around the central value $\sigma_0 = 1.4 \cdot 10^{-4}\,\mathrm{eV}^2$. Here only one solution survives, labeled I, at the location of the true parameters, *i.e.* $\sin^2 2\theta_{13} = 10^{-3}$, $\delta = 0$ and $\sigma = 1.4 \cdot 10^{-4}\,\mathrm{eV}^2$. The range for x^2 is further reduced to $x^2 = 3{\cdot}10^{-4} - 3{\cdot}10^{-3}$, also the allowed CP-phases are more restricted, $\delta = -0.06\,\pi - 0.1\,\pi$, clearly excluding large or maximal CP-violation. Table 3.2 summarizes the location and associated ranges for each of the possible minima in the final result. The solutions to equation 3.32 are very well suited to predict the location of each of the three minima 1,2 and I. This can be seen again in figure 3.6 – the thin grey curve in the middle and right panel is formed by the solutions to equation 3.32. All minima (black crosses) lie near or even exactly on this curve, thus a simple line search along this curve allows to determine an approximate location for each of the minima. This line search basically consists

Finding all local minima of $\Delta\chi^2$

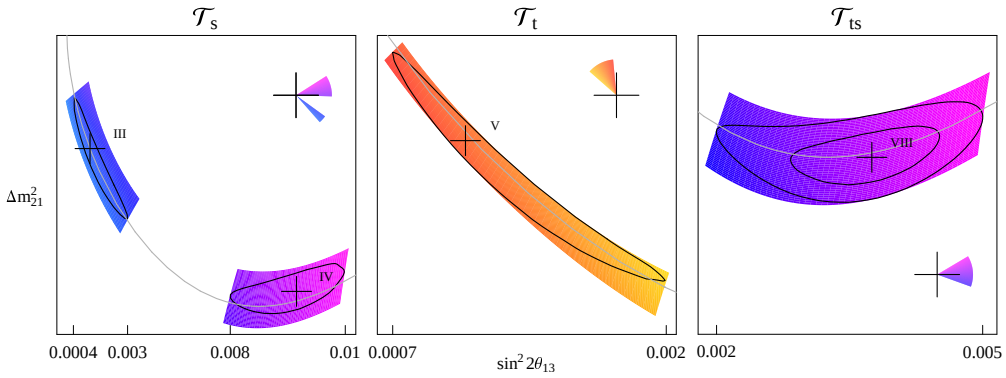

Figure 3.7: *The same as the rightmost panel of figure 3.6, but now for the three other sets of solutions generated by $\mathcal{T}_s$, $\mathcal{T}_t$ and $\mathcal{T}_{ts}$.*

in calculating the full χ^2 along the curve of solutions defined by equation 3.32 and then in identifying all local minima. The advantage is that the dimension of the search space has been reduced from 3 to 1 – this makes the problem of finding all local minima of the χ^2-function, which would have been nearly intractable in three dimensions, a comparatively easy task.

	$\Delta\chi^2$	position			x^2-range		δ-range	
		x^2	σ	δ				
I	0.0	$1.0 \cdot 10^{-3}$	1.4	0.0	$2.6 \cdot 10^{-4}$	$3.0 \cdot 10^{-3}$	-0.1	0.08
III	4.1	$1.2 \cdot 10^{-3}$	1.6	0.74	$4.2 \cdot 10^{-4}$	$2.9 \cdot 10^{-3}$	0.70	0.77
IV	5.2	$1.1 \cdot 10^{-2}$	1.0	0.40	$7.5 \cdot 10^{-3}$	$1.3 \cdot 10^{-2}$	0.32	0.51
V	6.9	$1.1 \cdot 10^{-3}$	1.6	-0.09	$6.7 \cdot 10^{-4}$	$2.3 \cdot 10^{-3}$	-0.27	-0.03
VIII	1.3	$3.8 \cdot 10^{-3}$	1.5	0.42	$2.2 \cdot 10^{-3}$	$5.0 \cdot 10^{-3}$	0.33	0.61

Table 3.2: *The $\Delta\chi^2$ and positions of the local minima for σ constrained to $\pm 0.15\,\sigma_0$ at 68.27% cl. Also given are the three standard deviations allowed ranges for x^2 and δ. Minimum* I *is marked by a black cross in the rightmost panel of figure 3.6, whereas minima* III *and* IV *are shown in the leftmost panel of figure 3.7. Minimum* V *is shown in the middle panel of this figure and finally minimum* VIII *is given in the rightmost panel. The units are $10^{-4}\,\mathrm{eV}^2$ for σ and δ is given in units of π.*

The exercise done for the intrinsic ellipse has now to be repeated for the three other ellipses, *i.e.* for the cases $\Delta m^2_{31} \to -\Delta m^2_{31}$, $\theta_{23} \to \pi/2 - \theta_{23}$ and $\Delta m^2_{31} \to -\Delta m^2_{31} \oplus \theta_{23} \to \pi/2 - \theta_{23}$. Again, first the solutions in terms of total rates according to equation 3.32 are computed. Then the spectral information is added and the local minima are found. All minima on this level of the analysis are listed in table 3.1. Number 1 and 2 are the intrinsic case, whereas number 3 and 4 are for $\mathcal{T}_s$, number 5 and 6 are for $\mathcal{T}_t$ and the last two 7 and 8 are for $\mathcal{T}_{ts}$. Thus there are two minima in each set of solutions. In this example there are indeed eight local minima, which however is *not* the eight-fold degeneracy as defined in [92], since only three minima (number 1, 3 and 8) appear at

approximately σ_0, and no pair of them belongs to one set, which would be expected if they indeed belonged to the intrinsic ambiguity as found in [93]. Thus the absence of a second solution at $\sigma = \sigma_0$ does in general not imply that no second solution exists. For two sets, namely the intrinsic one and $\mathcal{T}_t$ the two minima are connected into one solution (at 99.73% cl). Furthermore there is a great variety in the value of the CP-phase in each minimum and also the ranges for δ given in table 3.1 cover a fraction of $\sim 57\%$ of the unit circle. Even more problematic, they completely blur the distinction of CP-violation and CP-conservation. Thus the presence of several solutions is a veritable obstacle in the quest for leptonic CP-violation.

The third step of the analysis is once more to include an external constraint on the solar mass splitting σ. The final result for all three cases is shown in figure 3.7. Each panel in this figure corresponds to the rightmost panel in figure 3.6. The thin grey curves show again the location of the solutions of equation 3.32 in each case. Also here the local minima (black crosses) are very close to these lines which demonstrates that the analysis method described here works for those cases as well. The respective locations of the minima, the allowed ranges *etc.* are given in table 3.2. The number of remaining solutions is reduced to five. Only for the case $\mathcal{T}_s$ there are two solutions left. The $\mathcal{T}_s$ transformation maps the CP-conserving true phase $\delta_0 = 0$ into two other, clearly CP-violating phases (solutions III and IV). This phenomenon has already been observed and discussed in detail in [80]. On the other hand the $\mathcal{T}_t$ transformation (solution V) does not affect the value or range of the CP-phase very much, as described in *e.g.* [80,92]. In the combined case $\mathcal{T}_{ts}$ (solution VIII), however, the influence of $\mathcal{T}_s$ is very strong and the shift in the CP-phase is rather pronounced. Thus even in the full analysis several solutions are present, and some of them do strongly mix CP-violation and CP-conservation. Also the determination of θ_{13} strongly suffers from the presence of several solutions. Especially solution IV, belonging to the $\mathcal{T}_s$ set, extends the allowed range upwards by some factor of 30 compared to $(\sin^2 2\theta_{13})_0$. It is therefore a necessity to take the existence of multiple solutions into account in assessing the physics potential of future experiments.

CP-conservation and CP-violation are mixed by the multiplicity of solutions

	$\Delta\chi^2$	x^2-range		δ-range	
1	0.0	$7.6 \cdot 10^{-4}$	$1.3 \cdot 10^{-3}$	-0.07	0.05
3	5.9	$1.7 \cdot 10^{-3}$	$2.4 \cdot 10^{-2}$	0.70	0.76
5 6	7.3	$1.3 \cdot 10^{-3}$	$1.6 \cdot 10^{-3}$	-0.16	-0.10
8	4.7	$2.8 \cdot 10^{-3}$	$4.1 \cdot 10^{-3}$	0.40	0.54

Table 3.3: *The $\Delta\chi^2$ of the local minima for σ fixed to σ_0. Also given are the three standard deviations allowed ranges for x^2 and δ, where δ is given in units of π.*

Since most of the published results have been derived with keeping σ fixed[6], *i.e.* neglecting the errors on the solar parameters, also the results for fixed

[6]The exceptions are [80, 81, 94–96].

σ are shown in table 3.3. Obviously the ranges for both δ and $\sin^2 2\theta_{13}$ are significantly reduced within each solution. Furthermore one solution around $\delta \simeq 0.5\,\pi$ disappears. Thus the fraction of the unit circle covered by δ decreases from 57% by a factor of 2.7 to 21% and no CP-violating solution remains at the 95.45% cl. In fact, at this confidence level, only one solution would remain and the fraction of the unit circle covered by δ would reduce to less than 6%. This one example already illustrates the importance of taking into account the limited accuracy in the knowledge of the solar parameters. Keeping in mind that the solar parameters enter the oscillation probability in equation 3.1 via the product $\Delta m^2_{21} \cdot \sin 2\theta_{12}$, the errors on the angle and the mass splitting give an equal contribution to the total uncertainty. Kamland will determine Δm^2_{21} with high precision, but its performance on $\sin 2\theta_{12}$ will be rather poor [5,97]. Thus the error on the product will be around 15%, unless a dedicated experiment for a high precision measurement of θ_{12}, like the one described in [82], is built. This experiment could reduce the error on the product to a few percent.

Keeping Δm^2_{21} fixed is not a good approximation

3.7 Inclusion of degeneracies in the final result

In the example of the previous section five solutions were left in the analysis, even after the inclusion of spectral information and a constraint on the solar parameters. In the full analysis as described in appendix B and used to obtain the results of chapter 5 the multiplicity of solutions persists. This raises the question how to separate and classify the, in this context frequently used, terms degeneracy and correlation and how to present the results of the analysis in a concise way.

"Degeneracy"

One scheme to be found in the literature (*e.g.* in [92]) is to assign the term degenerate solution to any solution which fulfills the equations 3.19 and 3.20. Since the solar mass splitting is kept fixed, this is equivalent to defining degeneracy as the existence of disconnected solutions. The connectivity of solutions is, however, not a unique criterion for the classification since a complete analysis of degeneracies has to include spectral information, systematical errors, statistics and the state of knowledge on all parameters including the matter density. Once all those ingredients are taken into account a solution which was a point in parameter space becomes an extended region. The size of this region may be large enough to overlap with one or several of the regions around the other solutions, even neglecting the variation of the solar mass splitting. The extension of each region, in turn, depends sensitively on many factors, like the chosen confidence level or the detector performance (see appendix A). In many cases the χ^2-function retains an imprint of each of the possible solutions in the form of a local minimum. Whether this minimum is acceptable at a given confidence level can only be determined by a complete numerical calculation, the results of which will be presented in chapter 5. There are, however, also cases where there is no additional local minimum and the only consequence of the existence of a degenerate solution (at the level of total rates) in the full analysis is a strangely shaped allowed region. Thus there is no unique way to classify degenerate solutions, but there is a natural way to account for multiple

solutions in the full analysis. This is going to be discussed at the end of this chapter, and precise definitions are given in equations B.4 – B.6.

"Correlation"

On the other hand the term correlation is used in statistics whenever the error on one quantity q gives a contribution to the error in the determination of another quantity p. The degree of correlation is quantified by the correlation coefficient. This correlation coefficient is determined by the Taylor expansion of the logarithm of the likelihood function around its minimum (see, *e.g.* [70]). Thus the assumption enters that the error δq is small enough for being taken into account by means of a Taylor expansion around the minimum. Expanding around an extremum leaves as first non-vanishing terms of the expansion the quadratic ones. Usually only these are considered for the estimation of the correlation coefficients. Thus correlation includes only the *local* dependence on δq. If the higher order derivatives are non-negligible or if there is another minimum, this definition is no longer useful as a scheme to identify the impact of δq on δp. It is thus very difficult to uniquely assign the errors on the determination of the CP-phase and θ_{13} to either correlation or degeneracy.

Adding to these problems is the question, how to present the results in view of the existence of multiple solutions. If there were real data this task would be straightforward – each solution would be treated equally. Thus there would be an island in the parameter space for each possible[7] solution. This would resemble very much the situation in which solar neutrino data has been for nearly four decades [44]. There, a plethora of solutions like LOW, VAC, SMA, LMA *etc.* existed and all of them were considered as being real, *i.e.* when quoting a lower bound on Δm^2_{21} the lowest value of all solutions for Δm^2_{21} at a given confidence level was used. However when the issue is the physics potential of a *future* experiment, there are evidently no data. Therefore the data have to be simulated. For this simulation a set of physical input parameters $\boldsymbol{\lambda}_0$ has to be chosen. This choice is of course guided by existing knowledge, like that on the atmospheric mass scale, however, there remains a great freedom. Otherwise there would be already conclusive evidence for a unique set $\boldsymbol{\lambda}_0$ and there would be no need for a further measurement. Thus the dimension of the problem gets doubled, *i.e.* if the parameter space has dimension N, a comprehensive study has to deal with dimension $2\,N$. It is therefore mandatory to condense as much information regarding the physics reach of an experiment as possible into one or at least very few numbers for each set $\boldsymbol{\lambda}_0$. This is basically a kind of data compression, which of course involves a loss of information to some extent. This loss of information is, however, preferable to being overwhelmed by the sheer amount of information. Thus the task is to find a set of numbers which allows in an optimal way to decide on the scientific "value" of an experiment. Of course the problem is the definition of "value" in this context. The community seems to have settled[8] on three main aspects which constitute the scientific "value" of an experiment for oscillation physics.

The need for data compression in the presentation of results

[7] Here "possible" refers to being statistically acceptable at a certain confidence level.
[8] at least according to the author's perception

The angle θ_{13}

θ_{13} is the primary goal, either to determine its value or to push the upper limit as far as possible. Its importance is due to the fact that any CP-effects scale proportional to $\sin 2\theta_{13}$. There are two quantities of interest, the sensitivity limit and the accuracy. The latter only plays a minor role in the literature, whereas the sensitivity limit is the focus of attention. Since there are no theoretical predictions for the value of θ_{13} an experiment which is sensitive to lower values of θ_{13} is more likely[9] to find a finite value of θ_{13}. In the two flavour case this limit was defined as the upper limit on θ_{13} which is derived from a null result, *i.e.* a result which gives no indication for a finite value of θ_{13}. For example, this was the case in the Chooz experiment [65]. The Chooz collaboration shows their exclusion plot as a two dimensional picture where the axes are $\sin^2 2\theta_{13}$ and Δm^2_{31} to express the fact that within the two neutrino framework, used in their analysis, the two quantities are not independent but correlated. This result on its own would *not* imply any upper bound on $\sin^2 2\theta_{13}$ since for very small values of Δm^2_{31} there is no bound any more. The virtue of this way of presenting their result is that there are other experiments like Super-K and other atmospheric neutrino experiments [3, 54] which yield an accurate measurement of Δm^2_{31}. Using this information the Chooz result can be converted into the usual bound on $\sin^2 2\theta_{13}$. If this information changes it is straightforward to update the bound on $\sin^2 2\theta_{13}$, this is for example the case with the latest update of Super-K [60].

Definition of the $\sin^2 2\theta_{13}$ limit

In a three flavour framework the situation is much more complicated. There are basically three additional problems: the correlation with δ, the presence of disconnected solutions within one set $\mathcal{T}_i$ and the presence of four sets $\mathcal{T}_i$. A very practical and simple definition for the sensitivity limit even in this case is to regard the limit as the largest of all possible values of $\sin^2 2\theta_{13}$ which is compatible[10] with the data set simulated for $(\sin^2 2\theta_{13})_0 = 0$. A larger value of $\sin^2 2\theta_{13}$ will thus be found by the experiment, whereas a lower value might be found *if and only if* there is additional information on either the CP-phase, the mass hierarchy or the quadrant of θ_{23}. It does not make sense to show the resulting limit as a function of the fitted δ. A result which is compatible with $\sin^2 2\theta_{13} = 0$ does not allow any inference on the value of δ, since the CP-phase becomes undefined in the case $\sin^2 2\theta_{13} = 0$. Thus if there is information on the value of the CP-phase then there necessarily must be also information on θ_{13}. In that case a combined analysis of both experiments will become necessary. The same line of reasoning also applies to the three additional limits obtained for each of the $\mathcal{T}_i$, however, in a somewhat less stringent way. It is very difficult or even impossible to determine the mass hierarchy (see *e.g.* [80]) or the quadrant of θ_{23} (see *e.g.* [98, 99]) when $\sin^2 2\theta_{13}$ is very small. The above definition was introduced in [80] and was later on adopted by the authors of [100]. A mathematical definition is to be found in equation B.4.

[9] This likelihood of course depends on a probability measure in θ_{13}, which would have to be specified to make this a quantitative statement.

[10] at the confidence level at which the limit is given

The mass hierarchy

Usually the determination of the mass hierarchy is regarded as an intermediate goal – it will be achieved on the way to leptonic CP-violation. Long baseline experiments are sensitive to the mass hierarchy by virtue of matter effects. Thus if $\sin^2 2\theta_{13} = 0$ there is no sensitivity to the mass hierarchy since the matter effects can no longer be detected. The mass hierarchy can be determined whenever there are only solutions for one mass hierarchy at a given confidence level. The existence of a single point at a given confidence level with opposite mass hierarchy destroys the sensitivity. Thus for a given set of input parameters $\boldsymbol{\lambda}_0$ one has to look for the global minimum of the χ^2-function with opposite mass hierarchy. This definition is the basis for the exact definition in equation B.5. The sensitivity strongly depends on $(\sin^2 2\theta_{13})_0$, the solar mass splitting $(\Delta m^2_{21})_0$ and the CP-phase δ_0. For any experiment[11] the sensitivity has a lowest value for one CP-phase δ_0^{low} and a highest value for another CP-phase $\delta_0^{\text{high}} \simeq \delta_0^{\text{low}} + \pi$. The value of δ_0^{low} depends only on the relative weight of the $\sin\delta$ and $\cos\delta$ terms in equation 3.1. Thus a fair comparison of several experiments has to involve the same choice of δ_0 in terms of δ_0^{low} or δ_0^{high}. It would, for example, be inadequate to compare two experiments A and B with a single value of δ_0 which coincides with δ_0^{low} for experiment A and with δ_0^{high} for experiment B. Therefore all sensitivity limits should be given either at δ_0^{low} or δ_0^{high}. In this work all limits are given for δ_0^{low}, which is a conservative choice, *i.e.* there may be lower values of $\sin^2 2\theta_{13}$ where the mass hierarchy could be determined. However, conservative as this choice may be, it ensures that the sensitivities of different experiments can be compared in a consistent way.

The CP-phase

The determination of the CP-phase δ is considered to be the ultimate goal of oscillation physics. For this measurement three different quantities of interest can be defined. First, the sensitivity to maximal CP-violation, *i.e.* can $\delta_0 = \pm\pi/2$ be distinguished from CP-conservation which occurs at $\delta = 0$ or $\delta = \pi$. This test is especially simple and includes multiple solutions in a natural way – any solution fitting $\delta = 0$ or $\delta = \pi$ has to be considered. Second, the sensitivity to *any* CP-violation, which is the same as the sensitivity to maximal CP-violation, besides that δ_0 now can take any value. A mathematical definition is given in equation B.6. Third, the accuracy in the determination of δ. It is not possible to assign a simple Gaußian error to δ if there are multiple solutions, which generally is the case. Even if it might be possible to assign a Gaußian error to each of the solutions, the problem of choosing one of them would still remain, especially since the errors have a large variation for the different solutions. An alternative quantity of interest has therefore been defined in [80]: the coverage in δ. Here all values of δ which are acceptable at a given confidence level are considered, *i.e.* the union of all allowed ranges is given in units of 2π. This quantifies the amount of the unit circle which remains as a possible solution for δ. The coverage in δ depends on δ_0 and the worst (*i.e.* largest) value is given.

Sensitivity to maximal CP-violation

Coverage in δ

[11] with the exception of reactor neutrino experiments

Chapter 4

Dramatis personæ

In this chapter the various experimental setups studied in this work are introduced. A special focus will be to highlight the similarities and differences between different experimental approaches for determining the neutrino mixing parameters. Furthermore a description of the employed analysis techniques is given as well as the definition of the standard parameters used throughout this work.

4.1 The experiments

In general a neutrino oscillation experiment will be tuned such that the observed energy range covers the first oscillation maximum[1]. The condition for the oscillation maximum is given by

$$\Delta m^2 \, L/E = \pi/2 \,. \tag{4.1}$$

The experiments considered here are all optimized for the measurement of effects associated with the atmospheric mass splitting Δm^2_{31}. Before introducing these experiments in detail a simple comparison of their sampling of the L/E-space is given in figure 4.1, where the number of signal events is given as a function of L/E. All superbeam experiments (JHF-SK, NuMI, and JHF-HK) have their highest event rates in that L/E region where the oscillation maximum for $\Delta m^2_{31} \simeq 3.0 \cdot 10^{-3}\,\mathrm{eV}^2$ is located. The sampled range in L/E of the NuMI setup is somewhat smaller than the ones of the JHF experiments, which leads to a stronger Δm^2_{31}-dependence of the physics reach of NuMI which is discussed in detail in section 5.2. The range in L/E covered by a neutrino factory is rather large compared to the other experiments. The maximum of the event rates however occurs at $L/E \simeq 150\,\mathrm{km\,GeV}^{-1}$, which is clearly far off the value for which the oscillation maximum occurs for the currently favored values of $\Delta m^2_{31} \simeq 3.0 \cdot 10^{-3}\,\mathrm{eV}^2$. This has severe consequences regarding the impact of multiple solutions as shown in section 5.5. The L/E sampling of the reactor setups is not shown in figure 4.1, since they are disappearance experiments and

L/E sampling

[1] For an exception see [101]. There the possibilities which are offered by observing higher order maxima are discussed.

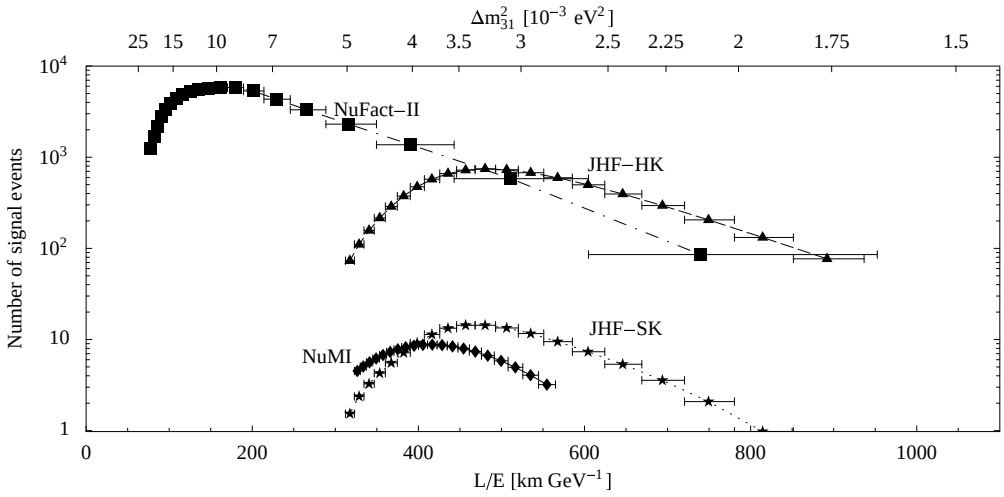

Figure 4.1: *The number of signal events per bin (equidistant in energy) as a function of L/E for the setups indicated by the corresponding labels. On the upper edge of the frame the position of the first oscillation maximum for a given value of Δm^2_{31} is depicted. The horizontal error bars give the bin size in units of L/E. The event numbers are calculated for the* LMA-I *numbers which are defined in equation 4.5 with* $\sin^2 2\theta_{13} = 0.1$ *and* $\delta = 0$. *They include the detector efficiencies and the energy resolution as defined in appendix A.2.*

the number of signal events is a misleading quantifier of the obtainable accuracy. The sampled range roughly corresponds to the one covered by the JHF experiments.

4.1.1 Reactor

Reactor neutrino experiments have a long and successful history. The first detection of a neutrino was achieved by a reactor experiment in 1956 [102] and awarded with a Nobel prize in 1995. This great start was succeeded by a number of neutrino oscillation experiments, the most important are: Gösgen [62], Bugey [63], Palo Verde [64], and Chooz [65]. The Chooz experiment provides today the most stringent limit on $\sin^2 2\theta_{13}$. Most recently the Kamland experiment has provided the solution to the longstanding solar neutrino puzzle [5]. The basic idea behind these experiments is that a nuclear reactor is a very powerful and pure source of $\bar{\nu}_e$, which are then detected by inverse β-decay

$$\bar{\nu}_e + p \longrightarrow e^+ + n\,, \tag{4.2}$$

with a threshold energy of 1.804 MeV. This reaction has a very distinct signature consisting of the prompt γ-rays of the annihilation of the positron and the delayed signal of the capture of the neutron. This delayed coincidence is the key for the rejection of most of the backgrounds. The relation of the observed, *i.e.* in the detector visible, energy E_{vis} to the true neutrino energy $E_{\bar{\nu}_e}$ is particularly simple and allows a unique determination of the true energy (for details

see appendix A.2.1). These experiments can measure only the disappearance of $\bar{\nu}_e$. The oscillation probability for this transition is taken from [94] and given by

$P_{\bar{\nu}_e \to \bar{\nu}_e}$ is independent of δ and θ_{23}

$$P_{\bar{\nu}_e \to \bar{\nu}_e} \simeq 1 - \sin^2 2\theta_{13} \sin^2 \Delta_{31} - \alpha^2 \Delta_{31}^2 \cos^4 \theta_{13} \sin^2 2\theta_{12}\,, \qquad (4.3)$$

where the dependence on Δm^2_{21} and θ_{13} has been approximated by an expansion of the full three neutrino probability in the spirit of equation 3.1. At the baselines and energies considered here matter effects can safely be neglected. Clearly $P_{\bar{\nu}_e \to \bar{\nu}_e}$ does neither depend on the CP-phase δ nor on θ_{23} and therefore this transition channel is free of degeneracies.

In view of the Chooz experiment is has been proposed to build a new reactor neutrino oscillation experiment to improve the Chooz bound [98, 103–105]. The new ingredient for an improved reactor experiment is to use a near and a far detector in order to reduce the various systematical errors to the necessary low levels. The main problem with a disappearance experiment is that the normalization uncertainty strongly affects the sensitivity of the experiment. This can to some extent be alleviated by using a near and a far detector. The remaining uncertainty is due to the relative normalization uncertainty between the two detectors. Furthermore the spectral shape is uncertain at some level due to the limited knowledge on the fuel composition and the neutrino spectra. This error is again strongly reduced by the comparison of near and far detector and only the relative energy calibration error of the two detectors remains. Thus the systematical error can be parameterized by a normalization uncertainty σ_{norm} of 0.8% and an energy calibration error σ_{cal} of 0.5% (for an exact definition see appendix A.2.1). All reactor setups in this work have a baseline of 1.7 km for the far detector and a baseline of 170 m for the near detector[2]. The size of the event sample is determined by the thermal reactor power (GW), the fiducial detector mass times efficiency (t) and the operation time of the experiment (y), thus the integrated luminosity is given by the product of these three factors and has the unit t GW y. Two setups with different integrated luminosities are used in this work: Reactor-I with 400 t GW y and Reactor-II with 8 000 t GW y. The latter setup roughly corresponds to a Kamland sized detector at a typical nuclear power plant running for a few years.

Spectrum vs. normalization uncertainty

4.1.2 NuMI

The NuMI experiment will use the same neutrino beam line as Minos and thus has a pion decay based muon neutrino beam. NuMI will therefore be able to observe the $\nu_\mu \to \nu_e$ transition. One difference to the Minos experiment will be that NuMI uses the beam in the so called off-axis configuration, *i.e.* the detector is placed several kilometers from the beam direction from Fermilab to Soudan. The off-axis concept was introduced in [106] and is based on simple relativistic kinematics. At a certain angle γ to the flight direction of the pion the energy of the neutrino produced in the decay of the pion becomes practically independent

The off-axis concept

[2] The consequences of relaxing this assumption are discussed in detail in [94] and it is found that near detector baselines up to several hundred meters do not degrade the performance significantly.

of the pion energy. A detector placed at this angle γ with respect to the decay pipe thus receives a beam, which has a very narrow energy spectrum compared to the on-axis beam. The high-energy tail is practically absent, which offers a strong reduction of the neutral current background[3]. The mean energy of this off-axis beam is 2.2 GeV. The other difference is that the NuMI detector will be a rather highly segmented low-Z calorimeter. The main types of interactions at those energies for ν_e are quasi elastic and inelastic[4] charged current events, thus requiring a detector which also measures the hadronic energy deposition, *i.e.* a calorimeter. The high segmentation is necessary to provide a sufficient discrimination of ν_e events against π^0's produced in neutral current interactions. Another irreducible source of background to the ν_e appearance is the presence of a small fraction $\sim 0.5\%$ of electron neutrinos in the beam. The whole project is described in detail in a letter of intent [88] and the parameterization of the experiment follows closely this letter of intent and can be found in appendix A.2.2. The detector will have a fiducial mass of 17 kt and will be placed at a distance of 712 km at an off-axis angle of 0.72°. The power on target is scheduled to be 0.4 MW and the experiment is going to run for five years. This setup will be denoted by NuMI throughout this work.

4.1.3 JHF

The JHF experiment uses a neutrino beam which is produced in the Japan proton accelerator research complex (JPARC) and directed towards the Kamioka mine, which currently houses Kamland and Super-K. The beam is again a pion decay based muon neutrino beam, very similar to the NuMI beam. The JHF experiment will also use the off-axis technique described in the previous section in order to reduce the high-energy tail of the beam. The off-axis angle for JHF is 2°. The baseline is with 295 km much shorter than the one of NuMI. Therefore a lower beam energy is required to meet the condition for the oscillation maximum in equation 4.1. The lower mean beam energy of 0.8 GeV implies that the fraction of quasi-elastic interactions is much larger and therefore there is no need to determine the hadronic energy deposition in the detector. This allows to use the Super-K detector, a water Cherenkov detector with a fiducial mass of 22.5 kt. Super-K has a very good ability to identify electron neutrino charged current events and to reject neutral current events, mainly π^0's. The JHF beam also contains a contamination of ν_e at the level of $\sim 0.5\%$. The power on target is planned to be 0.77 MW and the running time is five years. This initial stage will be denoted by JHF-SK.

Upgrade to JHF-HK

There also exists a plan to increase the size of the event sample by improving the proton intensity from 0.77 MW to 4 MW and to build a new water Cherenkov detector with a fiducial mass of 1 000 kt, which is called Hyper-K. This second stage will include running with an anti-neutrino beam. The total running time of eight years is split into two years of neutrino running and six years of anti-neutrino running. This distribution of running times is chosen such that the number of events in both modes is roughly the same. The three

[3] Neutral current events tend to feed down from high energies into the analysis range.
[4] mainly pion production

times longer anti-neutrino running is necessary to compensate for the much lower anti-neutrino cross section. This upgraded version of the experiment is denoted by JHF-HK. A detailed description of both stages can be found in a letter of intent [87]. The parameterization of the experiment used in this work closely follows this paper and can be found in appendix A.2.3.

4.1.4 Neutrino factory

A neutrino factory is based on the idea of using muon decay instead of pion decay to produce neutrinos [107]. The muons are circulated in a storage ring with long straight sections. The decay of muons in these straight sections produces an intense and pure beam of ν_μ and $\bar{\nu}_e$. The possibility to store anti-muons[5] also exists and in this case the beam consists of $\bar{\nu}_\mu$ and ν_e. The muons are produced by pion decay and have to be cooled in phase space in order to make a beam which can be accelerated. This cooling is planned to be achieved by means of so called ionization cooling, a technique which has not been demonstrated so far. The Mice experiment is dedicated to prove this concept [108]. There exist other approaches to this problem and detailed information can be gained from several design studies performed in Europe, the United States and Japan [109]. A nice overview is also given in a CERN yellow book [89]. The next step is to accelerate the muons to the desired storage energy and to transfer them into the storage ring where they are circulated until they have decayed. The appearance signal $\bar{\nu}_e \to \bar{\nu}_\mu$ in a neutrino factory experiment consists of anti-muons (in case muons are stored) produced by charged current deep inelastic scattering. The anti-muons have to be cleanly separated from the muons produced by the surviving ν_μ. These anti-muons are called wrong sign muon events, since they have the opposite charge relative to the muons in the storage ring. The charge identification is achieved by a magnetized iron calorimeter, which is similar to the Minos detector and described in detail in [110][6]. The calorimeter also provides a reasonable energy resolution for the hadronic part of each event, thus an event-by-event energy reconstruction of the neutrino energy is possible. The optimum combination of muon energy and baseline is considered to be around 50 GeV and 3 000 km (see *e.g.* [111]). The neutrino factory setup considered in this work has a total of $4.24 \cdot 10^{21}$ useful muon decays at a muon energy of 50 GeV, divided into 50% muons and 50% anti-muons. This corresponds to a power on target of 4 MW and a total running time of eight years [109]. The fiducial mass of the detector is 50 kt and the baseline is 3 000 km. This setup is labeled NuFact-II and the details of the parameterization can be found in appendix A.2.4.

Muon cooling

Wrong sign muons

4.2 Analysis technique & standard parameters

In order to assess the physics potential of an experiment, the result of the experiment is simulated for a given set of true oscillation parameters $\boldsymbol{\lambda}_0$. The

[5] by selecting π^+ instead of π^- at the target

[6] There are some subtleties concerning the detector performance discussed in detail in the appendices of [80].

calculation of the event rates is described in detail in appendix A.1. In a second step the simulated data are analyzed in very much the same fashion as real data would be – a fit to the data is performed. The fit is based on a χ^2-function, which is defined in appendix B. The χ^2-analysis proceeds in the usual way in order to obtain the allowed ranges for each parameter of interest. In the computation of the χ^2 the full spectral information of all bins is included[7]. Also the data of both appearance and disappearance channels are used simultaneously for NuMI, JHF-SK, JHF-HK and NuFact-II. The data of the disappearance channel constrain the atmospheric parameters Δm^2_{31} and θ_{23}. The solar parameters Δm^2_{21} and θ_{12} enter the oscillation probability in equation 3.1 only in the form of

Long baseline setups

$$\pi_{\text{sol}} := \Delta m^2_{21} \cdot \sin 2\theta_{12} \,, \tag{4.4}$$

therefore only this product is considered a free parameter in the analysis. All setups studied in this work cannot determine π_{sol} accurately and therefore external information is used to constrain π_{sol}. This information is provided by the Kamland experiment and the expected accuracy for three years of Kamland data is $\sim 15\%$ error at $1\,\sigma$ on π_{sol} [97, 112], thus an error of this size is assumed. The above mentioned setups all have to a varying extent non-negligible matter effects and the matter density uncertainty can strongly influence the result. Therefore also the matter density is treated as a free parameter and a $1\,\sigma$ error of 5% is assumed [113]. Furthermore the effects of various systematical uncertainties are included (see appendix B).

For the reactor setups Reactor-I and Reactor-II no appearance data is available and the disappearance channel cannot provide an accurate determination of Δm^2_{31}. Therefore the assumption is made that Δm^2_{31} will be well constrained by the next generation of long baseline experiments, Minos and CNGS. The $1\,\sigma$ error on Δm^2_{31} is therefore taken to be 10% [114], the results do not change even for errors as large as 50%. The survival probability of $\bar{\nu}_e$ does not only depend on π_{sol} as it can be seen from equation 4.3 and therefore the approximation of using only π_{sol} is abandoned and Δm^2_{21} and θ_{12} are treated as separate parameters with a $1\,\sigma$ error of 10% each [97, 112]. Matter effects do not play a role for the reactor setups and therefore the matter density is fixed to $\rho = 0$, restoring the vacuum case. Again the effects of various systematical uncertainties are included (see appendix B).

Reactor setups

Besides the above given approximations the oscillation probabilities are computed numerically exact in the three flavour scheme with constant matter densities of $2.8\,\text{g}\,\text{cm}^{-3}$ for NuMI, JHF-SK and JHF-HK and of $3.5\,\text{g}\,\text{cm}^{-3}$ for NuFact-II. The numerical complexity introduced by treating all oscillation parameters as free is considerable, *e.g.* for the computation of figure 5.12 a total of 10^8 probabilities, $5 \cdot 10^6$ convolutions with the detector response function and 10^6 evaluations of the χ^2-function were needed, consuming a total of 48 h CPU-time on a Pentium IV[8] with 2.4 GHz.

Finally the standard values of the oscillation parameters are introduced.

[7] The required energy response functions and the respective number of bins are given for each experiment in appendix A.2.

[8] Pentium IV is a registered trademark of the Intel corporation.

The LMA-I numbers are LMA-I and LMA-II

$$\begin{aligned} \Delta m^2_{31} &= +3.0 \cdot 10^{-3}\,\mathrm{eV}^2\,, \\ \sin^2 2\theta_{23} &= 1\,, \\ \Delta m^2_{21} &= +7 \cdot 10^{-5}\,\mathrm{eV}^2\,, \\ \sin^2 2\theta_{12} &= 0.8\,, \end{aligned} \tag{4.5}$$

and the LMA-II numbers are given by

$$\begin{aligned} \Delta m^2_{31} &= +3.0 \cdot 10^{-3}\,\mathrm{eV}^2\,, \\ \sin^2 2\theta_{23} &= 1\,, \\ \Delta m^2_{21} &= +1.4 \cdot 10^{-4}\,\mathrm{eV}^2\,, \\ \sin^2 2\theta_{12} &= 0.8\,. \end{aligned} \tag{4.6}$$

For $\sin^2 2\theta_{13}$ only values below the Chooz bound of 0.1 are considered, whereas the CP-phase can assume any value.

Latest Super-K results

During the final stage of this work the Super-K collaboration has presented an updated analysis of their existing data and the new best-fit value for the atmospheric mass splitting has been shifted downwards to $2.0 \cdot 10^{-3}\,\mathrm{eV}^2$ [60]. The analysis presented in [60] does not include any new data but the detector parameterization has been changed. The lower value of Δm^2_{31} implies that all sensitivities presented in chapter 5 will deteriorate. For the $\sin^2 2\theta_{13}$ sensitivity the dependence on the true value of Δm^2_{31} is explicitly given. The Super-K collaboration has presented an updated analysis of the day/night asymmetry in solar neutrinos as well [115]. It seems that this new analysis excludes the LMA-II solution at $3\,\sigma$. However this conclusion can depend sensitively on details of the analysis and is therefore to be considered with caution.

Chapter 5

Main results

The results shown in the following present an update and extension of those obtained in [80, 94–96]. They are organized according to the scheme introduced in chapter 3. First those experiments which have only one observable, *i.e.* exclusively only neutrino or anti-neutrino sources available, are discussed and their ability to determine $\sin^2 2\theta_{13}$ is studied in dependence of Δm^2_{31} and Δm^2_{21}. As it was shown in section 3.3 they cannot have any sensitivity to the mass hierarchy or restrict the CP-phase δ. Therefore it is necessary to combine these initial experiments in order to gain some physics potential concerning the mass hierarchy and CP-effects. The next logical step is to consider setups which have two observables in a single experiment, *i.e.* both neutrino and anti-neutrino sources available. The combination of neutrino and anti-neutrino data is a very powerful tool to alleviate the consequences of not knowing the CP-phase in advance and thus improves the ability to measure $\sin^2 2\theta_{13}$ considerably. The determination of the mass hierarchy becomes feasible for those experiments which have sufficiently long baselines and high enough energies in order to have large matter effects. These experiments have a very good potential to measure the leptonic CP-phase and to discover CP-violation in the lepton sector. Finally the issue of combining several of these setups in order to resolve degeneracies is discussed.

5.1 Reactor

The two reactor setups which are discussed in the following do not fit neatly into the organizing principle of this chapter, since they use instead of the apperance transition $\nu_e \leftrightarrow \nu_\mu$ the disappearance mode $\bar{\nu}_e \rightarrow \bar{\nu}_e$. This poses considerable experimental challenges as discussed in section A.2.1 and in more detail in [94]. The big advantage is however that the transition probability $P_{\bar{\nu}_e \rightarrow \bar{\nu}_e}$ does not depend on the CP-phase δ. Furthermore by choosing the baseline such that the first oscillation peak of the atmospheric mass splitting Δm^2_{31} is clearly within the energy range of the experiment the influence of the solar parameters Δm^2_{21} and θ_{12} becomes very small. Thus a reactor experiment provides a theoretically very clean laboratory to study θ_{13}.

$P_{\bar{\nu}_e \rightarrow \bar{\nu}_e}$ is independent of the CP-phase

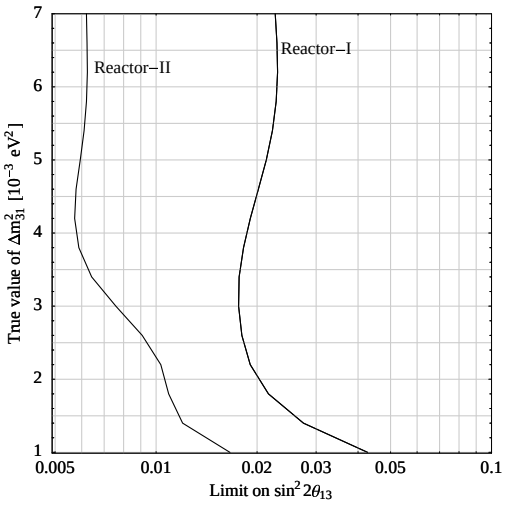

Figure 5.1: *The sensitivity limits on* $\sin^2 2\theta_{13}$ *as functions of the true value of* Δm^2_{31}. *They are shown for the* Reactor-I *and* Reactor-II *setups at the* 90% *confidence level. The variation of the limit with* Δm^2_{21} *is negligibly small and therefore not shown.*

In figure[1] 5.1 the sensitivity limit to $\sin^2 2\theta_{13}$ as a function of Δm^2_{31} is shown at 90% cl. It is clearly visible that the baseline of 1.7 km is optimized for a value of Δm^2_{31} around $3.0 \cdot 10^{-3}\,\mathrm{eV}^2$. The limit does not change perceptibly for different values of Δm^2_{21}, therefore the dependence on Δm^2_{21} is not shown. The only oscillation parameter whose correlation is sizeable is Δm^2_{31}. In principle a reactor experiment can also measure Δm^2_{31} via the position of the oscillation dip in the event rate spectrum, whose depth depends on the value of $\sin^2 2\theta_{13}$. This determination, however, is much less accurate even for large values of $\sin^2 2\theta_{13}$ than what will be achieved by long baseline experiments like Minos and CNGS [114]. Thus the constraint on Δm^2_{31} which will be derived by Minos and CNGS is used in order to minimize the impact of this correlation. It turns out that an error on Δm^2_{31} of around $30 - 50\%$ is tolerable and the result does not improve once this error is reduced.

Long baseline data constrains Δm^2_{31}

The obtainable sensitivity depends crucially on the level of systematic errors and backgrounds. On the basis of the total event rate the sensitivity for a disappearance experiment is given by the overall normalization uncertainty, *e.g.* a normalization error of 1% would wash out any disappearance signal at the same level of $\sim 1\%$. However if the number of events is large enough, the spectral signature of oscillations is very distinct and cannot be destroyed by an overall normalization uncertainty. In fact, for very high statistics experiments like Reactor-II it becomes possible, by exploiting the spectral information, to determine the normalization as an independent parameter simultaneously with $\sin^2 2\theta_{13}$ to a very good accuracy. In that case the limit is rather independent of the normalization uncertainty and other error sources become dominant. The most relevant source of additional systematical errors is the limited knowledge

Spectrum allows to measure the normalization

[1] All figures in this chapter are calculated for the LMA-I numbers as true parameters, with exception of those true parameters shown on the axes.

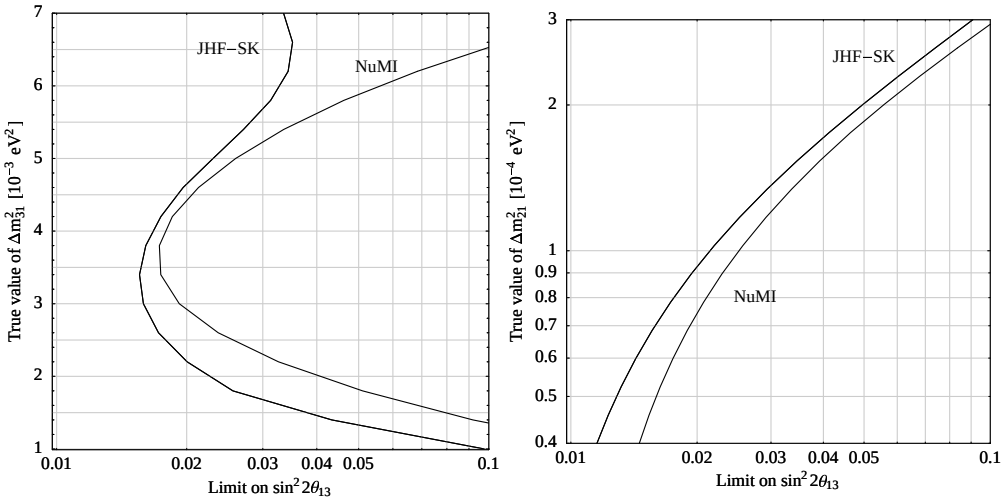

Figure 5.2: *The sensitivity limits on* $\sin^2 2\theta_{13}$ *as functions of the true values of* Δm^2_{31} (*left plot*) *or* Δm^2_{21} (*right plot*)*, respectively. They are shown for the* JHF-SK *and* NuMI *setups at the* 90% *confidence level. In the right figure, only the* Kamland*-allowed region is shown.*

on the isotope composition of the reactor and the accuracy of the neutrino spectra. These uncertainties can be largely canceled by the comparison of near and far detector. To which extent this cancellation occurs is however strongly dependent on the degree of equality of the energy response of the near and the far detector. For example an energy calibration error may spoil this cancellation. Another limiting factor is the possible presence of backgrounds, which are not the same for near and far detector. The different background levels have their origin in several factors like the different overburden and counting rate of near and far detector. The level to which the cancellation works can only be determined by an intensive R&D program. In [94] a detailed study of the impact of different levels of systematical errors is presented and the main conclusion is that with a moderate improvement on previous experiments like Chooz it seems possible to reach sensitivities to $\sin^2 2\theta_{13}$ at the order of 10^{-2}, which is a one order of magnitude improvement compared to the existing limit.

5.2 Initial superbeam

The initial superbeam experiments JHF-SK and NuMI will provide a measurement of Δm^2_{31} and $\sin^2 2\theta_{23}$ of unprecedented accuracy by observing with very high statistics the $\nu_\mu \to \nu_\mu$ transition [87, 88]. Their main purpose however is either to measure θ_{13} or to improve the limit. Both experiments are in their current configuration optimized for a value of Δm^2_{31} around $3.0 \cdot 10^{-3}\,\mathrm{eV}^2$. This can also be clearly seen in the left hand panel of figure 5.2, where the limit on $\sin^2 2\theta_{13}$ at 90% cl is shown as a function of Δm^2_{31} for both setups. The performance of both experiments is very similar, which is not surprising, since

NuMI and JHF-SK are very similar

both experiments observe the $\nu_\mu \to \nu_e$ transition in the first oscillation peak. The dependence of the limit obtained at NuMI on Δm^2_{31} is somewhat more pronounced since the beam is relatively narrower than the one of JHF-SK (see also figure 4.1). The dependence of the limit on Δm^2_{21} is shown in the right hand panel of figure 5.2. Again the behavior of the experiments is very similar for the same reasons as already stated. In contrast to a reactor experiment, JHF-SK and NuMI suffer a strong reduction of their capability to improve the limit on $\sin^2 2\theta_{13}$ when the solar mass splitting Δm^2_{21} becomes larger. At the largest currently allowed value of $\Delta m^2_{21} \simeq 3.0 \cdot 10^{-4}\,\mathrm{eV}^2$ they can no longer yield any improvement compared to the Chooz bound. This behavior is nicely described by equation 3.16 and explained in section 3.3. Its origin is the fact that the CP-phase is not known and strongly correlated with θ_{13}.

No improvement on Chooz for large Δm^2_{21}

Both JHF-SK and NuMI have the same level of background (~ 20 events) due to a contamination of the beam with ν_e (~ 10 events) and a certain fraction of neutral current events misidentified as ν_e event (~ 10 events). Even if it was possible to improve the neutral current rejection by a factor of ten the overall background would be only reduced by a factor of 2, which in turn would improve the performance only by a factor of $\sqrt{2}$. A reduction of the beam contamination is not possible for this kind of beams. The systematical uncertainty of these backgrounds of approximately 5% is not relevant since the statistical error is with $\sim 20\%$ much larger. Thus the only major improvement possible is to increase either the luminosity, the detector mass or the running time, *i.e.* the cost of the experiment.

5.3 Combinations of initial experiments

None of the so far discussed experiments has on its own the ability to test the mass hierarchy or to restrict the CP-phase, albeit for different reasons. The reactor setups Reactor-I and Reactor-II are not sensitive to the mass hierarchy, since there are no matter effects at those energies and baselines[2]. The CP-phase cannot be accessed by reactor experiments, because $P_{\bar\nu_e \to \bar\nu_e}$ does not depend on δ. JHF-SK and NuMI have only one observable and can access neither the mass hierarchy nor the CP-phase for the reasons described in section 3.3.

However, the limitations of these experiments can, to some degree, be circumvented by combining their data in a suitable way. This issue has also been studied in [95, 117].

Sensitivity to the mass hierarchy

The determination of the mass hierarchy requires sufficiently large matter effects and a second observable to break the ambiguity introduced by the CP-phase. Thus any combination of experiments has to involve NuMI, since NuMI has the largest baseline and highest energy of all the initial experiments and therefore

[2] In [116] it was pointed out that there is an interference effect in the transition probability, which leads in principle to a sensitivity to the mass hierarchy even in the absence of matter effects. This was studied in great detail with a simulation of the experiment in [82]. It turns out that this effect is not relevant for the setups under consideration here.

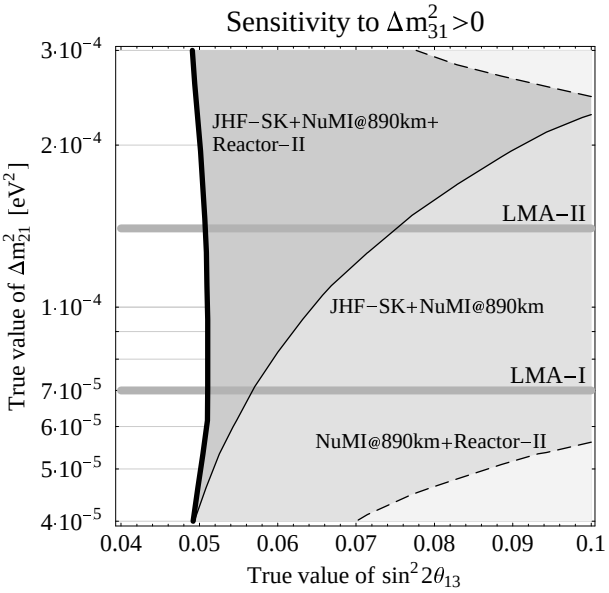

Figure 5.3: *The sensitivity to a positive sign of* Δm^2_{21} (*normal mass hierarchy*) *as a function of the true values of* $\sin^2 2\theta_{13}$ *and* Δm^2_{21} *within the* Kamland*-allowed region. Sensitivity at the 90% confidence level exists on the right-hand sides of the curves. It is shown for several combinations of experiments: for* JHF-SK *combined with* NuMI *at a baseline of* 890 km [95]*, for* NuMI *at a baseline of* 890 km *combined with* Reactor-II*, and for* JHF-SK *combined with* NuMI *at a baseline of* 890 km *and* Reactor-II*. The* LMA *best-fit values are marked by the horizontal grey lines. This figure is taken from* [94].

Large matter effects are essential

the largest matter effects. However, it turns out that even NuMI in its original configuration with a baseline of 712 km is not optimal. The best choice is to build the NuMI far detector at a baseline of 890 km, which is the longest baseline at the off-axis angle of 0.72°. The second observable could be delivered by an anti-neutrino run at NuMI itself, however the cross section and the beam luminosity make this an unfavorable scenario. A better choice is to use the data of the JHF-SK neutrino run to break the δ ambiguity. The resulting sensitivity is shown in figure 5.3 at 90% cl as a function of $\sin^2 2\theta_{13}$ and Δm^2_{21}. Again there is a strong degradation of the sensitivity for increasing Δm^2_{21}, since the matter effects become weaker relative to the increasing CP-effects. Adding the data of Reactor-II improves the situation considerably, since they strongly restrict the possible values of $\sin^2 2\theta_{13}$, which in turn excludes certain values of the CP-phase. In that case the sensitivity is nearly independent of the solar mass splitting and a determination of the mass hierarchy is possible for $\sin^2 2\theta_{13} > 0.05$.

Sensitivity to δ

The measurement of the CP-phase requires either the inclusion of anti-neutrino data or a precise determination of θ_{13}. The first possibility is shown in figure 5.4 with the label JHF-SK$_{cc}$, where the subscript *cc* indicates a sharing of the total

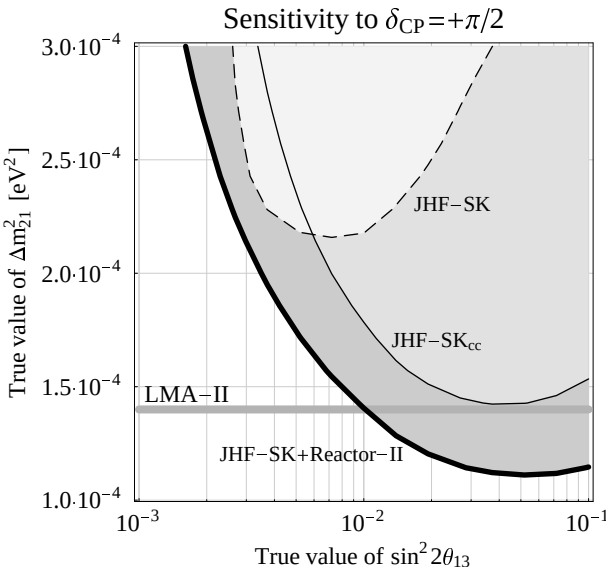

Figure 5.4: *The sensitivity to maximal CP violation $\delta_{CP} = +\pi/2$ as a function of the true values of $\sin^2 2\theta_{13}$ and Δm^2_{21} within the* Kamland*-allowed region. Sensitivity at the 90% confidence level is given on the upper sides of the curves. It is shown for* JHF-SK (*neutrino running only*), JHF-SK$_{cc}$ (*same overall running time split into neutrino and anti-neutrino running with about equal numbers of events*), *and* JHF-SK (*neutrino running only*) *combined with* Reactor-II. *The* LMA-II *best-fit value is marked by the horizontal grey line. This figure is taken from* [94].

running time on neutrinos and anti-neutrinos in such a way that the number of events for both modes is approximately the same. In figure 5.4 the sensitivity to maximal CP-violation for the case $\delta_0 = +\pi/2$ is shown as a function of $\sin^2 2\theta_{13}$ and Δm^2_{21}. Those two parameters determine the size of CP-effects, since CP-effects are suppressed by the smallest mass splitting (Δm^2_{21}) and the smallest angle (θ_{13}). The curve labeled JHF-SK$_{cc}$ barely touches the LMA-II value of Δm^2_{21}. A better option is to run JHF-SK exclusively with neutrinos and to use the reactor data to constrain $\sin^2 2\theta_{13}$, which is shown as the curve labeled JHF-SK+Reactor-II. This combination has a much better reach in both Δm^2_{21} and $\sin^2 2\theta_{13}$. The reason for this is that the reactor data can replace the anti-neutrino run at JHF-SK with a much better statistical accuracy.

Avoid anti-neutrino running

5.4 Advanced superbeam

An advanced superbeam experiment like JHF-HK has both neutrino and anti-neutrino running, therefore it belongs to the category of experiments which have intrinsically two observables. The physics reach is strongly improved by this, however the parameter dependence of the corresponding sensitivities is rather involved because of the existence of multiple solutions as already discussed in sections 3.5 and 3.6. In the presence of multiple solutions it can become very difficult to summarize the results of an experiment in only a couple of numbers,

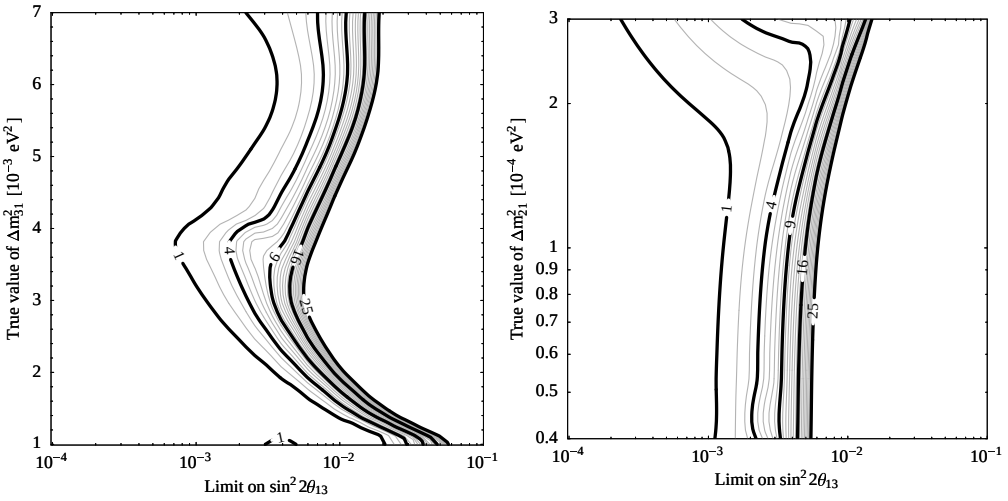

Figure 5.5: *Sensitivity limit on* $\sin^2 2\theta_{13}$ *for* JHF-HK *as a function of the true value of* Δm^2_{31} *(left hand panel) and of* Δm^2_{21} *(right hand panel). Shown are contours of constant* χ^2_{L}*, the thick black lines have a value of* χ^2_{L} *given by the corresponding labels, whereas the thin grey lines are separated by* $\Delta\chi^2_{\mathrm{L}} = 1$*.*

as it was discussed in detail in section 3.7. Therefore the presentation of the results will differ from the previous section. At some points it will be necessary to go into more detail and to highlight the complexity which originates from multiple solutions.

θ_{13} sensitivity

The combination of neutrino and anti-neutrino data restricts the set of possible solutions of equations 3.8 considerably and once spectral information is included disconnected solutions can appear. As a consequence χ^2_{L} may no longer be monotonous, there can even appear additional local minima. In those cases the limit as a function of the confidence level may become discontinuous. Therefore the limit at a fixed confidence level may cease to be a meaningful quantity. For this reason the contours of constant χ^2_{L} are shown in figure 5.5. The sensitivity limit as defined in section 3.7 at a certain confidence level is then given by the position of the rightmost point on the contour with the corresponding value of χ^2_{L} for a fixed value of the true parameters[3].

The dependence of the $\sin^2 2\theta_{13}$ limit on Δm^2_{31} has not changed very much in comparison to figure 5.2 as it can be seen from the left hand panel in figure 5.5. However the right hand panel clearly shows that the dependence on Δm^2_{21} is very different. It does no longer break away at large values of Δm^2_{21}, in fact at low confidence levels, below $3\,\sigma$, the limit improves for large values of Δm^2_{21} in contrast to the result of section 5.2. The reason for this different behavior is that the possible combinations of the CP-phase δ and $\sin^2 2\theta_{13}$ are

Anti-neutrino data improves Δm^2_{21} dependence

[3] χ^2_{L} is defined in equation B.4.

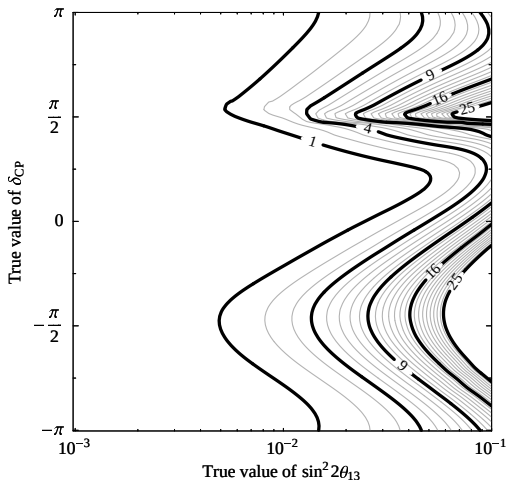

Figure 5.6: *Sensitivity to normal mass hierarchy for* JHF-HK *as a function of the true values of* $\sin^2 2\theta_{13}$ *and* δ*. Shown are contours of constant* χ^2_{H}*, the thick black lines have a value of* χ^2_{H} *given by the corresponding labels, whereas the thin grey lines are separated by* $\Delta\chi^2_{\mathrm{H}} = 1$*.*

highly restricted and the degree of rejection of certain CP-phases increases with increasing Δm^2_{21}. At even larger values of Δm^2_{21} (not allowed by Kamland and not shown in figure 5.5) a second minimum in χ^2_{L} appears due to the intrinsic ambiguity as defined in equation 3.34. Within the Kamland-allowed range of Δm^2_{21} a sensitivity limit at 90% cl of $\sim 2 \cdot 10^{-3}$ can be reached. A further improvement on this value is hardly possible since the limit is already dominated by the systematical background uncertainty. For an even lower limit a neutrino factory is necessary.

Sensitivity to the mass hierarchy

JHF-HK has too little matter effects

JHF-HK is not very well suited to determine the mass hierarchy since its baseline is too short and its energy too low to develop sizeable matter effects. However, there exists a proposal to direct a high energy beam from the Brookhaven National Laboratory towards the Homestake mine onto a megaton water Cherenkov detector [101]. This experiment would be much more suited to perform a measurement of the mass hierarchy since the matter effects are much larger. However no reliable background estimates for this proposal have been presented and it is not clear whether a water Cherenkov detector has a sufficient neutral current rejection at those energies. Therefore this idea is not considered further here and instead the capabilities of JHF-HK to determine the mass hierarchy are discussed.

In figure 5.6 the contours of constant χ^2_{H} are shown[4] as a function of the true values of $\sin^2 2\theta_{13}$ and δ. The true data set was computed with a normal mass hierarchy and the LMA-I values. For every point on the contour where $\chi^2_{\mathrm{H}} = 9$ the inverted mass hierarchy is excluded at $3\,\sigma$ cl. First of all the dependence

[4] χ^2_{H} is defined in equation B.5

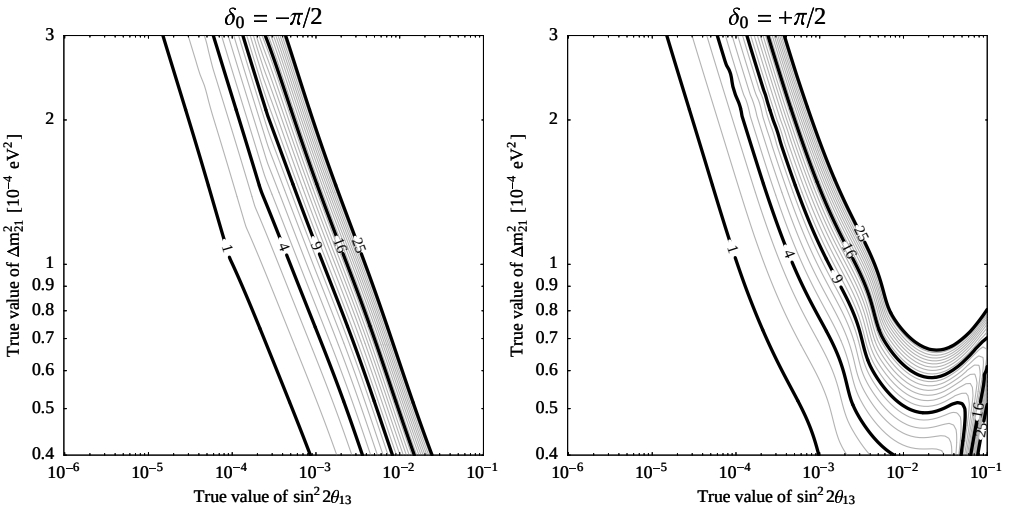

Figure 5.7: *Sensitivity to maximal* CP*-violation for* JHF-HK *as a function of the true values of* $\sin^2 2\theta_{13}$ *and* Δm^2_{21}*. In the left hand panel contours of constant* $\chi^2_{\mathrm{CP}}(-\pi/2)$ *are shown, whereas in the right hand panel contours of constant* $\chi^2_{\mathrm{CP}}(+\pi/2)$ *are depicted. The thick black lines have a value of* $\chi^2_{\mathrm{CP}}(\pm)$ *given by the corresponding labels, whereas the thin grey lines are seperated by* $\Delta\chi^2_{\mathrm{CP}}(\pm) = 1$*.*

on δ is very pronounced, the $2\,\sigma$ contour ($\chi^2_{\mathrm{H}} = 4$) varies by nearly one order of magnitude in $\sin^2 2\theta_{13}$. Second there is a cusp at $\delta_0 \simeq \pi/2$ which originates from a jump by π in the fitted value of δ. The reason for this jump is that there are two local minima in the χ^2-function separated by π and at $\delta_0 = \pi/2$ the global minimum jumps from one to the other local minimum. Some details to this mechanism can be found in [118]. This nicely illustrates the complexity introduced by the presence of multiple, disconnected solutions. The strong dependence on δ_0 makes it very difficult to quote a single value of $\sin^2 2\theta_{13}$ down to which the mass hierarchy can be determined. Furthermore the sensitivity to the mass hierarchy also strongly depends on the true value of Δm^2_{21}. It tends to decrease with increasing values of Δm^2_{21} and for very large values it improves again. The value of Δm^2_{21} where the turnover happens is also dependent on the value of δ_0.

Sensitivity to δ

As already discussed in section 3.7 there are several quantifiers for the ability to measure δ. In this section two of them are used in order to illustrate the performance of JHF-HK for the determination of the CP-phase – the sensitivity to maximal CP-violation and the sensitivity to any CP-violation. The exact definitions of maximal CP-violation $\chi^2_{\mathrm{CP}}(\pm)$ and any CP-violation χ^2_{CP} are given in equation B.6.

In figure 5.7 the sensitivity to maximal CP-violation is shown as a function of the true values of $\sin^2 2\theta_{13}$ and Δm^2_{21}. The lines are contours of constant $\chi^2_{\mathrm{CP}}(\pm)$,

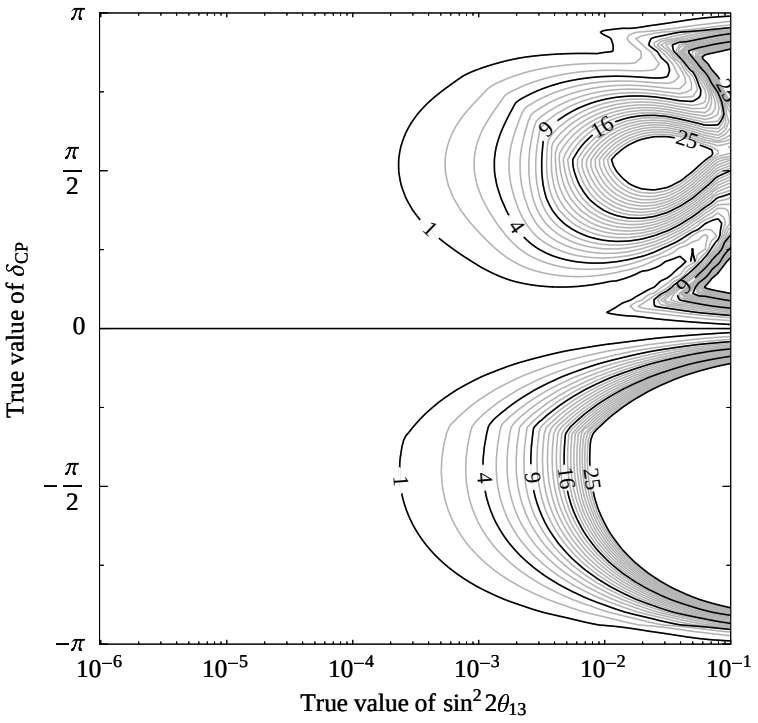

Figure 5.8: *Sensitivity to any* CP*-violation for* JHF-HK *as a function of the true values of* $\sin^2 2\theta_{13}$ *and* δ*. Shown are contours of constant* $\chi^2_{\rm CP}$*, the thick black lines have a value of* $\chi^2_{\rm CP}$ *given by the corresponding labels, whereas the thin grey lines are separated by* $\Delta\chi^2_{\rm CP} = 1$*.*

where the thick black lines have a value of $\chi^2_{\rm CP}(\pm)$ given by the corresponding labels, whereas the thin grey lines are separated by $\Delta\chi^2_{\rm CP}(\pm) = 1$. In the left hand panel the case $\delta_0 = -\pi/2$ is shown. In this case the sensitivity has a very simple behavior – it improves when $\sin^2 2\theta_{13}$ and/or Δm^2_{21} get larger. This reflects just the fact that CP-effects are supressed by both Δm^2_{21} and $\sin^2 2\theta_{13}$. Furthermore the simplicity of the curves indicates that in this case multiple solutions do not play an important role. In contrast the case $\delta_0 = +\pi/2$ shown in the right hand panel of figure 5.7 exhibits an interesting structure for low values of Δm^2_{21} and the largest values of $\sin^2 2\theta_{13}$. This valley in the lower right corner of the plot is due to the phenomenon called π-transit. The solution in the halfspace where $\Delta m^2_{31} < 0$ has a different value for the CP-phase than δ_0, and for changing true values of $\sin^2 2\theta_{13}$ δ_0 is continuously mapped to any fitted value of the CP-phase. For a specific true value of $\sin^2 2\theta_{13}$ $\delta_0 = +\pi/2$ is mapped to $\delta = \pi$ [80]. The position of the π-transit depends also on the true value of Δm^2_{21}, therefore the locations of the π-transit map out a line in the $\sin^2 2\theta_{13}$-Δm^2_{21} plane. In the case of JHF-HK the π-transit only occurs in an approximate sense, since $\delta_0 = +\pi/2$ is never exactly mapped to $\delta = \pi$.

Approximate π-transit

The feature of an approximate π-transit is also visible in the upper half of figure 5.8 (see also [118]). In this figure the sensitivity to any CP-violation is shown as a function of the true values of $\sin^2 2\theta_{13}$ and δ. The lines are contours

of constant χ^2_{CP}, where the thick black lines are labeled with the values of χ^2_{CP}. The thin grey lines are separated by one unit in χ^2_{CP}. As already mentioned the two valleys for positive δ_0 and large $\sin^2 2\theta_{13}$ are due to the π-transit. Except for the region where the π-transit occurs JHF-HK offers an excellent discovery potential for leptonic CP-violation provided $\sin^2 2\theta_{13}$ is larger than $\sim 10^{-2}$. From figures 5.7 and 5.8 it is also obvious that in some cases the problem of multiple solutions is a severe limitation in the search for CP-violation.

5.5 Neutrino factory

The presence of multiple, disconnected solutions at a neutrino factory is much more pronounced than for superbeam experiments. A neutrino factory with a baseline of 3 000 km does not operate at the first oscillation maximum; for a value of $\Delta m^2_{31} = 3.0 \cdot 10^{-3}\,\text{eV}^2$ the first maximum occurs at 7.3 GeV, an energy at which the detector efficiency is very low. Most events at a neutrino factory are coming from energies around 30 GeV. Therefore a neutrino factory is operating clearly off-peak (see also figure 4.1) and this strongly increases the problems associated with multiple solutions as it will be shown in the following.

θ_{13} sensitivity

On the basis of a simple two neutrino approximation the sensitivity of a neutrino factory to $\sin^2 2\theta_{13}$ should be exceedingly good, since the background levels are extremely low and the statistics is very large. In the original paper [107] sensitivities around 10^{-5} are found. It was, however, realized later[5] that within a three neutrino framework and with the currently favored values for Δm^2_{21} this picture has to be revised [80, 81, 84, 92, 93, 96]. The main problem is that $\sin^2 2\theta_{13}$ and the CP-phase are highly correlated, which was discussed in the context of a neutrino factory in [119, 120]. Earlier works on CP-effects can be found in [121]. The CP-phase is not only correlated with θ_{13} but, even worse, may give rise to multiple solutions (see sections 3.5 and 3.6).

The χ^2_{L} at a neutrino factory usually has a second minimum which makes the definition of a limit somewhat ambiguous. This is illustrated in figure 5.9, where the limit on $\sin^2 2\theta_{13}$ is shown as a function of the true values of Δm^2_{31} (left hand plot) and of Δm^2_{21} (right hand plot). The lines are contours of constant χ^2_{L}. The dependence on Δm^2_{31} does not exhibit the typical oscillation feature as for example in the left hand panel of figure 5.2, because at a neutrino factory most events do not originate from the oscillation maximum. For small values of Δm^2_{31} χ^2_{L} clearly has a second minimum around $\sin^2 2\theta_{13} \simeq 10^{-2}$. Its origin is the intrinsic ambiguity as defined in equation 3.34. This second minimum is rather deep and appears already at the $1\,\sigma$ cl. With increasing Δm^2_{31} the position of the second minimum moves to lower values of $\sin^2 2\theta_{13}$ and at the same time it becomes shallower. The reason for this behavior is that with increasing Δm^2_{31} the ratio α of Δm^2_{21} to Δm^2_{31} decreases. Thus the terms containing the CP-phase dependence in equation 3.1 loose relative weight

Multiple solutions – two minima in χ^2_{L}

[5] In the development of the field the neutrino factory came a long time before superbeams, thus basically all initial works dealt with the case of a neutrino factory.

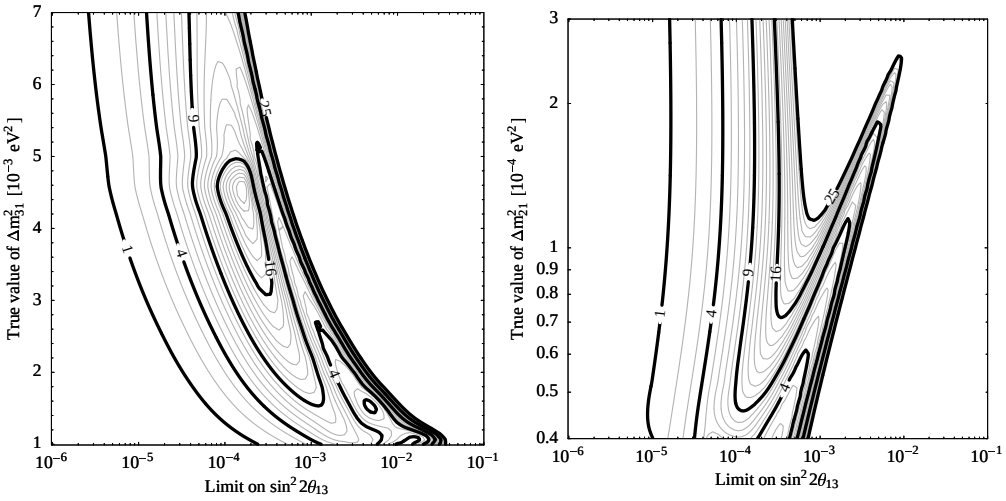

Figure 5.9: *Sensitivity limit on* $\sin^2 2\theta_{13}$ *for* NuFact-II *as a function of the true value of* Δm^2_{31} *(left hand panel) and of* Δm^2_{21} *(right hand panel). Shown are contours of constant* χ^2_{L}*, the thick black lines have a value of* χ^2_{L} *given by the corresponding labels, whereas the thin grey lines are separated by* $\Delta\chi^2_{\mathrm{L}} = 1$*.*

and the effects of the CP-phase are smaller. A similar argument applies also for the dependence on Δm^2_{21}, which is shown in the left hand panel of the same figure. With increasing Δm^2_{21} the ratio α also increases and the position of the second minimum is moved to larger values of $\sin^2 2\theta_{13}$. At the same time the CP-effects and the statistics become larger, thus improving the rejection of the second solution. The confidence level at which the second minimum appears therefore increases with Δm^2_{21}.

Figure 5.9 also illustrates the problems associated with the definition of the sensitivity limit as in section 3.7. At $3\,\sigma$ CL the limit as a function of Δm^2_{21} would exhibit a discontinuity at $\Delta m^2_{21} \simeq 1.1 \cdot 10^{-4}\,\mathrm{eV}^2$, immediately below this value the limit is $2 \cdot 10^{-3}$ and immediately above it is 10^{-4}. The position of this discontinuity obviously depends sensitively on the chosen confidence level.

Sensitivity to the mass hierarchy

The sensitivity to the mass hierarchy at a neutrino factory is in principle very good, since the baseline is very long and the energy is high enough to savely cover the MSW-resonance energy of roughly 10 GeV. In a two neutrino approximation, *i.e.* $\Delta m^2_{21} = 0$ the sensitivity to the mass hierarchy is approximately the same as for $\sin^2 2\theta_{13}$ [122]. This is no longer true for values of $\Delta m^2_{21} > 10^{-5}\,\mathrm{eV}^2$. The basic effect of changing the mass hierarchy is that the MSW-resonance is moved from neutrinos to anti-neutrinos, thus the relative number of events in both channels is shifted. The CP-phase can have the same effect due to the different sign of the $\sin\delta$ term in equation 3.1 for neutrinos and anti-neutrinos. Therefore it is in principle possible to mask the effect of the mass hierarchy by changing the fitted value of the CP-phase. The extent to which this masking is

CP-phase versus matter effects

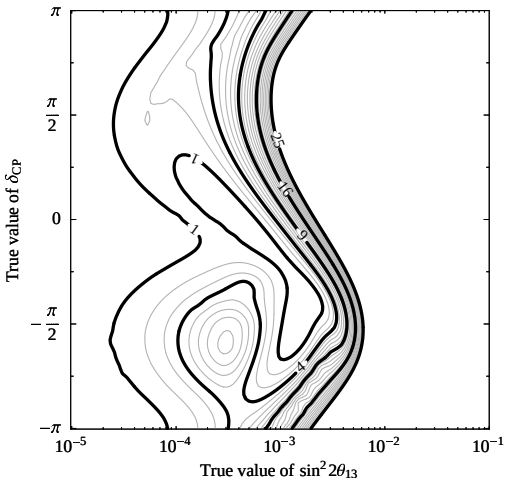

Figure 5.10: *Sensitivity to normal mass hierarchy for* NuFact-II *as a function of the true values of* $\sin^2 2\theta_{13}$ *and* δ*. Shown are contours of constant* χ^2_{H}*, the thick black lines have a value of* χ^2_{H} *given by the corresponding labels, whereas the thin grey lines are separated by* $\Delta\chi^2_{\text{H}} = 1$*.*

possible strongly depends on the true value of the CP-phase, *e.g.* for $\delta = 0$ the difference between neutrino and anti-neutrino transition probabilities is minimal[6] and therefore a shift of the fitted CP-phase can compensate for changing the mass hierarchy in the fit. If on the other hand the difference between neutrino and anti-neutrino probability due to the CP-phase is already maximal it may become very difficult to do so. Therefore the sensitivity to the mass hierarchy should show a strong dependence on both the true value of $\sin^2 2\theta_{13}$ and the true value of δ.

For this reason in figure 5.10 the sensitivity to the mass hierarchy is shown as a function of the true values of $\sin^2 2\theta_{13}$ and δ. The lines are contours of constant χ^2_{H} and the black lines are labeled with the values of χ^2_{H}, whereas the grey lines are separated by $\Delta\chi^2_{\text{H}} = 1$. As expected from the previous paragraph the dependence on both parameters is strong. The $5\,\sigma$ curve behaves in a nice sinusoidal way. However at lower confidence levels many features appear, especially for $\delta_0 = -\pi/2$. The reason is that also for this measurement the interplay of the CP-phase and matter effects is very important and as it will be explained in more detail in the next section a very interesting effect occurs at $\delta_0 = -\pi/2$. As already mentioned for JHF-HK the sensitivity first decreases with increasing Δm^2_{21}, but recovers for even larger values of Δm^2_{21}. Also for NuFact-II the value of Δm^2_{21} where this turnover happens is dependent on the true value of the CP-phase.

Due to the problems associated with the interplay of matter and CP-effects it could be necessary to go to longer baselines around 7 000 km where the CP-effects are completely supressed by matter effects. This observation has been

Very long baseline helps

[6]This is true for negligible matter effects, once they are sizeable the value at which the minimal and maximal difference occurs is shifted (see section 3.4).

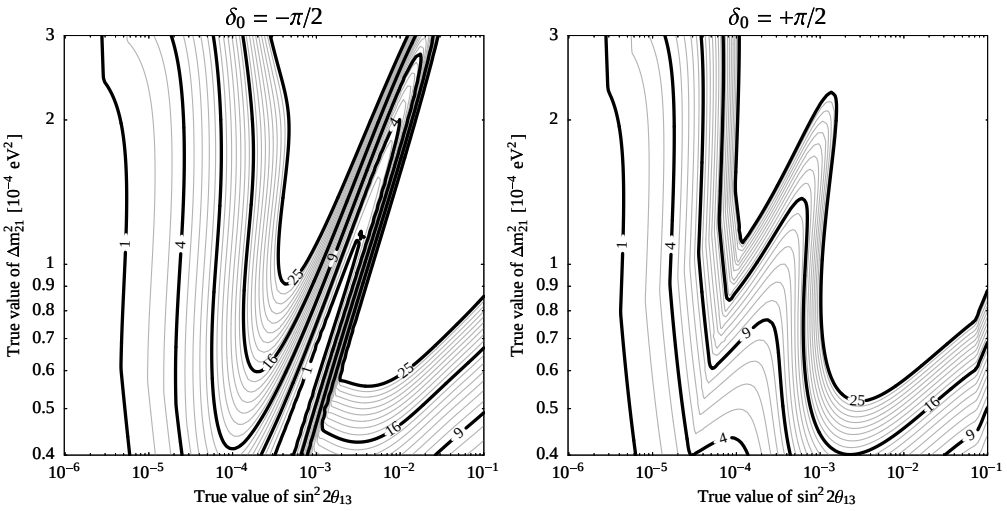

Figure 5.11: *Sensitivity to maximal* CP*-violation for* NuFact-II *as a function of the true values of* $\sin^2 2\theta_{13}$ *and* Δm^2_{21}*. In the left hand panel contours of constant* $\chi^2_{\rm CP}(-\pi/2)$ *are shown, whereas in the right hand panel contours of constant* $\chi^2_{\rm CP}(+\pi/2)$ *are depicted. The thick black lines have a value of* $\chi^2_{\rm CP}(\pm)$ *given by the corresponding labels, whereas the thin grey lines are separated by* $\Delta\chi^2_{\rm CP}(\pm) = 1$*.*

independently made by several authors [84, 92, 120, 122] and was pursued in detail in [96] where it was shown that at the magic baseline of $\sim 7\,300$ km it is possible to determine the mass hierarchy at $3\,\sigma$ cl down to values of $\sin^2 2\theta_{13}$ of 10^{-4} independently of δ and Δm^2_{21}.

Sensitivity to δ

As for JHF-HK in the previous section the sensitivity to maximal CP-violation and the sensitivity to any CP-violation will be used in order to quantify the performance of NuFact-II for the determination of the CP-phase (for the definition of these quantities see equation B.6).

In figure 5.11 the sensitivity to maximal CP-violation is shown as a function of the true values of $\sin^2 2\theta_{13}$ and Δm^2_{21}. The lines are contours of constant $\chi^2_{\rm CP}(\pm)$ and the black lines are labeled accordingly. The grey lines are separated by one unit in $\chi^2_{\rm CP}(\pm)$. In both cases $\delta_0 = \pm\pi/2$ there is a valley in $\chi^2_{\rm CP}(\pm)$.

π-transit

The origin of the valley in the left hand panel ($\delta_0 = -\pi/2$) is the already described π-transit. The valley is very deep and basically reaches $\chi^2_{\rm CP}(\pm) \simeq 0$ for most values of Δm^2_{21}. The valley in the right hand panel ($\delta_0 = +\pi/2$) is far less pronounced and originates from a similar source as the valley in the $\sin^2 2\theta_{13}$-sensitivity shown in the right hand panel of figure 5.9. The simple reason is that there are multiple solutions which in some cases lie exactly at the fitted value of $\delta = \pi$. Obviously the presence of multiple solutions also presents a severe problem at a neutrino factory. The strong upward bending of the contours in both panels at large $\sin^2 2\theta_{13} > 10^{-3}$ is exclusively due to

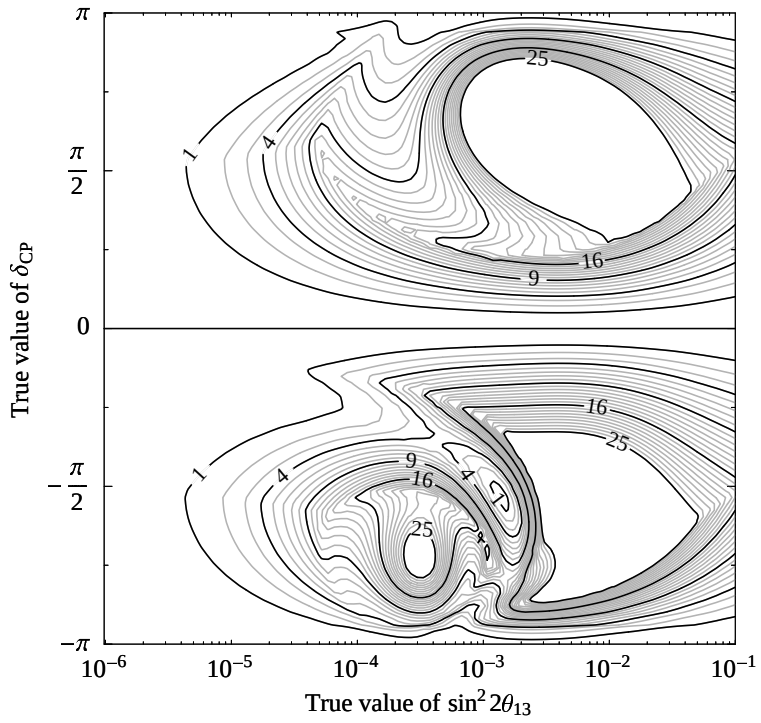

Figure 5.12: *Sensitivity to any* CP*-violation for* NuFact-II *as a function of the true values of* $\sin^2 2\theta_{13}$ *and* δ*. Shown are contours of constant* $\chi^2_{\rm CP}$*, the thick black lines have a value of* $\chi^2_{\rm CP}$ *given by the corresponding labels, whereas the thin grey lines are separated by* $\Delta\chi^2_{\rm CP} = 1$*.*

Matter density uncertainty is the dominant error source for large $\sin^2 2\theta_{13}$

the matter density uncertainty of 5%. A reduction of this error to 1% would strongly reduce this effect and the sensitivity at $\sin^2 2\theta_{13} \simeq 10^{-3}$ would prevail up to the Chooz bound. The issue of the impact of matter density uncertainties and different parameterizations is discussed in very great detail in *e.g.* [123], whose references furthermore provide a detailed picture of the large number of works dealing with this topic.

The sensitivity to any CP-violation exhibits an even more complex dependence on the true values of $\sin^2 2\theta_{13}$ and δ as it is shown in figure 5.12. The lines are now contours of constant $\chi^2_{\rm CP}$ and once more the thick black lines are labeled with the according values of $\chi^2_{\rm CP}$ and the grey lines are separated by one unit. The semilunar valley for negative values of δ is due to the π-transit and becomes very deep ($\chi^2_{\rm CP} < 1$) at around $\sin^2 2\theta_{13} = 10^{-3}$ and $\delta = -\pi/2$, clearly reflecting the valley in the left hand panel of figure 5.11. For positive values of the CP-phase there is now a much shallower valley, which becomes relevant only for $\sin^2 2\theta_{13}$ smaller than $\sim 5 \cdot 10^{-4}$. Also this feature has a clear correspondence in the right hand panel of figure 5.11. The deterioration of the sensitivity for relatively large values of $\sin^2 2\theta_{13} > 10^{-3}$ is again solely due to the matter density uncertainty. This effect makes JHF-HK a more accurate experiment at large values of $\sin^2 2\theta_{13} > 10^{-2}$ (see figure 5.8). Therefore it seems necessary to improve the knowledge of the matter profile along the specific baseline of a

neutrino factory considerably. Clearly the issue of improving the accuracy of the knowledge of the matter profile deserves further intensive studies once a neutrino factory enters into the stage of having a proposal submitted.[7]

5.6 Possible strategies to resolve degeneracies

In the previous sections it was shown that the presence of multiple solutions considerably impairs the physics capabilities of the second generation experiments. For this reason a number of possible remedies have been proposed. They all have in common that they rely on the inclusion of complementary data in the analysis in order to lift at least some degeneracies.

Superbeam & neutrino factory

In [124] the combination of an advanced superbeam experiment with the data of a neutrino factory was studied. In this paper it was found that this combination can successfully remove degeneracies for values of $\sin^2 2\theta_{13}$ larger than 10^{-3} in an approximation where only θ_{13} and δ were considered as free parameters in the fit. The complementarity of neutrino factories and superbeams is due to the fact that the latter work at the oscillation peak whereas a neutrino factory does not. The different energy dependence of the four terms in equation 3.1 then allows to reject many of the multiple solutions. For small values of $\sin^2 2\theta_{13}$ below 10^{-3} the problem arises that the superbeam data is completely dominated by background and systematical errors and therefore ceases to be useful.

Silver channel

Another possibility is to extend the class of possible final states in the oscillation, *i.e.* the detection of ν_τ's. This was studied in detail in [99], the so called "silver" channel allows to resolve degeneracies very cleanly down to values of $\sin^2 2\theta_{13}$ around 10^{-3}. Again these studies were performed in the approximation of only two free parameters: θ_{13} and δ. The value of the $\nu_e \to \nu_\tau$ transition lies in its complementary behavior with respect to δ and θ_{23}. The experimental challenge imposed by the routine detection of ν_τ's is considerable and in [99] a detailed study of the performance of an Opera-like detector [125] is performed, with the result that for $\sin^2 2\theta_{13}$ below 10^{-3} the silver channel becomes background dominated. Another possibility for the clean detection of ν_τ's could be the liquid argon technology currently under development for the Icarus [126] experiment.

β-beam

A novel idea for a very bright and clean source of ν_e has been proposed in [127] – the β-beam. Here the decay of relatively short-lived β-unstable nuclei is used to produce an intense beam of ν_e in very much the same fashion as a neutrino factory exploits the decay of muons. It is also possible to produce $\bar{\nu}_e$ by using a different nucleus. The advantage of this type of beam compared to conventional beams is that the beam is very clean – there are only ν_e or $\bar{\nu}_e$ in the beam and the spectrum is very well known. The main technological challenges are the production of the radioactive nuclei in a sufficient abundance and the issue of radioactive contamination of the whole facility. The β-beam would be highly complementary to a superbeam since it would observe the same

[7] NB – Seismometers are very cheap compared to the estimated cost of a neutrino factory. One seismometer has roughly the same price as one photomultiplier.

probability however with interchanged initial and final state. Thus the sign of the $\sin\delta$ term in equation 3.1 is opposite. However up to now no study on this option has been performed in order to demonstrate its capability to resolve degeneracies. It is to be expected that this combination should work excellently down to $\sin^2 2\theta_{13} \simeq 10^{-3}$. At this point the superbeam data become dominated by backgrounds and systematical errors. The β-beam itself however may go down much further in $\sin^2 2\theta_{13}$ provided it is possible to reach the required luminosities. The physics potential of a β-beam is studied in [128], however not including multiple solutions.

Finally the possibility exists to have two baselines at a neutrino factory simultaneously, since the shape of the storage ring easily offers two baselines. The optimal combination would be to have one detector at $\sim 3\,000$ km and the other at around 7 200 km. This observation has been independently made by several authors [84,92,120,122]. The usefulness of this combination for resolving degeneracies has been demonstrated in [96]. The longer baseline has the special feature that at this specific baseline the dependence of the oscillation probability on Δm^2_{21} and δ vanishes due to matter effects. Therefore this baseline is called magic and the condition for it is

Magic baseline

$$\sin(\Delta\hat{A}) = 0 \quad \Leftrightarrow \quad \sqrt{2}G_F n_e L = 2\pi\,, \tag{5.1}$$

yielding a value for L of 7 250 km for a realistic matter profile. The magic baseline allows to cleanly resolve degeneracies down to values of $\sin^2 2\theta_{13}$ below 10^{-4}. The technical challenge here is to build the storage ring at a rather steep angle.

Each of these possibilities offers its advantages but also has some drawbacks. Especially the size of $\sin^2 2\theta_{13}$ will play an important role in deciding which option is the most suitable. It is however very important to keep in mind that in the light of possible deviations from the CKM-like mixing of three lepton flavours it will be crucial to have several independent measurements of the oscillation parameters. Furthermore it will be necessary for high precision neutrino physics to drastically reduce the errors on the solar parameters.

Testing the CKM mechanism

Chapter 6

Conclusion & outlook

The flavour transitions of atmospheric and solar neutrinos have now been convincingly proven and they are the first clear evidence for physics beyond the Standard Model. The most plausible mechanism for these flavour transitions is neutrino oscillation and therefore a broad experimental program is underway to test this mechanism. Under the assumption that neutrinos oscillate the results of Kamland rule out any other solution than LMA, with a relatively large solar mass splitting and mixing angle. The size of both the mass splitting and the angle imply that three flavour effects cannot be neglected for precision neutrino oscillation physics and even the discovery of leptonic CP-violation may now be possible. Although neutrino oscillation has been discovered with natural neutrino sources, the road to high precision experiments leads inevitably to the use of artificial neutrino sources. The uncertainties connected with the production of neutrinos in natural sources are already now larger than most other experimental errors, therefore any improvement of the experiments has to start with the source.

The proposed new neutrino sources include nuclear reactors, superbeams, β-beams and neutrino factories. For many of the new experiments also advances in detector technology are envisaged like megaton scale water Cherenkov detectors. In this work the physics potential of a subset of the possible combinations of sources and detectors for future experiments was discussed. Specifically the sensitivities to the small mixing angle θ_{13}, to the mass hierarchy and to CP-violation were studied and the obtainable sensitivities for reactor experiments, initial and advanced superbeams and a neutrino factory were given. Moreover some possible combinations of the different setups were evaluated and their potential to resolve degeneracies was discussed. The analysis strategy was presented in detail based on an analytical description of the problem. New results on the location of degenerate solutions were obtained and a classification scheme for experiments was introduced. For a subset of experiments an analytical expression for the sensitivity limit to θ_{13} was derived, which agrees very well with the full, numerical calculation. The statistical analysis was performed in a full three flavour framework, where the correlation of all oscillation parameters is included as well as the existence of multiple solutions. Matter effects can substantially alter the oscillation probabilities and were therefore accurately

treated and specifically a possible uncertainty was taken into account. The basis for the statistical analysis was the computation of the event rates in each experiment. A detailed simulation of the detector response was performed to calculate the event rates and the most relevant sources of systematical errors have been considered. The detector simulation has been carefully calibrated against the available literature.

The reactor setups Reactor-I and Reactor-II do not have any sensitivity to the mass hierarchy or to CP-violation due to the form of the electron neutrino disappearance probability. This implies that the reactor setups are free of any degeneracy and therefore allow an unambiguous extraction of θ_{13}. In order to keep the systematical errors at bay it is mandatory to use a near detector. The sensitivity[1] to the small mixing angle was found to be around $\sin^2 2\theta_{13} \simeq 10^{-2}$, which is comparable to what initial superbeams can achieve. The determination of θ_{13} at a reactor experiment is independent of the value of the solar mass splitting, which is a big advantage especially for large Δm^2_{21}.

Two possible initial superbeam experiments have been studied: NuMI and JHF-SK. Both setups are rather similar with the main difference that NuMI has a much longer baseline and therefore matter effects are more pronounced. NuMI and JHF-SK each can probe $\sin^2 2\theta_{13}$ down to $\sim 10^{-2}$ for the LMA-I parameters. However the sensitivity to θ_{13} completely breaks away for large values of Δm^2_{21}. None of the two can achieve any sensitivity to the mass hierarchy or CP-violation in their initially proposed configuration.

Several combinations of the initial superbeam and reactor setups were investigated and it was found that the various combinations largely increase the physics potential. For the determination of the mass hierarchy the optimal combination involves Reactor-II, to fix the value of θ_{13}, JHF-SK, to alleviate the effects of the unknown CP-phase, and NuMI with a longer baseline, to obtain sufficient matter effects. This combination is able to determine the mass hierarchy down to $\sin^2 2\theta_{13} \simeq 0.05$ independent of the value of the solar mass splitting. The optimal combination for the discovery of CP-violation is given by JHF-SK running exclusively with neutrinos and Reactor-II. Again Reactor-II was found to be useful to constrain θ_{13}. With this combination the first step towards leptonic CP-violation is possible, however the parameters, especially the solar mass splitting, have to be favorable.

JHF-HK was chosen as a representative of an advanced superbeam experiment. Its sensitivity to θ_{13} was found to go down to $\sin^2 2\theta_{13} \simeq 2 \cdot 10^{-3}$ for the LMA-I parameters. This limit is rather stable under a change of the solar mass splitting. The sensitivity to the mass hierarchy is poor because the baseline and energy do not give rise to sizeable matter effects. JHF-HK was shown to have a good discovery potential for CP-violation for all values of the solar mass splitting provided $\sin^2 2\theta_{13}$ is bigger than 10^{-2}. For very large values of $\sin^2 2\theta_{13}$ this setup can yield a high precision measurement of the leptonic CP-phase.

The ultimate tool for oscillation physics is a neutrino factory. The NuFact-II setup was therefore expected to outperform all other options studied in this work. In the case of NuFact-II it became obvious, however, that the structure

[1] All results in this chapter are given at 90% cl.

of the oscillation probabilities introduces a considerable amount of complexity in the analysis of the data. Therefore it is not straightforward to summarize the sensitivities of NuFact-II in just a couple of numbers. The numbers given in the following should be considered as a rough guideline and for a more accurate picture the corresponding figures should be consulted. With this caveat in mind, the sensitivity to $\sin^2 2\theta_{13}$ is around 10^{-4} at the LMA-I parameters but changes strongly for different parameter values and confidence levels (see figure 5.9). The sensitivity of NuFact-II to the mass hierarchy is very good and reaches down to $\sin^2 2\theta_{13} \simeq 10^{-3}$. However it displays a pronounced dependence on the true value of the CP-phase and the solar mass splitting (see figure 5.10). Finally a neutrino factory can discover maximal CP-violation down to very small values of $\sin^2 2\theta_{13} \simeq 2 \cdot 10^{-5}$ quite independent of the true value of the solar mass splitting (see figure 5.11). However the determination of the CP-phase is hindered at large values of θ_{13} due to the matter density uncertainty (see figure 5.12). The topology of the projected χ^2 is in general rather complicated. Therefore it depends strongly on the exact location in the parameter space how well the CP-phase can be constrained. This is the most impressive example for the degree of complexity which is induced by the presence of multiple solutions.

Several possibilities to resolve degeneracies and thus to improve the performance of the experiments have been briefly discussed. For instance the magic baseline is able to resolve the degeneracies for $\sin^2 2\theta_{13} \geq 10^{-4}$.

The techniques presented in this work are well suited to study other new experiments like β-beams. They seem to offer a very competitive option even compared to a neutrino factory. However it is very difficult to compare the results presented here with the published results on β-beams, since the latter results have been obtained with a much less sophisticated analysis technique. Also the effects of including the silver channel, *i.e.* the possibility to detect tau neutrinos, clearly deserve further studies. Beyond the precision determination of neutrino mixing parameters testing the three neutrino mixing is a very interesting and important topic as well. Similar to the quark sector, where a large effort is under way to measure the CKM-matrix with a very high precision, the same program is necessary for neutrinos. The first step could be to test the unitarity of the leptonic mixing matrix. In case leptonic CP-violation is discovered it will become of paramount importance to clarify which mechanism is responsible for this effect. It could be caused by the CP-phase in the mixing matrix, but also other origins are conceivable, *e.g.* non-standard interactions of neutrinos. Many models for generating neutrino masses give rise to such interactions and therefore the interplay of oscillation and non-standard interactions is a rich area for further research. Summarizing, neutrinos have provided us with the first clear evidence for physics beyond the Standard Model and it is to be expected that many more surprises lie ahead in neutrino physics.

Note added in proof

During the very last stage of this work the SNO collaboration has released improved neutral current results on solar neutrinos [129]. The new data are in good agreement with previous results and the hypotheses of no flavour transition

is excluded with more than $7\,\sigma$. The constraint on the solar mixing has improved as well and maximal mixing is now rejected at $5.4\,\sigma$. The LMA-II solution is disfavored at more than 99% cl. The analysis presented in [129] does not yet include the latest result of Super-K on the day/night asymmetry [115], which by themselves seem to exclude LMA-II at $3\,\sigma$. Thus it is to be expected that in a combined analysis LMA-II will be ruled out at more than $3\,\sigma$.

Acknowledgments

I wish to express my gratitude to my supervisor Manfred Lindner for being an excellent teacher and a patient boss, who left me any freedom I needed to pursue my interests. It was a great pleasure to work and learn at his chair for more than three years. Also I would like to thank the people with whom I have done most of my work. Walter Winter deserves special thanks for being the guinea pig for the software on which this work is based. Thanks to Martin Freund who introduced me to neutrino physics, computer graphics and programming. I have to thank Thomas Schwetz for making my stay in Valencia much more enjoyable and also for sharing his insights in neutrino physics and statistics. I am especially grateful to Evgeny Akhmedov, who was patient with my questions and always provided illuminating answers to them. Jose Valle I would like to thank for inviting me to Valencia and for stipulating my interest in physics beyond neutrino oscillation. Furthermore I acknowledge the financial support of the Max-Planck-Institut für Physik.

Specifically concerning this work, I have to thank Jörn Kersten for proof reading and pinning down the errors in my English. The remaining errors, of which I am certain that they exist, are entirely my responsibility. Also Thomas Schwetz and Walter Winter deserve a special thanks for the additional proof reading of parts of this work.

The atmosphere in our group was always very comfortable and for this I thank all my colleagues in Munich: Stefan Antusch, Florian Bauer, Michael Ratz, Gerhart Seidl and also our newcomers Marc-Thomas Eisele, Markus Michael Müller and Mark Rolinec. Also the people providing the infrastructure should not be forgotten: Karin Ramm, our brave secretary who fought many battles with the administration, and the staff of the CIP-pool who kept the computers running.

Last but certainly not least I thank my wife Angelika for her enduring support and patience.

Appendix A

Experiment simulation

A.1 Simulation of the detector response

A neutrino detector is a very complex system composed of many different parts and its performance is computed by means of a Monte-Carlo simulation. Typically these simulation programs include a detailed description of the geometry, materials, electronics *a.s.f.* and the propagation of each particle through all the various parts is followed step by step from the primary interaction vertex till the reconstructed event. This procedure is repeated for a large number of particles and on the basis of this sample it is possible to determine properties of the detector like efficiencies, energy resolution *etc.*. These Monte-Carlo programs are however very slow and can therefore not be used for the type of analysis presented in this work. An alternative to the use of a full detector simulation is to regard a detector as an abstract entity, which maps the incident neutrino flux to the reconstructed neutrino flux. In general the properties of the mapping function can be derived from the results of a full detector simulation. In this work these properties are not reconstructed from the full Monte-Carlo results since these results are not publicly available. Instead they are retrieved from the information given in the corresponding references, where summaries of the full simulation are presented. However it turns out that the available information is sufficient to accurately reproduce the published results for each setup.

The detector as abstract function

The mapping function used in this work takes into account the most important interaction modes of all neutrino flavours, the energy response of the detector and the corresponding efficiencies. The basic interaction types (IT) for the long baseline setups (*i.e.* NuMI, JHF-SK, JHF-HK and NuFact-II) are: neutral current (NC), total charged current (CC) and quasi–elastic (QE). The corresponding total cross sections are shown in figure A.1 and taken from [130]. Errors on the cross sections are not taken into account, although the current knowledge is not very accurate. For all long baseline experiments subject to this work it is implicitly assumed that there will be a near detector experiment which will determine the relevant cross sections precisely. From figure A.1 it is obvious that the relative contribution of each IT varies with the energy of the neutrino, *e.g.* QE events play a major role only for energies well below 10 GeV. For the reactor experiments Reactor-I and Reactor-II the only relevant IT is in-

Interaction types – IT

verse β-decay and the cross section for this reaction is approximately given by

$$\sigma(E_{e^+}) \simeq \frac{2\pi^2\hbar^3}{m_e^5 f \tau_n} p_{e^+} E_{e^+} \,, \tag{A.1}$$

where τ_n is the lifetime of a free neutron and f is the free neutron decay phase space. In the numerical calculation the cross section from [131] is used, which includes higher order corrections.

Calculation of raw event rates

For the calculation of event rates, the first step is to compute the number of events for each IT in the fiducial mass of the detector for each neutrino flavour and energy bin. The second step is to include the detector effects like energy resolution or the misidentification of particles. The combination of those steps yields the differential event rate spectrum for each flavour and IT as seen by the detector. This spectrum is called a "channel". The channels for all ITs then are assembled into pairs of signal and background, each such pair is called a "rule"[1]. In the construction of each rule the fact that certain ITs cannot be completely separated either due to physical reasons (*e.g.* the flavour–blindness of NC interactions) or because of detector effects (*e.g.* charge misidentification) is taken into account. In one experiment there can be several rules, *i.e.* pairs of signal and background, for example the ν_μ events of the disappearance transition and the ν_e events of the appearance transition in a superbeam experiment constitute the signals of two different rules.

Channels & rules

The master formula for the computation of the differential event rate for each channel, *i.e.*, the final flavour f and the interaction type IT, is given by

Differential event rate

$$\begin{aligned}\frac{dn_f^{\mathrm{IT}}}{dE'} = \quad & N \sum_{f_i} \int\int dE\, d\hat{E} \quad \underbrace{\Phi_{f_i}(E)}_{\text{Production}} \times \\ & \underbrace{\frac{1}{L^2} P_{\nu_{f_i}\to\nu_f}(E, L, \rho; \theta_{23}, \theta_{12}, \theta_{13}, \Delta m^2_{31}, \Delta m^2_{21}, \delta_{\mathrm{CP}})}_{\text{Propagation}} \times \\ & \underbrace{\sigma_f^{\mathrm{IT}}(E) k_f^{\mathrm{IT}}(E, \hat{E})}_{\text{Interaction}} \times \\ & \underbrace{T_f(\hat{E}) V_f(\hat{E}, E')}_{\text{Detection}} \,,\end{aligned} \tag{A.2}$$

where f_i is the initial flavour of the neutrino, E is the incident neutrino energy, $\Phi_{f_i}(E)$ is the flux of the initial flavour at the source, L is the baseline length, N is a normalization factor, and ρ is the matter density. The interaction term is composed of two factors, which are the total cross section $\sigma_f^{\mathrm{IT}}(E)$ for the flavour f and the interaction type IT, and the energy distribution of the secondary

[1] The term rule is used because in the actual software a set of rules has to be defined in order to implement a pair of signal and background.

particle[2] $k_f^{\mathrm{IT}}(E, \hat{E})$ with $\hat{E}$ being the visible energy of the secondary particle. The detector properties are modeled by the threshold function $T_f(\hat{E})$, coming from the limited resolution or the cuts in the analysis, and the energy resolution function $V_f(\hat{E}, E')$ for the secondary particle. Thus, E' is the *reconstructed* neutrino energy.

Splitting the integrations

Since it is rather cumbersome to numerically solve this double integral, the integral is split into pieces and the integral over $\hat{E}$ is evaluated first. The only terms containing $\hat{E}$ are $k_f^{\mathrm{IT}}(E, \hat{E})$, $T_f(\hat{E})$, and $V_f(\hat{E}, E')$, and the following definition can be made

$$R_f^{\mathrm{IT}}(E, E')\, \epsilon_f^{\mathrm{IT}}(E') \equiv \int d\hat{E} \quad T_f(\hat{E})\, k_f^{\mathrm{IT}}(E, \hat{E})\, V_f(\hat{E}, E')\,. \tag{A.3}$$

The integrand for the integration with respect to $\hat{E}$ does not depend on any oscillation parameter and needs therefore to be evaluated only once for each experiment. Furthermore the approximation of R_f^{IT} by the following analytical expression is used

$$R_f^{\mathrm{IT}}(E, E') = \frac{1}{\sigma_E \sqrt{2\pi}} \exp \frac{(E - E')^2}{2\sigma_E^2}. \tag{A.4}$$

The values for the effective relative energy resolution σ_E and the effective efficiency ϵ_f^{IT} are in general energy dependent and can be found in appendix A.2 for each setup. The reason for using this approximation is that the full energy transfer function as derived by a full detector simulation is not publicly available.

The final step in the event rate calculation is the integration of equation A.2 with respect to E' in order to obtain the number of events n_i in each bin i

$$n_i = \int_{E_i^l}^{E_i^u} dE' \quad \frac{dn_f^{\mathrm{IT}}}{dE'}\,, \tag{A.5}$$

where E_i^l denotes the lower bin boundary and E_i^u the upper bin boundary. The only part in equation A.2 which depends on E' is $R_f^{\mathrm{IT}}(E, E')\, \epsilon_f^{\mathrm{IT}}(E')$ and therefore the integration with respect to E' can be computed immediately and the result is the convolution kernel $K_i(E)$ for each bin i

$$K_i(E) = \int_{E_i^l}^{E_i^u} dE' \quad R_f^{\mathrm{IT}}(E, E')\, \epsilon_f^{\mathrm{IT}}(E')\,. \tag{A.6}$$

Reassembling the various parts, the final expression for the calculation of the number of events in the i-th bin is given by

$$n_i = N \sum_{f_i} \int dE \quad \Phi_{f_i}(E) \times \frac{1}{L^2} P_{\nu_{f_i} \to \nu_f}(E, L, \boldsymbol{\lambda}) \times \sigma_f^{\mathrm{IT}}(E) \times K_i(E)\,, \tag{A.7}$$

[2] In cases with several secondary particles, k_f is the average of the distribution functions for each type of secondary particle weighted with the corresponding branching ratio.

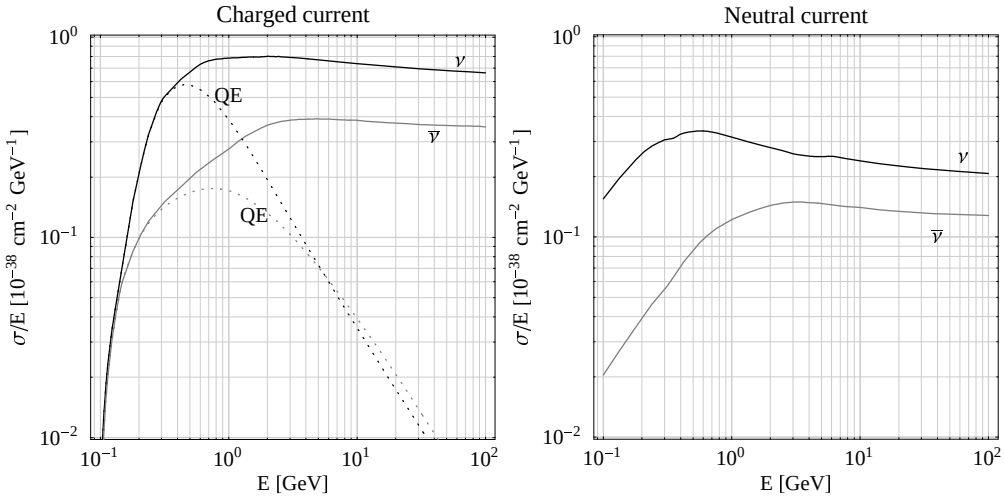

Figure A.1: *The cross sections for the total charged current* (*solid curves, left hand plot*)*, quasi–elastic charged current* (*dotted curves, left hand plot*)*, and neutral current* (*right hand plot*) *neutrino* (*black curves*) *and anti-neutrino* (*gray curves*) *interactions* [130]*. This figure is taken from* [80].

Only one integration remains

where $\boldsymbol{\lambda}$ denotes the oscillation parameters. By decomposing the various integrals the triple integral[3] for the calculation of the number of events in one bin has been reduced to a simple integration with respect to the true neutrino energy E. This reduction of the dimension from three to one is crucial for the numerical efficiency of the code and improves the speed by roughly three orders of magnitude.

A.2 Experiment description

A.2.1 The reactor experiment

The detector technology for a reactor neutrino experiment is very similar to that of Chooz [65], Kamland [5] and the Borexino counting test facility [132]. All these detectors use a liquid scintillator, which is based on mineral oil. The scintillator is contained in a plastic balloon and viewed by a large number of photomultipliers. In between the balloon and the photomultipliers a buffer liquid is needed in order to shield the fiducial inner volume from the radioactivity of the photomultipliers. The signature of a $\bar{\nu}_e$ event is the delayed coincidence of the prompt γ-rays due to the annihilation of the positron and the γ-rays emitted in the neutron capture. The neutrino energy is uniquely determined by the visible energy E_{vis} via the relation

$$E_{\bar{\nu}_e} = E_{\text{vis}} - 511\,\text{keV} + (m_n - m_p) + \mathcal{O}(E_{\bar{\nu}_e}/m_n)\,, \tag{A.8}$$

[3] *i.e.* the two integrations in equation A.2 plus the integration in equation A.5

where the 511 keV have to be subtracted in order to account for the rest mass of the electron which is co-annihilated with the positron. The typical energy resolution is roughly $(5-10)\%/\sqrt{E_{\text{vis}}}$ [5,133] and a value of $\sigma_E = 5\%/\sqrt{E_{\text{vis}}}$ is used. The results do not change for a value of $7.5\%/\sqrt{E_{\text{vis}}}$, the value obtained in the KamLAND experiment. The visible energy range used for the analysis is $(1-7.2)$ MeV and divided into 62 bins. The normalization is the same as in [133] and such that at a distance of 1 km 227.5 events are observed in one fiducial ton of detector within one year at a reactor with a thermal power of 1 GW. The efficiency is taken to be unity and constant. The deviations from 1 should be at most of the order of a few percent. Furthermore no backgrounds are considered for two reasons: First, it would require a detailed background computation for a specific site. Second and more important, it should be possible to build an essentially background free detector [133]. For a more detailed description of the experiment appendix B of [94] can be consulted. The near detector is assumed to be identical to the far detector and to be located so close that no oscillation has developed.

For the neutrino flux from the reactor the parameterization of [134] is used and the fuel composition of [5] is adopted.

A.2.2 The NuMI experiment

The detector of the NuMI experiment will be a low-Z calorimeter[4] in order to obtain a measurement of the hadronic energy deposition and to separate ν_e CC events from NC events. The low mass number of the absorber material ensures that the hadronic shower has a sufficient size in order to be reliably detected. The detector is described in detail in [88]. The energy resolution is expected to be very similar to the one of MINOS [135] and therefore $\sigma_E = 0.15 \cdot E_\nu$ is used. The analysis range is $(1.6 - 2.8)$ GeV and divided into 20 bins. The signal consists of the ν_e CC events from the appearance transition and the ν_μ CC events from the surviving ν_μ. The backgrounds to the appearance measurement are the misidentified NC events and the ν_e CC events due to the contamination of the beam with ν_e. The only background which is considered for the disappearance measurement is the fraction of NC events which is identified as ν_μ CC event. The efficiencies and rejection factors are taken from [88] as far as they have been provided in this work, whereas the missing information was obtained from [136]. The efficiencies are given in table A.1.

The beam flux is taken from [137] and has been provided as data files by [136].

A.2.3 The JHF experiment

The detector for the JHF experiment is the Super-K (JHF-SK) detector or its 1 000 kt version Hyper-K (JHF-HK). It is assumed that the 1 000 kt detector has the same characteristics as the Super-K detector. This type of water Cherenkov detector has an excellent capability to identify electrons and muons based on

[4] Other detector technologies like a liquid Argon TPC are also under consideration.

Disappearance	
Signal	$0.9 \otimes (\nu_\mu \to \nu_\mu)_{\text{CC}}$
Background	$0.005 \otimes (\nu_\mu \to \nu_x)_{\text{NC}}$
Appearance	
Signal	$0.4 \otimes (\nu_\mu \to \nu_e)_{\text{CC}}$
Background	$0.005 \otimes (\nu_\mu \to \nu_x)_{\text{CC}}$
Beam background	$0.4 \otimes (\nu_e \to \nu_e)_{\text{CC}}$ $0.4 \otimes (\bar{\nu}_e \to \bar{\nu}_e)_{\text{CC}}$

Table A.1: *The efficiencies for the signals and backgrounds of the* NuMI *experiment. This table is taken from* [95].

the topology of the Cherenkov ring. Furthermore, the lepton momentum can be measured with a high precision [87].

The signal events for the neutrino beam are given by ν_μ and ν_e CC interactions, whereas the backgrounds are given by the ν_μ NC events and the ν_e CC events coming from the ν_e contained in the beam. Furthermore the misidentification of ν_μ events as ν_e event acts as an additional background to the appearance measurement. The background rejection factors and the signal efficiencies are taken from table 2 in [87]. They are assumed to be constant, which should be a reasonable approximation.

Disappearance	
Signal	$0.9 \otimes (\nu_\mu \to \nu_\mu)_{\text{QE}}$
Background	$0.0056 \otimes (\nu_\mu \to \nu_x)_{\text{NC}}$
Appearance	
Signal	$0.505 \otimes (\nu_\mu \to \nu_e)_{\text{CC}}$
Background	$0.0056 \otimes (\nu_\mu \to \nu_x)_{\text{NC}}$ $3.3 \cdot 10^{-4} \otimes (\nu_\mu \to \nu_\mu)_{\text{cc}}$
Beam background	$0.505 \otimes (\nu_e \to \nu_e)_{\text{CC}}$ $0.505 \otimes (\bar{\nu}_e \to \bar{\nu}_e)_{\text{CC}}$

Table A.2: *The efficiencies for the signals and backgrounds of the* JHF-SK *and* JHF-HK *experiments. This table is taken from* [80].

Since a water Cherenkov detector cannot measure the hadronic energy deposition in a neutrino interaction, the analysis of the energy spectrum has to be constrained to the QE event sample. The accuracy of the energy reconstruction is limited by the Fermi-motion of the nucleons, inducing a width of about $(80 - 100)\,\text{MeV}$ [138]. The distribution is, up to very good accuracy, Gaußian [138]. The Fermi-motion is energy independent and causes by far the largest error in the energy reconstruction. A constant width of 85 MeV is used in this work *i.e.*, $\sigma_E = 0.085\,\text{GeV}$.

In order to use the spectral information, the signal event samples are separated into QE events and non-QE events. In the disappearance channel, there

are enough events to completely discard the non-QE events, as it is done in [87]. For the appearance channel, the following strategy is adopted to optimally exploit the information in the data: the total number of all CC events in the range $0.4 - 1.2\,\mathrm{GeV}$ is used, as well as the QE spectrum in the same energy range divided into 20 bins with a free normalization in order to avoid a double counting of the QE events. This separation of rates and spectra is a well-known technique, which is used *e.g.* in the solar analysis of Super-K data in [139].

Separation of rates and spectrum

The beam fluxes used are the same as in [87] and have been provided as data files by [138].

A.2.4 The neutrino factory experiment

The detector which is considered to be optimal for a neutrino factory is a magnetized iron calorimeter, similar to the Minos [135] or Monolith [140] detectors. This detector type measures the leptonic as well as the hadronic energy deposition, albeit with a different resolution. NC events can be very well rejected due to the absence of the long muon track. The magnetic field is necessary to improve the lepton momentum measurement and to determine the charge. The energy resolution of this type of detector is very well approximated by a Gaußian with the width $\sigma_E = 0.15 \cdot E_\nu$, which is very similar to the resolution of Minos [135]. This approximation is justified in detail in the appendices of [80]. The spectrum is evaluated in the analysis range from 4 GeV to 50 GeV and is divided into 20 bins.

The requirement of a very precise charge determination in order to obtain a clean wrong sign muon sample imposes the need for a cut on the minimum muon momentum and the minimum missing transversal momentum [110, 141]. The values for these cuts in turn determine the background levels and the low energy efficiencies, which have some relevance to the issue of the confidence level at which certain multiple solutions appear in the fit. The muon momentum cut here is 4 GeV. This value yields an efficiency for ν_μ linearly rising from 0 at 4 GeV to 0.45 at 20 GeV and staying constant from there on, whereas for $\bar{\nu}_\mu$ the efficiency rises linearly from 0 at 4 GeV to 0.35 at 20 GeV. This roughly corresponds to an interpolation between the values given in [110, 141] and is approximately the same as in [89]. The corresponding background levels are given in table A.3. A very detailed discussion of this issue is given in the appendices of [80].

The signal at a neutrino factory consists of the ν_μ disappearance and the wrong-sign muon appearance signal. The backgrounds for the disappearance measurement are a certain fraction of the NC events. In the appearance transition there is additionally a fraction of misidentified right sign muon events. The values used in this work are shown in table A.3.

Disappearance – μ^- stored	
Signal	$0.45 \otimes (\nu_\mu \to \nu_\mu)_{\mathrm{CC}}$
Background	$10^{-5} \otimes (\nu_\mu \to \nu_x)_{\mathrm{NC}}$
Disappearance – μ^+ stored	
Signal	$0.35 \otimes (\bar{\nu}_\mu \to \bar{\nu}_\mu)_{\mathrm{CC}}$
Background	$10^{-5} \otimes (\bar{\nu}_\mu \to \bar{\nu}_x)_{\mathrm{NC}}$
Appearance – μ^- stored	
Signal	$0.45 \otimes (\bar{\nu}_e \to \bar{\nu}_\mu)_{\mathrm{CC}}$
Background	$5 \cdot 10^{-6} \otimes (\nu_\mu \to \nu_x)_{\mathrm{NC}}$ $5 \cdot 10^{-6} \otimes (\nu_\mu \to \nu_\mu)_{\mathrm{CC}}$
Appearance – μ^+ stored	
Signal	$0.35 \otimes (\nu_e \to \nu_\mu)_{\mathrm{CC}}$
Background	$5 \cdot 10^{-6} \otimes (\bar{\nu}_\mu \to \bar{\nu}_x)_{\mathrm{NC}}$ $5 \cdot 10^{-6} \otimes (\bar{\nu}_\mu \to \bar{\nu}_\mu)_{\mathrm{CC}}$

Table A.3: *The high energy efficiencies for the signals and backgrounds for* NuFact-II. *This table is taken from* [80].

Appendix B

Statistics and the treatment of systematical errors

In this appendix the statistical analysis methods and the parameterizations of the various systematical uncertainties are explained. The statistical analysis is divided into two parts. The first one deals with the systematical errors, whereas the second one deals with the retrieval of the oscillation parameters. The reason for this division is that the first part does not require the recalculation of event rates and therefore is numerically much faster to solve separately. For the analysis of the systematical errors the so called pull method is used [41][1]. In the pull method k systematical errors are included by introducing k additional variables ζ_k, which will be called nuisance parameters in the following. The nuisance parameters describe the dependence of the event rates on the various sources of systematical errors, *e.g.* an error on the total normalization is included by multiplying the expected number of events in each bin by a factor $(1 + \zeta_1)$. The variation of ζ_1 in the fit is constrained by adding a penalty p_1 to the χ^2-function. In case of a Gaußian distributed systematical error this penalty is given by

The pull method – nuisance parameters

$$p_i = \frac{(\zeta_i - \zeta_i^0)^2}{\sigma_{\zeta_i}^2}\,, \tag{B.1}$$

where ζ_i^0 denotes the mean and σ_{ζ_i} the standard deviation of the corresponding nuisance parameter, *i.e.* the amount of systematical uncertainty. The resulting χ^2 is then minimized with respect to all nuisance parameters ζ_i and this yields χ^2_{pull}

$$\chi^2_{\text{pull}}(\boldsymbol{\lambda}) := \min_{\{\zeta_i\}} \left(\chi^2(\boldsymbol{\lambda}, \zeta_1, \ldots, \zeta_k) + \sum_{j=1}^{k} p_j(\zeta_j) \right)\,, \tag{B.2}$$

where $\boldsymbol{\lambda}$ denotes the oscillation parameters including the matter density ρ. One advantage of the pull method is that whenever the number N of data points is much larger than k, it is numerically easier to compute χ^2_{pull} than to invert the $N \times N$ covariance matrix. For the experiments considered here N is typically 20 and $k \sim 4$, thus the pull method is numerically much faster. Moreover it is more

[1] In fact the pull method was employed already in [80] before [41] appeared.

flexible and allows the inclusion of systematical errors also for a Poissonian χ^2-function. In [41] it was shown that the pull method and the covariance based approach are equivalent for a Gaußian and linear model. In general there is a separate $(\chi^2_{\text{pull}})^\alpha$ for each rule α, *i.e.* pair of signal and background spectra, with a separate set of nuisance parameters ζ_i^α. In this case χ^2_{pull} is the sum of all individual $(\chi^2_{\text{pull}})^\alpha$.

In this way the dependence on the k nuisance parameters has been eliminated from χ^2_{pull} and only the dependence on the physical parameters $\boldsymbol{\lambda}$ remains. Usually only one of the parameters λ_i is of interest, which is denoted by η. The set of remaining physical parameters is denoted by $\bar{\boldsymbol{\lambda}}$. Furthermore the experiment may have no reasonable accuracy for a certain number I of other parameters $\{\lambda_j\}$, this set of insufficiently measured parameters[2] is called $\boldsymbol{\kappa}$. For the parameters $\boldsymbol{\kappa}$ external input from other experiments is included in order to improve the overall performance of the experiment. The external information is again taken into account by adding a penalty π_j for each of the κ_j but in this case to χ^2_{pull}. The form of the π_j is in the Gaußian case given again by equation B.1. The sum of χ^2_{pull} and the penalties π_j is then minimized with respect to the set of the remaining physical parameters $\bar{\boldsymbol{\lambda}}$. This yields the projected χ^2_η

Insufficiently determined parameters – external input

$$\chi^2_\eta(\eta|\boldsymbol{\lambda}_0) = \min_{\bar{\boldsymbol{\lambda}}} \left(\chi^2_{\text{pull}}(\eta, \bar{\boldsymbol{\lambda}}) + \sum_{i=1}^{I} \pi_i(\kappa_i) \right) . \tag{B.3}$$

$\chi^2_\eta(\eta|\boldsymbol{\lambda}_0)$ is now only a function of η and has to be interpreted with one degree of freedom, thus the confidence level in units of σ is given by $\sqrt{\chi^2_\eta}$. Of course $\chi^2_\eta(\eta|\boldsymbol{\lambda}_0)$ retains a dependence on the values of the true parameters $\boldsymbol{\lambda}_0$, which will be dropped in the notation for convenience. In the case that several experiments are combined the sum of the unprojected $\chi^2_{\text{pull}}(\eta, \bar{\boldsymbol{\lambda}})$ for each experiment is added to the sum of all the π_i and the minimization with respect to $\bar{\boldsymbol{\lambda}}$ is performed for the complete sum[3]. The definition of χ^2_η in equation B.3 already implies the inclusion of the degenerate solutions created by the transformation $\mathcal{T}_i$ (as defined in equation 3.9), *i.e.* the fit runs over all values of Δm^2_{31}, including both normal and inverted mass hierarchy. It also runs over all values of θ_{23}, *i.e.* the case $\pi/2 - \theta_{23}$ is included.

Degeneracies included

$\sin^2 2\theta_{13}$

Specifically some exact definitions of sensitivities and errors are made in accordance with the discussion in section 3.7. For the sensitivity limit to $\sin^2 2\theta_{13}$ this quantity is useful

$$\chi^2_{\text{L}}(\theta_{13}) := \chi^2_{\theta_{13}}(\theta_{13}|(\theta_{13})_0 = 0) . \tag{B.4}$$

The sensitivity limit as defined in section 3.7 in terms of χ^2_{L} is given by the largest value of $\sin^2 2\theta_{13}$ where $\chi^2_{\text{L}}(\theta_{13})$ is below the threshold for the given confidence level, *e.g.* for a $2\,\sigma$ limit this threshold is 4.

[2] This set can in principle contain η. In this case the projected χ^2 of η is dominated by the external input π_η.

[3] *i.e.* the external information is counted only once

The sensitivity to the mass hierarchy is defined by the value of the global minimum of $\chi^2_{\theta_{13}}$ with the opposite sign of Δm^2_{31}, *i.e.* Δm^2_{31} is restricted to the half-space where the fitted Δm^2_{31} has the opposite sign than the true value of Δm^2_{31}. Thus for the true Δm^2_{31} being larger than 0, the sensitivity is given by

The mass hierarchy

$$\chi^2_{\mathrm{H}} := \min_{\eta, \Delta m^2_{31} < 0} \chi^2_{\eta}(\eta | (\Delta m^2_{31})_0 > 0)\,. \tag{B.5}$$

Finally the sensitivity to any CP-violation is defined by the minimum χ^2 separation of the true value of the CP-phase δ_0 from any of the CP-conserving values of the CP-phase, π and 0

CP-violation

$$\chi^2_{\mathrm{CP}}(\delta_0) := \min\left\{\chi^2_{\delta}(0|\delta_0), \chi^2_{\delta}(\pi|\delta_0)\right\}\,. \tag{B.6}$$

The sensitivity to maximal CP-violation is the special case where $\delta_0 = \pm\pi/2$, *i.e.* $\chi^2_{\mathrm{CP}}(\pm\pi/2)$.

Definition of χ^2 for the long baseline setups

For the long baseline setups the set $\boldsymbol{\lambda}$ consists of $\Delta m^2_{21} \cdot \sin 2\theta_{12}$, Δm^2_{31}, θ_{23}, θ_{13}, δ_{CP} and ρ. The product $\Delta m^2_{21} \cdot \sin 2\theta_{12}$ is called π_{sol} and is used because the transition probability in equation 3.1 depends on the solar parameters only via this product. This is the only approximation introduced for the treatment of the oscillation probabilities. The insufficiently determined parameters $\boldsymbol{\kappa}$ are the matter density ρ and the solar product π_{sol}. The external input for ρ is assumed to come from geophysics and to constrain the matter density to within 5% at $1\,\sigma$ [113]. The solar product will be well constrained by Kamland data and the expected final accuracy after three years of data taking will be 15% for the solar product π_{sol}, again at $1\,\sigma$ [97, 112].

As basis for the analysis of the long baseline setups, the standard χ^2-function for Poissonian distributed quantities, as given for example in [70], is used

Poissonian χ^2

$$\chi^2 \;=\; \sum_{i=1}^{b} \left(2[\langle x_i \rangle - x_i] + 2\, x_i \log \frac{x_i}{\langle x_i \rangle} \right). \tag{B.7}$$

Here, b is the number of bins, x_i is the number of events in the ith bin, and $\langle x_i \rangle$ is the expectation value of the number of events in the ith bin. For each bin i, the total number of events is the sum of signal and background events, *i.e.*,

$$x_i = s_i + b_i, \tag{B.8}$$

where s_i is the number of signal events and b_i is the number of background events, as defined in the previous appendix. The systematical errors in x_i and b_i are included by modifying the signal s^0_i and background b^0_i raw event rates of the previous appendix by

Normalization & tilt

$$\begin{aligned} s_i &= s_i(\zeta_1, \zeta_2) = s^0_i \left(1 + \zeta_1 + \zeta_2 \cdot E_i/(E_{\max} - E_{\min})\right), \\ b_i &= b_i(\zeta_3, \zeta_4) = b^0_i \left(1 + \zeta_3 + \zeta_4 \cdot E_i/(E_{\max} - E_{\min})\right), \end{aligned} \tag{B.9}$$

where E_i is the average energy in the ith bin, $E_{\max}$ is the maximum energy, and $E_{\min}$ is the minimum energy of all bins. The nuisance parameters ζ_1 and

ζ_3 are called "normalization" and describe the effect of an overall change in the magnitude of signal or background, whereas the parameters ζ_2 and ζ_4 are called "tilt" and describe a linear distortion in the spectral shape of the signal or background. This distortion can come from limited knowledge of the background or an energy calibration error. This way of parameterizing an energy calibration error was for example used in the analysis of the Bugey data [63]. The total number of events in the ith bin x_i now becomes

$$x_i = x_i(\zeta) = s_i(\zeta_1, \zeta_2) + b_i(\zeta_3, \zeta_4). \tag{B.10}$$

Note that ζ_1 to ζ_4 are independent parameters and there is a different set of these four parameters for each rule α. In order to implement the uncertainties of the nuisance parameters, the values of ζ_1 to ζ_4 are assumed to follow a Gaußian distribution with mean 0 and a standard deviation of σ_{ζ_i}. The values of σ_{ζ_i} for each long baseline experiment and rule are given in table B.1.

	σ_{ζ_1}	σ_{ζ_2}	σ_{ζ_3}	σ_{ζ_4}
Disappearance – NuMI	0.05	0.05	0.05	0.05
Appearance – NuMI	0.05	0.05	0.05	0.05
Disappearance – JHF	0.05	0.025	0.2	0.025
Appearance – JHF	0.05	0.025	0.05	0.05
Disappearance – NuFact-II	0.01	0.05	0.05	0.05
Appearance – NuFact-II	0.01	0.05	0.2	0.05

Table B.1: *Systematical uncertainties for the long baseline setups from* [110,140,142, 143] *for* NuFact-II*, from* [87, 144–147] *for the* JHF *experiments and from* [88, 136] *for the* NuMI *setup.*

Definition of χ^2 for the reactor setups

For the reactor setups the set $\boldsymbol{\lambda}$ consists of Δm^2_{21}, $\sin 2\theta_{12}$, Δm^2_{31} and θ_{13}, since the disappearance probability $P_{\bar{\nu}_e \to \bar{\nu}_e}$ in equation 4.3 does not depend on any other parameter. The insufficiently determined parameters $\boldsymbol{\kappa}$ are the solar parameters Δm^2_{21} and θ_{12} and the atmospheric mass splitting Δm^2_{31}. The external input for the solar parameters is assumed to come from the Kamland data and the expected final accuracy after three years of data taking will be better than 10% for each of the solar parameters [97, 112]. The results do not depend strongly on this number and therefore a conservative value of 10% is used. The external input on Δm^2_{31} will be due to *e.g.* the Minos experiment and the error is assumed to be 10% at $1\,\sigma$.

The starting point for the analysis of the reactor setups is the usual Gaußian χ^2 (see *e.g.* [70])

Gaußian χ^2

$$\chi^2 \;=\; \sum_{i=1}^{b} \frac{(\langle x_i \rangle - x_i)^2}{x_i}\,. \tag{B.11}$$

A Gaußian χ^2 can be used since the number of events in each bin is very large. The systematical errors are parameterized in the following way

$$x_i = (1 + \zeta_1)s_i^0 + \zeta_2 M_i \,, \tag{B.12}$$

where ζ_1 describes the relative normalization and ζ_2 the energy calibration error. An energy calibration error shifts the visible energy from E_{vis} to $(1 + \zeta_2)E_{\text{vis}}$, this can be expressed up to first order in ζ_2 by

Relative normalization & energy calibration

$$x_i(\zeta_2) \simeq x_i(\zeta_2 = 0) + \zeta_2 M_i \text{ with } M_i = \left.\frac{\partial x_i}{\partial \zeta_2}\right|_{\zeta_2=0} . \tag{B.13}$$

The relative normalization error σ_{ζ_1} is given by

$$\sigma_{\zeta_1}^{-2} = (\sigma_{\zeta_1}^{\text{source}})^{-2} + (\sigma_{\zeta_1}^{\text{detector}})^{-2} \,, \tag{B.14}$$

where $\sigma_{\zeta_1}^{\text{source}}$ and $\sigma_{\zeta_1}^{\text{detector}}$ describe the individual contributions of the normalization uncertainty of the source and of the two detectors. The conditions for which this relation holds are given in appendix A of [94]. The values for σ_{ζ_1} and σ_{ζ_2} are given in table B.2.

	σ_{ζ_1}	σ_{ζ_2}
Disappearance – Reactor	0.008	0.005

Table B.2: *Systematical uncertainties for the reactor setups from* [65, 148].

Numerical issues

For all the necessary function minimizations a fast "direction set" method is used. The algorithm and its implementation in C are taken from [149]. The advantages of using this minimization algorithm are its high speed and its excellent accuracy compared to grid–based methods. Furthermore, it does not require the computation of derivatives of the function to be minimized, which is rather important because derivatives of numerical functions can be unstable and are quite slow to be computed. All numerical calculations are performed with `double` precision, *i.e.* 32-bit numbers.

List of figures

Bibliography

[1] Kamiokande-II, K. Hirata et al., *Observation of a neutrino burst from the supernova* SN1987A, Phys. Rev. Lett. **58** (1987), 1490–1493.

R. M. Bionta et al., *Observation of a neutrino burst in coincidence with supernova* SN1987A *in the large Magellanic cloud*, Phys. Rev. Lett. **58** (1987), 1494.

[2] G. G. Raffelt, *Particle physics from stars*, Ann. Rev. Nucl. Part. Sci. **49** (1999), 163–216, `hep-ph/9903472`.

[3] Super-K, Y. Fukuda et al., *Evidence for oscillation of atmospheric neutrinos*, Phys. Rev. Lett. **81** (1998), 1562–1567, `hep-ex/9807003`.

[4] SNO, Q. R. Ahmad et al., *Direct evidence for neutrino flavor transformation from neutral-current interactions in the Sudbury Neutrino Observatory*, Phys. Rev. Lett. **89** (2002), 011301, `nucl-ex/0204008`.

[5] Kamland, K. Eguchi et al., *First results from* Kamland*: Evidence for reactor anti-neutrino disappearance*, Phys. Rev. Lett. **90** (2003), 021802, `hep-ex/0212021`.

[6] K2K, M. H. Ahn et al., *Indications of neutrino oscillation in a* 250 km *long-baseline experiment*, Phys. Rev. Lett. **90** (2003), 041801, `hep-ex/0212007`.

[7] M. C. Gonzalez-Garcia and Y. Nir, *Developments in neutrino physics*, Rev. Mod. Phys. **75** (2003), 345–402, `hep-ph/0202058`.

[8] A. D. Dolgov, *Neutrinos in cosmology*, Phys. Rept. **370** (2002), 333–535, `hep-ph/0202122`.

[9] E. L. Wright, *The* WMAP *data and results*, (2003), `astro-ph/0306132`.

[10] The 2dFGRS Team, W. J. Percival et al., *Parameter constraints for flat cosmologies from* CMB *and* 2dFGRS *power spectra*, (2002), `astro-ph/0206256`.

[11] S. Hannestad, *Neutrino masses and the number of neutrino species from* WMAP *and* 2dFGRS, (2003), `astro-ph/0303076`.

[12] R. N. Mohapatra, ICTP *lectures on theoretical aspects of neutrino masses and mixings*, (2002), `hep-ph/0211252`.

M.-C. Chen and K. T. Mahanthappa, *Fermion masses and mixing and* CP*-violation in* $SO(10)$ *models with family symmetries*, (2003), `hep-ph/0305088`.

R. N. Mohapatra, *Understanding neutrino masses and mixings within the seesaw framework*, (2003), `hep-ph/0306016`.

J. C. Pati, *Probing grand unification through neutrino oscillations, leptogenesis, and proton decay*, Phys. Rept. **379** (2003), 69–148, `hep-ph/0305221`.

G. Altarelli and F. Feruglio, *Phenomenology of neutrino masses and mixings*, (2003), `hep-ph/0306265`.

[13] V. Barger, D. Marfatia, and K. Whisnant, *Progress in the physics of massive neutrinos*, (2003), `hep-ph/0308123`.

[14] P. Vogel, *Double beta decay: Theory, experiment, and implications*, Ann. Rev. Nucl. Part. Sci. **52** (2000), 115–151, `nucl-th/0005020`.

S. R. Elliott and P. Vogel, *Double beta decay*, Ann. Rev. Nucl. Part. Sci. **52** (2002), 115–151, `hep-ph/0202264`.

[15] S. M. Bilenky, C. Giunti, J. A. Grifols, and E. Masso, *Absolute values of neutrino masses: Status and prospects*, Phys. Rept. **379** (2003), 69–148, `hep-ph/0211462`.

[16] B. Pontecorvo, *Inverse beta processes and nonconservation of lepton charge*, Sov. Phys. JETP **7** (1958), 172–173.

[17] B. Pontecorvo, *Neutrino experiments and the question of leptonic-charge conservation*, Sov. Phys. JETP **26** (1968), 984–988.

V. N. Gribov and B. Pontecorvo, *Neutrino astronomy and lepton charge*, Phys. Lett. **B28** (1969), 493.

[18] Z. Maki, M. Nakagawa, and S. Sakata, *Remarks on the unified model of elementary particles*, Prog. Theor. Phys. **28** (1962), 870.

[19] M. Kobayashi and T. Maskawa, CP *violation in the renormalizable theory of weak interaction*, Prog. Theor. Phys. **49** (1973), 652–657.

[20] L. Wolfenstein, *Neutrino oscillations and stellar collapse*, Phys. Rev. **D20** (1979), 2634–2635.

S. P. Mikheev and A. Y. Smirnov, *Resonance enhancement of oscillations in matter and solar neutrino spectroscopy*, Sov. J. Nucl. Phys. **42** (1985), 913–917.

S. P. Mikheev and A. Y. Smirnov, *Resonant amplification of neutrino oscillations in matter and solar neutrino spectroscopy*, Nuovo Cim. **C9** (1986), 17–26.

[21] L. Wolfenstein, *Oscillations among three neutrino types and* CP *violation*, Phys. Rev. **D18** (1978), 958–960.

S. M. Bilenky, J. Hosek, and S. T. Petcov, *On oscillations of neutrinos with Dirac and Majorana masses*, Phys. Lett. **B94** (1980), 495.

J. Schechter and J. W. F. Valle, *Neutrino oscillation thought experiment*, Phys. Rev. **D23** (1981), 1666.

[22] B. Kayser, CPT, CP, *and* C *phases and their effects in Majorana particle processes*, Phys. Rev. **D30** (1984), 1023.

[23] J. Schechter and J. W. F. Valle, *Neutrino masses in* $SU(2)\times U(1)$ *theories*, Phys. Rev. **D22** (1980), 2227.

[24] L.-L. Chau and W.-Y. Keung, *Comments on the parametrization of the Kobayashi-Maskawa matrix*, Phys. Rev. Lett. **53** (1984), 1802.

C. Jarlskog, *A basis independent formulation of the connection between quark mass matrices,* CP *violation and experiment*, Z. Phys. **C29** (1985), 491–497.

C. Jarlskog, *Matrix representation of symmetries in flavor space, invariant functions of mass matrices and applications*, Phys. Rev. **D35** (1987), 1685.

[25] E. K. Akhmedov, P. Huber, M. Lindner, and T. Ohlsson, T *violation in neutrino oscillations in matter*, Nucl. Phys. **B608** (2001), 394–422, `hep-ph/0105029`.

[26] W. T. Kelvin, *On the age of the Sun's heat*, Macmillan's Magazine (1862), 288.

[27] H. v. Helmholtz, *On the interaction of natural forces*, Phil. Mag. **11** (1856), 489.

[28] F. W. Aston, *The mass-spectra of chemical elements*, Philosophical Magazine and Journal of Science **39** (1920), 611.

[29] C. F. v. Weizsäcker, *Über Elementumwandlungen im Inneren der Sterne II*, Physikalische Zeitschrift **39** (1938), 633.

H. A. Bethe, *Energy production in stars*, Phys. Rev. **55** (1939), 436.

[30] J. N. Bahcall, *How the Sun shines*, SLAC Beam Line **31N1** (2001), 2–12, `astro-ph/0009259`.

[31] J. Christensen-Dalsgaard, *Helioseismology*, Rev. Mod. Phys. **74** (2003), 1073–1129, `astro-ph/0207403`.

[32] J. Davis, Raymond, D. S. Harmer, and K. C. Hoffman, *Search for neutrinos from the Sun*, Phys. Rev. Lett. **20** (1968), 1205–1209.

[33] J. N. Bahcall, *Solar models: An historical overview*, AAPPS Bull. **12N4** (2002), 12–19, `astro-ph/0209080`.

[34] Kamiokande-II, K. S. Hirata et al., *Observation of ^8B solar neutrinos in the* Kamiokande-II *detector*, Phys. Rev. Lett. **63** (1989), 16.

[35] Sage, V. N. Gavrin et al., *First measurement of the integral solar neutrino flux by the Soviet-American Gallium experiment* (Sage), (1991), Given at 11th Moriond Workshop: Tests of Fundamental Laws in Physics, Les Arcs, France, 26 Jan - 2 Feb 1991.

[36] Gallex, P. Anselmann, Gallex *results from the first 30 solar neutrino runs*, (1994), Prepared for 29th Rencontres de Moriond: Electroweak Interactions and Unified Theories, Meribel les Allues, France, 12-19 Mar 1994.

[37] Super-K, M. B. Smy, *Solar neutrinos with* Super-Kamiokande, Phys. Rev. Lett. **65** (1999), 1297–1300, hep-ex/9903034.

[38] C.-S. Lim and W. J. Marciano, *Resonant spin-flavor precession of solar and supernova neutrinos*, Phys. Rev. **D37** (1988), 1368.

E. K. Akhmedov, *Resonant amplification of neutrino spin rotation in matter and the solar neutrino problem*, Phys. Lett. **B213** (1988), 64–68.

[39] L. Wolfenstein, *Neutrino oscillations in matter*, Phys. Rev. **D17** (1978), 2369.

E. Roulet, *Mikheyev-Smirnov-Wolfenstein effect with flavor-changing neutrino interactions*, Phys. Rev. **D44** (1991), 935–938.

M. M. Guzzo, A. Masiero, and S. T. Petcov, *On the* MSW *effect with massless neutrinos and no mixing in the vacuum*, Phys. Lett. **B260** (1991), 154–160.

[40] A. Y. Smirnov, *Solar neutrinos: Interpretation of results*, Phys. Lett. **B555** (2002), 144–146, hep-ph/0209131.

[41] G. L. Fogli, E. Lisi, A. Marrone, D. Montanino, and A. Palazzo, *Getting the most from the statistical analysis of solar neutrino oscillations*, Phys. Rev. **D66** (2002), 053010, hep-ph/0206162.

[42] J. Bahcall, *John Bahcall's homepage*, http://www.sns.ias.edu/~jnb/.

[43] V. Barger and D. Marfatia, Kamland *and solar neutrino data eliminate the* LOW *solution*, Phys. Lett. **B555** (2003), 144–146, hep-ph/0212126.

G. L. Fogli et al., *Solar neutrino oscillation parameters after first* Kamland *results*, Phys. Rev. **D67** (2003), 073002, hep-ph/0212127.

M. Maltoni, T. Schwetz, and J. W. F. Valle, *Combining first* Kamland *results with solar neutrino data*, Phys. Rev. **D67** (2003), 093003, hep-ph/0212129.

A. Bandyopadhyay, S. Choubey, R. Gandhi, S. Goswami, and D. P. Roy, *The solar neutrino problem after the first results from* Kamland, Phys. Lett. **B559** (2003), 121–130, hep-ph/0212146.

J. N. Bahcall, M. C. Gonzalez-Garcia, and C. Peña-Garay, *Solar neutrinos before and after* Kamland, JHEP **02** (2003), 009, hep-ph/0212147.

H. Nunokawa, W. J. C. Teves, and R. Zukanovich Funchal, *Determining the oscillation parameters by solar neutrinos and* Kamland, Phys. Lett. **B562** (2003), 28–35, hep-ph/0212202.

P. Aliani, V. Antonelli, M. Picariello, and E. Torrente-Lujan, *Neutrino mass parameters from* Kamland*,* SNO *and other solar evidence*, JCAP **0302** (2002), 001, hep-ph/0212212.

P. C. de Holanda and A. Y. Smirnov, LMA MSW *solution of the solar neutrino problem and first* Kamland *results*, JCAP **0302** (2003), 001, hep-ph/0212270.

[44] B. T. Cleveland et al., *Measurement of the solar electron neutrino flux with the* Homestake *chlorine detector*, Astrophys. J. **496** (1998), 505–526.

Sage, J. N. Abdurashitov et al., *Solar neutrino flux measurements by the Soviet-American Gallium Experiment* (Sage) *for half the 22-year solar cycle*, J. Exp. Theor. Phys. **95** (2002), 181–193.

Gallex, W. Hampel et al., Gallex *solar neutrino observations: Results for* Gallex IV, Phys. Lett. **B447** (1999), 127–133.

GNO, M. Altmann et al., GNO *solar neutrino observations: Results for* GNO I, Phys. Lett. **B490** (2000), 16–26, hep-ex/0006034.

Super-K, S. Fukuda et al., *Determination of solar neutrino oscillation parameters using 1496 days of* Super-Kamiokande-I *data*, Phys. Lett. **B539** (2002), 179–187, hep-ex/0205075.

SNO, Q. R. Ahmad et al., *Measurement of day and night neutrino energy spectra at* SNO *and constraints on neutrino mixing parameters*, Phys. Rev. Lett. **89** (2002), 011302, nucl-ex/0204009.

[45] M. A. Markov and I. M. Zheleznyhk, *On high energy neutrino physics in cosmic rays*, Nuclear Physics **27** (1961), 385.

K. Greisen, *Cosmics ray showers*, Ann. Rev. Nucl. Science **10** (1960), 63.

[46] T. K. Gaisser and M. Honda, *Flux of atmospheric neutrinos*, Ann. Rev. Nucl. Part. Sci. **52** (2002), 153–199, hep-ph/0203272.

[47] C. V. Achar et al., *Detection of muons produced by cosmic ray neutrinos deep underground*, Phys. Lett. **18** (1965), 196.

C. V. Achar et al., *Observation of a non-elastic cosmic ray neutrino interaction*, Phys. Lett. **19** (1965), 78.

F. Reines et al., *Evidence for high-energy cosmic ray neutrino interactions*, Phys. Rev. Lett. **15** (1965), 429–433.

[48] T. J. Haines et al., *Calculation of atmospheric neutrino induced backgrounds in a nucleon decay search*, Phys. Rev. Lett. **57** (1986), 1986–1989.

[49] Kamiokande-II, K. S. Hirata et al., *Experimental study of the atmospheric neutrino flux*, Phys. Lett. **B205** (1988), 416.

[50] Frejus, C. Berger et al., *A study of atmospheric neutrino oscillations in the* Frejus *experiment*, Phys. Lett. **B245** (1990), 305–310.

[51] W. W. M. Allison et al., *Measurement of the atmospheric neutrino flavour composition in* Soudan-2, Phys. Lett. **B391** (1997), 491–500, hep-ex/9611007.

[52] Macro, M. Ambrosio et al., *Measurement of the atmospheric neutrino-induced upgoing muon flux using* Macro, Phys. Lett. **B434** (1998), 451–457, hep-ex/9807005.

[53] J. G. Learned, S. Pakvasa, and T. J. Weiler, *Neutrino mass and mixing implied by underground deficit of low-energy muon-neutrino events*, Phys. Lett. **B207** (1988), 79.

V. D. Barger and K. Whisnant, *The effects of neutrino oscillations with one mass scale on the atmospheric neutrino flux*, Phys. Lett. **B209** (1988), 365.

K. Hidaka, M. Honda, and S. Midorikawa, *Neutrino oscillations and the anomalous atmospheric neutrino flux*, Phys. Rev. Lett. **61** (1988), 1537.

[54] Super-K, M. Shiozawa, *Experimental results on atmoshperic neutrinos in* Super-Kamiokande-I, (2002), Talk given at Neutrino 2002, Munich, Germany, http://neutrino2002.ph.tum.de.

Super-K, T. Toshito, Super-Kamiokande *atmospheric neutrino results*, (2001), hep-ex/0105023.

Super-K, S. Fukuda et al., *Tau neutrinos favored over sterile neutrinos in atmospheric muon neutrino oscillations*, Phys. Rev. Lett. **85** (2000), 3999–4003, hep-ex/0009001.

Super-K, Y. Fukuda et al., *Measurement of the flux and zenith-angle distribution of upward through-going muons by* Super-K, Phys. Rev. Lett. **82** (1999), 2644–2648, hep-ex/9812014.

Super-K, K. Scholberg, *Atmospheric neutrinos at* Super-Kamiokande, (1999), hep-ex/9905016.

Macro, M. Ambrosio et al., *Matter effects in upward-going muons and sterile neutrino oscillations*, Phys. Lett. **B517** (2001), 59–66, hep-ex/0106049.

F. Ronga, *Atmospheric neutrinos in the* Soudan-2 *and* Macro *experiments*, Nucl. Phys. Proc. Suppl. **100** (2001), 113–118.

[55] G. L. Fogli, E. Lisi, and D. Montanino, *A consistent three flavor approach to possible evidence of neutrino oscillations*, Astropart. Phys. **4** (1995), 177–188.

G. L. Fogli and E. Lisi, *On the atmospheric neutrino anomaly and its statistical significance*, Phys. Rev. **D52** (1995), 2775–2782, hep-ph/9504287.

[56] M. C. Gonzalez-Garcia, H. Nunokawa, O. L. G. Peres, and J. W. F. Valle, *Active-active and active-sterile neutrino oscillation solutions to the atmospheric neutrino anomaly*, Nucl. Phys. **B543** (1999), 3–19, hep-ph/9807305.

E. K. Akhmedov, A. Dighe, P. Lipari, and A. Y. Smirnov, *Atmospheric neutrinos at* Super-Kamiokande *and parametric resonance in neutrino oscillations*, Nucl. Phys. **B542** (1999), 3–30, hep-ph/9808270.

R. Foot, R. R. Volkas, and O. Yasuda, *Confronting solutions to the atmospheric neutrino anomaly involving large angle $\nu_\mu \to \nu_e$ oscillations with* Super-Kamiokande *and* Chooz, Phys. Lett. **B433** (1998), 82–87, hep-ph/9802287.

O. Yasuda, *Three flavor neutrino oscillation analysis of the* Super-Kamiokande *atmospheric neutrino data*, Phys. Rev. **D58** (1998), 091301, hep-ph/9804400.

R. Foot, C. N. Leung, and O. Yasuda, *Atmospheric neutrino tests of neutrino oscillation mechanisms*, Phys. Lett. **B443** (1998), 185–190, hep-ph/9809458.

N. Fornengo, M. C. Gonzalez-Garcia, and J. W. F. Valle, *On the interpretation of the atmospheric neutrino data in terms of flavor changing neutrino interactions*, JHEP **07** (2000), 006, hep-ph/9906539.

N. Fornengo, M. C. Gonzalez-Garcia, and J. W. F. Valle, *Updated global analysis of the atmospheric neutrino data in terms of neutrino oscillations*, Nucl. Phys. **B580** (2000), 58–82, hep-ph/0002147.

[57] M. C. Gonzalez-Garcia and M. Maltoni, *Two mass-scale oscillation analysis of atmospheric and reactor data*, Eur. Phys. J. **C26** (2003), 417–428, hep-ph/0202218.

M. Maltoni, T. Schwetz, M. A. Tortola, and J. W. F. Valle, *Constraining neutrino oscillation parameters with current solar and atmospheric data*, Phys. Rev. **D67** (2003), 013011, hep-ph/0207227.

[58] G. L. Fogli, E. Lisi, A. Marrone, and D. Montanino, *Status of atmospheric $\nu_\mu \to \nu_\tau$ oscillations and decoherence after the first* K2K *spectral data*, Phys. Rev. **D67** (2003), 093006, hep-ph/0303064.

[59] N. Fornengo, M. Maltoni, R. T. Bayo, and J. W. F. Valle, *Probing neutrino non-standard interactions with atmospheric neutrino data*, Phys. Rev. **D65** (2002), 013010, hep-ph/0108043.

[60] Y. Hayato, *Status of the* Super-Kamiokande*, the* K2K *and the* JPARC ν *project*, Talk at *HEP 2003*, International Europhysics Conference on High Energy Physics (Aachen, Germany, 2003).

[61] G. L. Fogli et al., *Addendum to: Solar neutrino oscillation parameters after first* Kamland *results*, Nucl. Phys. **B611** (2003), 3–39, hep-ph/0308055.

[62] CALTECH-SIN-TUM, G. Zacek et al., *Neutrino oscillation experiments at the* Gösgen *nuclear power reactor*, Phys. Rev. **D34** (1986), 2621–2636.

[63] Y. Declais et al., *Search for neutrino oscillations at 15-meters, 40-meters, and 95-meters from a nuclear power reactor at* Bugey, Nucl. Phys. **B434** (1995), 503–534.

[64] F. Boehm et al., *Final results from the* Palo Verde *neutrino oscillation experiment*, Phys. Rev. **D64** (2001), 112001, hep-ex/0107009.

[65] Chooz, M. Apollonio et al., *Limits on neutrino oscillations from the* Chooz *experiment*, Phys. Lett. **B466** (1999), 415–430, hep-ex/9907037.

Chooz, M. Apollonio et al., *Search for neutrino oscillations on a long baseline at the* Chooz *nuclear power station*, Eur. Phys. J. **C27** (2003), 331–374, hep-ex/0301017.

[66] F. Dydak et al., *A search for muon-neutrino oscillations in the* Δm^2 *range* $0.3\,\mathrm{eV}^2$ *to* $90\,\mathrm{eV}^2$, Phys. Lett. **B134** (1984), 281.

Fermilab E531, N. Ushida et al., *Limits to muon-neutrino, electron-neutrino* $\rightarrow$ *tau-neutrino oscillations and muon-neutrino, electron-neutrino* $\rightarrow$ *tau-direct coupling*, Phys. Rev. Lett. **57** (1986), 2897–2900.

K. S. McFarland et al., *A limit on muon-neutrino (anti-muon-neutrino)* $\rightarrow$ *tau-neutrino (anti-tau-neutrino) oscillations from a precision measurement of neutrino-nucleon neutral current interactions*, Phys. Rev. Lett. **75** (1995), 3993–3996, hep-ex/9506007.

Chorus, E. Eskut et al., *New results from a search for* $\nu_\mu \rightarrow \nu_\tau$ *and* $\nu_e \rightarrow \nu_\tau$ *oscillation*, Phys. Lett. **B497** (2001), 8–22.

Nomad, P. Astier et al., *Final* Nomad *results on* $\nu_\mu \rightarrow \nu_\tau$ *and* $\nu_e \rightarrow \nu_\tau$ *oscillations including a new search for* ν_τ *appearance using hadronic tau decays*, Nucl. Phys. **B611** (2001), 3–39, hep-ex/0106102.

[67] LSND, A. Aguilar et al., *Evidence for neutrino oscillations from the observation of* $\bar{\nu}_e$ *appearance in a* $\bar{\nu}_\mu$ *beam*, Phys. Rev. **D64** (2001), 112007, hep-ex/0104049.

[68] Karmen, B. Armbruster et al., *Upper limits for neutrino oscillations* $\bar{\nu}_\mu \rightarrow \bar{\nu}_e$ *from muon decay at rest*, Phys. Rev. **D65** (2002), 112001, hep-ex/0203021.

[69] Karmen, J. Wolf, *Final* LSND *and* Karmen-2 *neutrino oscillation results*, (2001), Prepared for International Europhysics Conference on High- Energy Physics (HEP 2001), Budapest, Hungary, 12-18 Jul 2001.

[70] K. Hagiwara et al., *Review of Particle Physics*, Physical Review D **66** (2002), 010001+.

[71] M. Maltoni and T. Schwetz, *Testing the statistical compatibility of independent data sets*, (2003), hep-ph/0304176.

[72] M. Maltoni, T. Schwetz, M. A. Tortola, and J. W. F. Valle, *Can four neutrinos explain global oscillation data including* LSND *and cosmology?*, (2003), hep-ph/0305312.

[73] M. Sorel, J. Conrad, and M. Shaevitz, *A combined analysis of short-baseline neutrino experiments in the (3+1) and (3+2) sterile neutrino oscillation hypotheses*, (2003), hep-ph/0305255.

[74] H. Murayama and T. Yanagida, LSND*,* SN1987A*, and* CPT *violation*, Phys. Lett. **B520** (2001), 263–268, hep-ph/0010178.

G. Barenboim, L. Borissov, J. Lykken, and A. Y. Smirnov, *Neutrinos as the messengers of* CPT *violation*, JHEP **10** (2002), 001, hep-ph/0108199.

[75] G. Barenboim, L. Borissov, and J. Lykken, CPT *violating neutrinos in the light of* Kamland, JHEP **10** (2002), 001, hep-ph/0212116.

[76] M. C. Gonzalez-Garcia, M. Maltoni, and T. Schwetz, *Status of the* CPT *violating interpretations of the* LSND *signal*, Phys. Lett. **B520** (2003), 263–268, hep-ph/0306226.

[77] Miniboone, G. McGregor, *The* Miniboone *experiment: Status and plans*, AIP Conf. Proc. **655** (2003), 58–67.

[78] V. D. Barger, K. Whisnant, and R. J. N. Phillips, *Three neutrino oscillations and present experimental data*, Phys. Rev. **D22** (1980), 1636.

V. D. Barger and K. Whisnant, *Global three-neutrino vacuum oscillation fits to the solar and atmospheric anomalies*, Phys. Rev. **D59** (1999), 093007, hep-ph/9812273.

M. C. Gonzalez-Garcia, M. Maltoni, C. Peña-Garay, and J. W. F. Valle, *Global three-neutrino oscillation analysis of neutrino data*, Phys. Rev. **D63** (2001), 033005, hep-ph/0009350.

G. L. Fogli, E. Lisi, A. Marrone, D. Montanino, and A. Palazzo, *Atmospheric, solar, and* Chooz *neutrinos: A global three generation analysis*, (2001), hep-ph/0104221.

[79] M. Battaglia et al., *The* CKM *matrix and the unitarity triangle*, Phys. Rev. Lett. **58** (2003), 1490–1493, hep-ph/0304132.

[80] P. Huber, M. Lindner, and W. Winter, *Superbeams versus neutrino factories*, Nucl. Phys. **B645** (2002), 3–48, hep-ph/0204352.

[81] M. Freund, P. Huber, and M. Lindner, *Systematic exploration of the neutrino factory parameter space including errors and correlations*, Nucl. Phys. **B615** (2001), 331–357, hep-ph/0105071.

[82] S. Choubey, S. T. Petcov, and M. Piai, *Precision neutrino oscillation physics with an intermediate baseline reactor neutrino experiment*, (2003), hep-ph/0306017.

[83] V. D. Barger, K. Whisnant, S. Pakvasa, and R. J. N. Phillips, *Matter effects on three-neutrino oscillations*, Phys. Rev. **D22** (1980), 2718.

T. Ohlsson and H. Snellman, *Three flavor neutrino oscillations in matter*, J. Math. Phys. **41** (2000), 2768–2788, hep-ph/9910546.

[84] A. Cervera et al., *Golden measurements at a neutrino factory*, Nucl. Phys. **B579** (2000), 17, hep-ph/0002108.

[85] M. Freund, *Analytic approximations for three neutrino oscillation parameters and probabilities in matter*, Phys. Rev. **D64** (2001), 053003, hep-ph/0103300.

[86] K2K, K. Nakamura, *Status of the* K2K *long-baseline neutrino-oscillation experiment*, Nucl. Phys. **A663** (2000), 795.

NuMI, J. Hylen et al., *Conceptual design for the technical components of the neutrino beam for the main injector* (NuMI), (1997), FERMILAB-TM-2018.

CNGS, G. Acquistapace et al., *The* CERN *neutrino beam to Gran Sasso* (NGS)*: Conceptual technical design*, (1998), CERN-98-02.

CNGS, R. Baldy et al., *The* CERN *neutrino beam to Gran Sasso* (NGS)*. (addendum)*, (1999), CERN-SL-99-034-DI.

[87] Y. Itow et al., *The* JHF-Kamioka *neutrino project*, Nucl. Phys. Proc. Suppl. **111** (2001), 146–151, hep-ex/0106019.

[88] D. Ayres et al., *Letter of intent to build an off-axis detector to study* $\nu_\mu \to \nu_e$ *oscillations with the* NuMI *neutrino beam*, (2002), hep-ex/0210005.

[89] M. Apollonio et al., *Oscillation physics with a neutrino factory*, (2002), hep-ph/0210192.

[90] H. Minakata and H. Nunokawa, *Exploring neutrino mixing with low energy superbeams*, JHEP **10** (2001), 001, hep-ph/0108085.

[91] G. L. Fogli and E. Lisi, *Tests of three-flavor mixing in long-baseline neutrino oscillation experiments*, Phys. Rev. **D54** (1996), 3667–3670, hep-ph/9604415.

[92] V. Barger, D. Marfatia, and K. Whisnant, *Breaking eight-fold degeneracies in neutrino* CP *violation, mixing, and mass hierarchy*, Phys. Rev. **D65** (2002), 073023, hep-ph/0112119.

[93] J. Burguet-Castell, M. B. Gavela, J. J. Gomez-Cadenas, P. Hernandez, and O. Mena, *On the measurement of leptonic* CP *violation*, Nucl. Phys. **B608** (2001), 301–318, hep-ph/0103258.

[94] P. Huber, M. Lindner, T. Schwetz, and W. Winter, *Reactor neutrino experiments compared to superbeams*, Nucl. Phys. **B665** (2003), 487–519, hep-ph/0303232.

[95] P. Huber, M. Lindner, and W. Winter, *Synergies between the first-generation* JHF-SK *and* NuMI *superbeam experiments*, Nucl. Phys. **B654** (2003), 3–29, hep-ph/0211300.

[96] P. Huber and W. Winter, *Neutrino factories and the 'magic' baseline*, Phys. Rev. **D68** (2003), 037301, hep-ph/0301257.

[97] M. C. Gonzalez-Garcia and C. Peña-Garay, *On the effect of θ_{13} on the determination of solar oscillation parameters at* Kamland, Phys. Lett. **B527** (2002), 199–205, hep-ph/0111432.

[98] H. Minakata, H. Sugiyama, O. Yasuda, K. Inoue, and F. Suekane, *Reactor measurement of θ_{13} and its complementarity to long-baseline experiments*, (2002), hep-ph/0211111.

[99] A. Donini, D. Meloni, and P. Migliozzi, *The silver channel at the neutrino factory*, Nucl. Phys. **B646** (2002), 321–349, hep-ph/0206034.

D. Autiero et al., *The synergy of the golden and silver channels at the neutrino factory*, (2003), hep-ph/0305185.

[100] P. Migliozzi and F. Terranova, *Next generation long baseline experiments on the path to leptonic* CP *violation*, Phys. Lett. **B563** (2003), 73–82, hep-ph/0302274.

[101] M. Diwan et al., *Very long baseline neutrino oscillation experiment for precise determination of oscillation parameters and search for $\nu_\mu \to \nu_e$ appearance and* CP *violation*, (2002), hep-ex/0211001.

[102] C. Cowan et al., *Detection of the free neutrino: A confirmation*, Science **124** (1956), 103.

C. Cowan and F. Reines, *The neutrino*, Nature **178** (1956), 446.

[103] L. A. Mikaelyan and V. V. Sinev, *Neutrino oscillations at reactors: What next?*, Phys. Atom. Nucl. **63** (2000), 1002–1006, hep-ex/9908047.

L. Mikaelyan, *Future reactor neutrino oscillation experiments at Krasnoyarsk*, Nucl. Phys. Proc. Suppl. **91** (2001), 120–124, hep-ex/0008046.

L. A. Mikaelyan, *Investigation of neutrino properties in experiments at nuclear reactors: Present status and prospects*, Phys. Atom. Nucl. **65** (2002), 1173, hep-ph/0210047.

[104] V. Martemyanov, L. Mikaelyan, V. Sinev, V. Kopeikin, and Y. Kozlov, *The* Kr2Det *project: Search for m_3 state contribution $|U_{e3}|^2$ to the electron neutrino using a one reactor - two detector oscillation experiment at Krasnoyarsk underground site*, (2002), hep-ex/0211070.

[105] M. Shaevitz, *Using reactors to measure θ_{13}*, (2003), Talk given at NOON 2003, Kanazawa, Japan, http://www-sk.icrr.u-tokyo.ac.jp/noon2003/.

[106] D. Beavis et al., *Proposal of* BNL AGS E-889, Tech. report, BNL, 1995.

[107] S. Geer, *Neutrino beams from muon storage rings: Characteristics and physics potential*, Phys. Rev. **D57** (1998), 6989–6997, hep-ph/9712290.

[108] R. Edgecock, *The* Mice *experiment*, J. Phys. **G29** (2003), 1601–1611.

[109] N. Holtkamp and S. Geer, *Feasibility study of neutrino source based on muon storage ring*, ICFA Beam Dyn. Newslett. **21** (2000), 37–51.

S. Ozaki et al., *Feasibility study–II of a muon–based neutrino source*, (2001), BNL-52623.

Muon Collider/Neutrino Factory, M. M. Alsharoa et al., *Status of neutrino factory and muon collider research and development and future plans.*, (2002), hep-ex/0207031.

P. Gruber (ed.) et al., *The study of a european neutrino factory complex*, (2002), CERN-PS-2002-080-PP.

[110] A. Cervera, F. Dydak, and J. Gomez Cadenas, *A large magnetic detector for the neutrino factory*, Nucl. Instrum. Meth. **A451** (2000), 123–130.

[111] O. Yasuda, *Physics potential and present status of neutrino factories*, (2002), hep-ph/0203273, and references therein.

[112] V. Barger, D. Marfatia, and B. Wood, *Resolving the solar neutrino problem with* Kamland, Phys. Lett. **B498** (2001), 53–61, hep-ph/0011251.

[113] R. J. Geller and T. Hara, *Geophysical aspects of very long baseline neutrino experiments*, Nucl. Instrum. Meth. **A503** (2001), 187–191, hep-ph/0111342.

[114] V. D. Barger et al., *Neutrino oscillation parameters from* Minos, Icarus *and* Opera *combined*, Phys. Rev. **D65** (2002), 053016, hep-ph/0110393.

[115] Super-K, M. B. Smy et al., *Precise measurement of the solar neutrino day/night and seasonal variation in* Super-Kamiokande-I, (2003), hep-ex/0309011.

[116] S. T. Petcov and M. Piai, *The* LMA MSW *solution of the solar neutrino problem, inverted neutrino mass hierarchy and reactor neutrino experiments*, Phys. Lett. **B533** (2002), 94–106, hep-ph/0112074.

[117] V. Barger, D. Marfatia, and K. Whisnant, *Off-axis beams and detector clusters: Resolving neutrino parameter degeneracies*, Phys. Rev. **D66** (2002), 053007, hep-ph/0206038.

V. Barger, D. Marfatia, and K. Whisnant, *How two neutrino superbeam experiments do better than one*, Phys. Lett. **B560** (2003), 75–86, hep-ph/0210428.

H. Minakata, H. Nunokawa, and S. Parke, *The complementarity of eastern and western hemisphere long- baseline neutrino oscillation experiments*, Phys. Rev. **D68** (2003), 013010, hep-ph/0301210.

[118] S. Parke and W. Winter, (2003), in preparation.

[119] A. De Rujula, M. B. Gavela, and P. Hernandez, *Neutrino oscillation physics with a neutrino factory*, Nucl. Phys. **B547** (1999), 21–38, hep-ph/9811390.

K. Dick, M. Freund, M. Lindner, and A. Romanino, CP*-violation in neutrino oscillations*, Nucl. Phys. **B562** (1999), 29–56, hep-ph/9903308.

A. Donini, M. B. Gavela, P. Hernandez, and S. Rigolin, *Neutrino mixing and* CP*-violation*, Nucl. Phys. **B574** (2000), 23–42, hep-ph/9909254.

[120] M. Freund, M. Lindner, S. T. Petcov, and A. Romanino, *Testing matter effects in very long baseline neutrino oscillation experiments*, Nucl. Phys. **B578** (2000), 27–57, hep-ph/9912457.

[121] J. Arafune, M. Koike, and J. Sato, CP *violation and matter effect in long baseline neutrino oscillation experiments*, Phys. Rev. **D56** (1997), 3093–3099, hep-ph/9703351.

H. Minakata and H. Nunokawa, *How to measure* CP *violation in neutrino oscillation experiments?*, Phys. Lett. **B413** (1997), 369–377, hep-ph/9706281.

H. Minakata and H. Nunokawa, CP *violation vs. matter effect in long-baseline neutrino oscillation experiments*, Phys. Rev. **D57** (1998), 4403–4417, hep-ph/9705208.

M. Tanimoto, *Indirect search for* CP *violation in neutrino oscillations*, Phys. Lett. **B435** (1998), 373–380, hep-ph/9806375.

[122] M. Freund, P. Huber, and M. Lindner, *Extracting matter effects, masses and mixings at a neutrino factory*, Nucl. Phys. **B585** (2000), 105–123, hep-ph/0004085.

[123] T. Ohlsson and W. Winter, *The role of matter density uncertainties in the analysis of future neutrino factory experiments*, (2003), hep-ph/0307178.

[124] J. Burguet-Castell, M. B. Gavela, J. J. Gomez-Cadenas, P. Hernandez, and O. Mena, *Superbeams plus neutrino factory: The golden path to leptonic* CP *violation*, Nucl. Phys. **B646** (2002), 301–320, hep-ph/0207080.

[125] Opera, M. Guler et al., *Experiment proposal* Opera*: An appearance experiment to search for $\nu_\mu \to \nu_\tau$ oscillations in the* CNGS *beam*, Tech. Report CERN/SPSC 2000-028, SPSC/P318, LNGS P25/2000, 2000.

[126] Icarus, F. Arnedo et al., *Cloning of* T600 *modules to reach the design sensitive mass*, Tech. Report ICARUS-TM/2001-08 LNGS-EXP 13/89 add. 2/01, 2001.

[127] P. Zucchelli, *A novel concept for a $\bar{\nu}_e/\nu_e$ neutrino factory: The β-beam*, Phys. Lett. **B532** (2002), 166–172.

[128] M. Mezzetto, *Physics reach of the β-beam*, J. Phys. **G29** (2003), 1771–1776, hep-ex/0302007.

[129] SNO, S. N. Ahmed et al., *Measurement of the total active ^8B solar neutrino flux at the Sudbury Neutrino Observatory with enhanced neutral current sensitivity*, (2003), nucl-ex/0309004.

[130] M. D. Messier, private communication.

[131] P. Vogel and J. F. Beacom, *The angular distribution of the reaction $\bar{\nu}_e + p \to e^+ + n$*, Phys. Rev. **D60** (1999), 053003, hep-ph/9903554.

[132] G. Alimonti et al., *A large-scale low-background liquid scintillation detector: The counting test facility at Gran Sasso*, Nucl. Instrum. Meth. **A406** (1998), 411–426.

[133] S. Schönert, T. Lasserre, and L. Oberauer, *The* HLMA *project: Determination of high Δm^2_{21}* LMA *mixing parameters and constraint on $|U_{e3}|$ with a new reactor neutrino experiment*, Astropart. Phys. **18** (2003), 565–579, hep-ex/0203013.

[134] P. Vogel and J. Engel, *Neutrino electromagnetic form-factors*, Phys. Rev. **D39** (1989), 3378.

H. Murayama and A. Pierce, *Energy spectra of reactor neutrinos at* Kamland, Phys. Rev. **D65** (2002), 013012, hep-ph/0012075.

[135] Minos, E. Ables et al., P-875*: A long baseline neutrino oscillation experiment at Fermilab*, (1995), FERMILAB-PROPOSAL-0875.

[136] D. A. Harris, private communication.

[137] M. D. Messier, *Basics of the* NuMI *off-axis beam*, Talk given at "New Initiatives for the NuMI Neutrino Beam", May 2002, Batavia, IL.

[138] T. Nakaya, private communication.

[139] J. N. Bahcall, M. C. Gonzalez-Garcia, and C. Peña-Garay, *Robust signatures of solar neutrino oscillation solutions*, JHEP **04** (2002), 007, hep-ph/0111150.

[140] Monolith, N. Y. Agafonova et al., Monolith*: A massive magnetized iron detector for neutrino oscillation studies*, (2000), LNGS-P26-2000.

[141] C. Albright et al., *Physics at a neutrino factory*, (2000), hep-ex/0008064, and references therein.

[142] A. Geiser, private communication.

[143] A. Blondel et al., *The neutrino factory: Beam and experiments*, Nucl. Instrum. Meth. **A451** (2000), 102–122.

[144] M. D. Messier, *Evidence for neutrino mass from observations of atmospheric neutrinos with* Super-Kamiokande, Ph.D. thesis, Boston University, 1999.

[145] K. Ishihara, *Study of $\nu_\mu \rightarrow \nu_\tau$ and $\nu_\mu \rightarrow \nu_{\rm sterile}$ neutrino oscillations with the atmospheric neutrino data in* Super-Kamiokande, Ph.D. thesis, University of Tokyo, 1999.

[146] K. Okumura, *Observation of atmospheric neutrinos in* Super-Kamiokande *and a neutrino oscillation analysis*, Ph.D. thesis, University of Tokyo, 1999.

[147] W. Flanagan, *A study of atmospheric neutrinos at* Super-Kamiokande, Ph.D. thesis, University of Hawaii, 1997.

[148] L. Oberauer, private communication.

[149] W. H. Press, S. A. Teukolsky, W. T. Vetterling, and B. P. Flannery, *Numerical Recipes in C*, Cambridge University Press, 1995.

This thesis was typeset with LaTeX2e using the packages a4, amsmath, amssymb and graphicx. The font is Computer Modern 11 pt by Donald E. Knuth. The bibliography was prepared with BibTeX and the packages cite and mcite. The style file for BibTeX is a modified version of amsplain. This work is printed on acid free paper.